The Beam-Down Solar Thermal Concentrator: Experimental Characterization and Modeling

By

Marwan Basem Mokhtar

A Thesis Presented to the

Masdar Institute of Science and Technology

in Partial Fulfillment of the Requirements for the Degree of

Master of Science

in

Mechanical Engineering

The Beam-Down Solar Thermal Concentrator: Experimental Characterization and Modeling

By Marwan Basem Mokhtar

A Thesis Presented to the Masdar Institute of Science and Technology in Partial Fulfillment of the Requirements for the Degree of

Master of Science in Mechanical Engineering

June 2011

AUTHOR'S DECLARATION

I understand that copyright in my thesis is transferred to Masdar Institute of Science and Technology.

Author _____

RESEARCH SUPERVISORY COMMITTEE MEMBERS

Dr. Matteo Chiesa, Advisor, Chair, _____

Masdar Institute of Science and Technology

Dr. Peter Armstrong, Co-Advisor, _____

Masdar Institute of Science and Technology

Dr. Olaf Goebel, _____

Masdar Power

Abstract

Solar thermal technologies have emerged as a strong candidate for large scale power generation. Unlike other renewable energy technologies, Concentrated Solar Power (CSP) offers the capability of supplying reliable dispatchable power. Among CSP technologies point-focus power tower or central receiver plants promise higher thermodynamic conversion efficiencies compared to line focus technologies due to their higher achievable temperatures. The Beam-Down solar thermal concentrator is a variation of central receiver plants with Cassegrainian optics. It was constructed in Masdar City in 2009 in order to investigate the potential of the unconventional plant design. The Beam-Down optics and the heliostat construction are considered to be the two main modifications on regular central receiver plant designs.

In March 2010 our research team at LENS (the Laboratory for Energy and Nano-Science) performed a comprehensive test on the Beam-Down heliostat field using the existing flux measurement system consisting of a CCD camera and heat flux sensors. It was concluded that two main issues require further investigation and became the focus of this thesis:

- The reliability of the flux measurement set up used to characterize the performance of the plant,
- The concentration quality of the individual heliostats which directly affects the performance of the plant.

Based on that, and in order to investigate and analyze the flux concentration quality of the unique heliostats, a model was considered necessary. A geometrical optics model is presented. The

model is developed to investigate the causes of optical aberrations of the heliostats. It is also adapted to assess the effect of varying optical errors and sunshapes on concentration quality and radiation spillage. The optical model uses geometry and vector algebra to maintain the computation speed high and to simplify implementation compared with stochastic methods.

Efforts were also directed on enhancing the accuracy of the heat flux sensors which are used as a reference for the optical flux measurement system consisting of a Charge-Coupled Device (CCD) camera. A regression model for correcting the heat flux sensor measurement is proposed. It is founded on a convective and radiative heat transfer model of the flux sensor. As will be shown, the proposed model for calibration reduces the measurement error significantly, especially at low radiation fluxes. In addition, since the model is based on easily measurable variables it can be applied conveniently on existing measurement systems without major modifications.

An analysis of the overall Beam-Down performance is presented. The analysis is based on a theoretical receiver design. Performance curves of plant under varying operating temperatures, ambient conditions and concentration levels are presented. This gives an overview of the plant performance as a whole. The analysis is based on full concentration test data obtained experimentally at the plant in March 2011 using the retrofitted measurement system.

A part of this thesis is dedicated to discussing some topics of practical importance in solar concentrating system with an optical lay out similar to our Beam-Down concentrator. Optical alignment procedures of the central reflector mirrors and the tracking sensors of the heliostats are discussed. In addition the canting procedure of individual heliostat facets and their effect on amount of intercepted radiation is also addressed.

This research was supported by the Government of Abu Dhabi to help fulfill the vision of the late President Sheikh Zayed Bin Sultan Al Nayhan for sustainable development and empowerment of the UAE and humankind.

Acknowledgement

Special appreciation is extended to all those who contributed their time and energy in any way in order to help in getting this mission finished.

Prays and thanks for Allah, for giving me the inspiration and determination that made it possible for me to carry through the hard times, needless mentioning the good times.

Special thanks are extended to my advisor Dr. Matteo Chiesa for his assistance, guidance and encouragement throughout my stay in Abu Dhabi. I appreciate your way of working with me; it made me feel like your friend rather than your student. I would also like to thank Dr. Peter Armstrong for his valuable comments, fruitful discussions and enlightening ideas. Many things would have not been possible without your help.

I would also like to thank all LENS group members for their continuous help and support, special thanks for my Beam-Down partner Mr. Steven Meyers for his valuable assistance that made this possible. Special thanks are also due to all whom I have enjoyed working with at the Beam-Down: Abdul Qadir, Irene, Zaid, Tauha, Ragini and Abdu Aziz.

Thanks are due to Dr. Olaf Goebel Head of Engineering at Masdar Power, for his fruitful comments and discussions and for serving in my research supervisory committee.

It would have not been possible for me to undertake this study without the financial support from Masdar Institute of Science and Technology. Their generous support is highly appreciated.

Thanks are also extended to the administrative staff of Masdar Institute for their help during my stay in Abu Dhabi.

Thanks are extended to our partners in MES, Cosmo oil and Tokyo Tech. In particular, I would like to thank Mr. Kazu Ezawa for his continuous support in the Beam Down plant.

I would like also to thank Mr. Stefan Wilbert, Dr. Christoph Richter and all the colleagues in the German Aerospace Center (DLR) for the experience I gained during my internship which was instrumental in advancing my research.

Special thanks are also extended to Dr. Dima al Nazer for her help in preparing the final version of this document.

I also would like to thank all my friends and colleagues at Masdar Institute. First for the friendly environment that I enjoyed and second for the knowledge and advice that was most needed. Thank you all for those memorable times.

Last, but certainly not least, my deep thanks to my parents Basem and Dima and for my brother Muhannad, my sister Maha, and my brother Saleem for their continuous encouragement and their support during my study abroad.

Contents

Abstract i

الملخص ..... **Error! Bookmark not defined.**

Contents vi

List of Figures x

List of Abbreviations xv

Nomenclature xvii

1 Introduction 1

1.1 Motivation 1

1.2 Problem Definition and Objectives 3

1.3 Description of the Beam-Down Concentrator 5

1.3.1 Concept 5

1.3.2 Heliostat Field 8

1.3.3 Flux Measurement System 11

2 Geometrical-Optics Model and Error Analysis of Concentrated Flux Distribution from a Single Heliostat 13

2.1 Coordinate System 15

2.2 Defining Heliostat Geometry 17

2.2.1 Positions of facet centers at different elevation and azimuth angles 18

2.2.2 Facet tilt angles and rotation of facets' unit normal for elevation and azimuth angles 19

2.3 Geometrical Optics Model 20

2.4 Heliostat Positioning 22

2.5 Optical Analysis and Error Propagation 23

2.5.1 Intercept factor 25

2.5.2 Angular acceptance function 26

2.5.3 Error mapping between sun plane and global azimuth and elevation coordinates . 28

2.6 Model Application to the Beam-Down B8 Heliostat 31

2.7 Summary 39

3 Heat Flux Measurement System 40

3.1 A Model for Improved Solar Irradiation Measurement at Low Flux using Heat Flux Sensors 42

3.1.1 Preliminary Testing of Heat Flux Sensors 45

3.1.2 Principle of Operation of Heat Flux Sensors 46
3.1.3 Heat Transfer Model 48
3.1.4 Experimental Setup 49
3.1.5 Linear Regression Model 51
3.1.6 Residuals Analysis 55
3.2 In situ Calibration of Heat Flux Sensors 57
3.2.1 Experimental Setup 58
3.2.2 Generalized Correction Model 61
3.3 Summary 65
4 Heliostat Field Performance Characterization 67
4.1 Concentration quality 68
4.2 Weighted Flux Map 68
4.3 Centroid and Offset Calculation 70
4.3.1 Finding $g_{ambient}$ 71
4.3.2 Filtering for Centroid Calculation 72
4.3.3 Filtering for calculating cumulative power curve 72
4.4 Selecting Hypothetical Receiver Dimensions 73
4.5 Results 77
4.5.1 Tower Shading 80

4.5.2 Heliostat concentration Errors 81
4.6 Summary 83
5 Analysis of Beam-Down Performance under Full Concentration 84
5.1 Receiver Net Useful Power 85
5.2 Receiver Thermal Losses 86
5.3 Incident Power Variation 88
5.4 Receiver Sizing 92
5.5 Receiver Performance 92
5.6 Summary 96
6 Practical Considerations in the Beam-Down Solar Thermal Concentrator 98
6.1 Optics Alignment 98
6.2 Canting and Spillage 103
Conclusion 108
Future Work 111
Bibliography 113

List of Figures

Figure 1-1 Beam Down Solar Thermal Concentrator, central reflector is illuminated by radiation from the heliostat field 5

Figure 1-2 Vertical cross sectional view of 100kW pilot plant (Hiroshi Hasuike et al. 2009)..... 6

Figure 1-3 The aim point at height (H) serves as one focus (F1) for both the ellipse and the hyperbola, the other focus being at the receiver located near the ground at (F2). (Figure courtesy of (Winter, Sizmann, and Vant-Hull 1991))..... 7

Figure 1-4 Heliostat Field Layout..... 9

Figure 1-5 Typical ganged type heliostat and tracking sensor. The center of the control mirror, the tracking sensor and the focal point are aligned on a common line. 10

Figure 2-1 Schematic of the Beam Down Heliostat Field and Tower Position for Definition of the Global Coordinate System 16

Figure 2-2 Schematic of a Heliostat and the Local Coordinate System (Figure courtesy of MES) 17

Figure 2-3 Elemental scanning of the sun plane, i.e the effective source..... 29

Figure 2-4 Differential change dϕ in global coordinates relative to the change dw in sun plane 30

Figure 2-5 Top view of Figure 2-4 illustating the change in elevation angle due to the change dw (angles are exagurated for clarity) 31

Figure 2-6 Visualization of the model applied to heliostat B8 in the reference position (i.e zero azimuth, 90^o elevation). Dimensions in (mm). 33

Figure 2-7 Sunshape, effective errors and the resulting effective source distribution..... 34

Figure 2-8 Error in various facets of B8 heliostats at different sun positions. Deviation is the distance between the location of the facet center at target plane assuming an ideal effective source compared to using the actual effective source. This deviation does not include the effect of aberrations. 36

Figure 2-9 Left: facet centers on target plane deviated from ideal location at origin (0,0). Red points showing deviation assuming an ideal effective source. Blue points include both aberrations and an effective error in elevation and azimuth, of $d\alpha$ and $d\varphi$ respect 39

Figure 3-1 Target plane as seen by the CCD camera. Heat flux sensors locations are shown, 5-8 Schmidt-Boelter thermopile based sensors, 1-4 Gardon type foil based sensors. 42

Figure 3-2 Radiation flux using factory calibration versus the radiation flux measured by the reference instrument (RMSE= 115 W/m^2). 46

Figure 3-3 Inner construction of a typical HFS (but not of the exact model used) (Kidd and Nelson 1995)..... 47

Figure 3-4 Right: BDSTC tower and heliostat field with experimental setup in front, left: details of the experimental setup 50

Figure 3-5 Electrical analog for the HFS heat transfer model 51

Figure 3-6 Variation of sensing element temperature T_{SE}, mean water temperature T_w and ambient temperature T_a. 52

Figure 3-7 Radiation flux predicted using the proposed model of equation 3-9 versus the radiation flux measured by the reference instrument (RMSE=6.3 W/m^2)..... 54
Figure 3-8 Error due to shadowing of the test rig in early morning. On the left a zoomed-in view where one can observe how shadow is progressing, first shading the PSP then the Licor and last the HFS..... 55
Figure 3-9 Residuals distribution versus explanatory variables..... 56
Figure 3-10 Residuals distribution versus explanatory variables for the test data set..... 57
Figure 3-11 Experimental setup of heat flux measurement on the target plane using HFS. Up: A view of the sensors attached to the target from underneath. Coolant flows to the sensors from a well insulated tank with a sufficient thermal mass to prevent temperature fluctuations. The coolant is distributed to the sensors using a manifold to ensure even flow. Ambient temperature and RH under the target are recorded Bottom: thermocouples are used to measure coolant outlet temperature of each of the eight sensors in addition to coolant temperature in the tank, thermopile output of the sensor and all thermocouples are directed to the main data logger using an AM25T multiplexer..... 60
Figure 3-12 Residuals distribution versus explanatory variables..... 65
Figure 4-1 Typical flux density map generated by the overhead CCD camera (Resolution: 980x980 pixels)..... 70
Figure 4-2 Mean radiation at a radial distance (r) from the centroid of the flux map, normalized by the theoretical maximum power given by (DNI*number of flat heliostat facets*area of one pixel), this theoretical maximum is the upper limit of radiation concentration as it clearly ignores cosine factor, incidence angle, reflectivity of the mirrors in addition to other things..... 74

Figure 4-3 Cumulative power intercepted by the receiver from the centroid until the radial distance (r), normalized by the maximum theoretical total power (DNI * Heliostat Area). This theoretical maximum is the upper limit of radiation concentration as it clearly ignores cosine factor, incidence angle, and reflectivity of the mirrors in addition to other things. .. 74
Figure 4-4 Cumulative power intercepted by the receiver from the centroid until the radial distance (r), normalized by the total power. 76
Figure 4-5 Flux maps with receiver apertures drawn around the centroid, flux maps where filtered using equation 3 and a k value of 1. 77
Figure 4-6 Complete shading of "A-line" heliostats in the North sector around solar noon, sun elevation angle ~60^{o}..... 81
Figure 4-7 Heliostat concentration errors showing scattering and aberrations..... 82
Figure 5-1 A typical flux map showing a conceptual two-aperture receiver, inner receiver for high temperature superheating and outer receiver for low temperature preheating. 90
Figure 5-2 Cumulative power (*Pcum*) intercepted by the receiver starting from the centroid until a radial distance (*r*). Curves are shown for different times of the day..... 91
Figure 5-3 Daily average cumulative power (*Pcum*) intercepted by the receiver starting from the centroid until a radial distance (*r*). 91
Figure 5-4 Net power collected as a function of receiver radius. Convection and radiation losses are also shown as a function of receiver size. 92
Figure 5-5 Optical efficiency of the receiver..... 93
Figure 5-6 Receiver thermal efficiency 94
Figure 5-7 Overall efficiency of the receiver..... 94
Figure 5-8 Useful power collected in the HTF 95

Figure 5-9 Maximum possible work rate (Exergy)..... 96
Figure 5-10 Day average of maximum possible work as a function of output MFT..... 96
Figure 6-1 Tracking feedback sensor with laser pointer used for the alignment..... 99
Figure 6-2 Intersection points of laser beam on the target plane. Experiment was done four times for each heliostat at different laser pointer rotation angles, differences are due to mechanical inaccuracies in the laser attachment bracket which are magnified by long travel distance.101
Figure 6-3 Heliostat B8 having some radiation falling on the outer CR mirror (Time: 11:15, 1:15 before solar noon). 102
Figure 6-4 Heliostat B8 with better centering on the correct CR mirror however with scattered radiation of the four adjacent CR mirrors, and with the center of the radiation moving farther from the true target center. (Time: 13:45, 1:15 after solar noon)..... 102
Figure 6-5 Left: B8 concentrated flux deviated from the center point. Right: B8 concentrated flux after correcting CR mirror inclination 103
Figure 6-6 Vertical cross sectional view of Beam Down concentrator showing individual heliostat focus well above the target plane (Hiroshi Hasuike et al. 2009)..... 105
Figure 6-7 Effect of canting angles on the spillage of the reflected radiation and on the quality of the concentrated radiation on the target plane. Left: Actual canting angles used. Right: “Focuced” canting angles. 106
Figure 6-8 Heliostat spillage variation simulated for 9-March-2011. Left: Actual canting angles used. Right: “Focuced” canting angles. 106

List of Abbreviations

BDSTC	Beam-Down Solar Thermal Concentrator
CCD	Charge Coupled Device
CR	Central Reflector
CSP	Concentrated Solar Power
CSR	Circumsolar Ratio
DNI	Direct Normal Irradiation
GHI	Global Horizontal Irradiation
HFS	Heat Flux Sensor
HTF	Heat Transfer Fluid
LEC	Levelized Energy Cost
MFT	Mean Fluid Temperature
MPT	Mean Plate Temperature
MWT	Mean Wall Temperature
PIR	Precision Infrared Radiometer
PSP	Precision Spectral Pyranometer
RMSE	Root Mean Square Error

SE	Sensing Element
Wspd	Wind Speed

Nomenclature

A	Area of receiver aperture	m^2
B_{eff}	Effective source	
$B_{sunshape}$	Sunshape	
c_o, c_1, c_2, c_3	Regression model coefficients	
c_k	Position vector of the center of the k^{th} facet	
c_P	Specific heat of the HTF	$J\ kg^{-1}\ K^{-1}$
D_i	Receiver's tube inner diameter	m
D_o	Receiver's tube outer diameter	m
e_i	Position vectors of the center of each of the elevation axes	
F'	Collector efficiency factor	
F_R	Heat removal factor	
f	Position vector of the upper focal point	
$f(\theta)$	Angular acceptance function	
G_{HFS}	Solar radiation measured by the HFS	W/m2
G_{IR}	Net IR radiation measured by the PIR	W/m^2
G_{PSP}	Solar radiation measured by the PSP	W/m2
Gr	Grashof number	

g	Gravitational acceleration	m s^{-2}
$\hat{g}_k$	Unit reflected vector from the CR mirror to the target	
$\tilde{h}_{cf}v$	Forced convection heat transfer coefficient	W m^{-2} K^{-1}
h_{cn}	Natural convection heat transfer coefficient	W m^{-2} K^{-1}
h_c	Convection heat transfer coefficient	W m^{-2} K^{-1}
h_f	Convection heat transfer coefficient between HTF an inner wall	W m^{-2} K^{-1}
h_r	Linearized radiation heat transfer coefficient	W m^{-2} K^{-1}
k	Thermal conductivity	W m K^{-1}
$\tilde{k}$	Dome heating correction factor	
L	Thickness of the resistive wafer	m
$\dot{m}$	HTF mass flow rate	kg s^{-1}
Nu	Nusselt number	
n	Number of hot (or cold) junctions of the thermocouple circuit	
$\hat{n}_k$	Unit normal of each facet	
$P_{CR,k}$	Intersection points with the CR	
Pr	Prandlt number	
$P_{T,k}$	Intersection points with the target	
$\dot{Q}_u$	Net useful power output of the receiver	W
$\dot{Q}_{incident}$	Incident solar power on the receiver aperture	W
q_{net}	Net het flux across through the sensing element	W m^{-2}
R_e	Reynolds number	
$R_y(\theta)$	Counterclockwise rotation matrix around the y-axis	
$R_z(\theta)$	Counterclockwise rotation matrix around the z-axis	

$\hat{s}$	Sun position vector	
$\hat{r}_k$	Unit reflected vector	
T_a	Ambient temperature	K
T_{case}	PIR case temperature	K
T_{dome}	PIR dome temperature	K
T_e	Air temperature	K
T_{fi}	Inlet mean fluid temperature	K
T_{fo}	Outlet mean fluid temperature	K
T_{pm}	Mean plate temperature	K
T_{SE}	Sensing element temperature	K
T_{sky}	Effective sky temperature	K
T_w	Mean water temperature	K
U_L	Overall heat loss coefficient	W m^{-2} K^{-1}
u_e	Wind speed	m s^{-1}
V	Voltage generated by the thermopile	mV
α	Solar absorptivity.	
	Solar elevation angle	rad
$(\alpha AG)_{SE}$	Effective absorptivity-area-incident radiation product of the sensing element	W
β	Volumetric expansion coefficient	K^{-1}
γ	Intercept factor	
ϵ_{SE}	Emissivity of sensing element coating	
ΔT	Temperature difference across the resistive wafer	K
δ	Seebeck coefficient	mV K^{-1}

σ	Stefan-Boltzmann constant	5.6704 E-8W m^{-2} K^{-4}
	Error mrad	
ϕ	Solar azimuth angle	rad
v	Kinematic viscosity	m^2 s^{-1}
θ_{azi}	Azimuth angle of the heliostat	rad
θ_{ele}	Elevation angle of the heliostat	rad

CHAPTER 1

INTRODUCTION

1.1 MOTIVATION

Solar thermal technologies have emerged as a strong candidate for large scale power generation. Unlike other renewable energy technologies, Concentrated Solar Power (CSP) offers the capability of supplying reliable dispatchable power; through integration with thermal storage systems, or through hybrid operation with existing fossil-fueled plants. Therefore, offering firm generation capacity suitable for peak and base load operation [1].

From a newly-introduced technology, CSP has become one of the mainstream power generation solutions. CSP installations were providing only 436 MW of the world's electricity generation at the end of 2008. According to [1], CSP Projects under construction, mostly in Spain, will add at least another 1,000 MW by 2011. Further, projects adding up to 7,000 MW are under planning and development in the USA, in addition to 10,000 GW in Spain, which could all come online by 2017. [1].

Masdar has recently started the construction of the first CSP solar power station in the UAE. Shams One, will be the first large scale solar power plant in the Middle East with a capacity of 100MW, generating 210GWh of electricity per year [2]. Furthermore, around 1500 MW of solar power is planned in the coming years (split between CSP and PV), this is a strong statement of commitment from the government of Abu Dhabi towards future energy and CSP technologies. [2].

Although not as well established a technology as parabolic trough, central receiver CSP plants promise higher energy conversion efficiency and consequently lower levelized energy cost (LEC) [3]. Nonetheless, holding back its wide deployment is the uncertainty in cost, performance and technical risk mainly due to the lack of commercial central receiver project experience [4]. The largest commercial tower plant (Gemasolar) is currently being built in Spain by a joint venture company between Masdar and Sener; Torresol Energy, yet another proof of Abu Dhabi's commitment to CSP.

Commercialization of tower technology of course helps in cost reduction and lowering project risk, however, it is expected that 48% of the cost reduction in tower plants costs will come from technology research and development [4]. Revolutionary advances are needed in areas such as

high temperature receivers, conversion cycles, solar fuels, storage systems, heat transfer fluids, heliostat construction, heat rejection technologies, flux measurement, resource assessments…etc.

It is therefore essential to build up the necessary R&D infrastructure and develop our expertise in the field, to be able to address local and global technology problems facing the development and implementation of CSP.

1.2 Problem Definition and Objectives

Masdar City 100 kW_{th} Beam-Down solar thermal concentrator was proposed by Tokyo Institute of Technology (TiTech). TiTech led the consortium in charge of building the pilot plant. The main objective of this project was to test several design concepts that can reduce the overall cost of this type of power tower, verify a numerical code developed by TiTech and ultimately investigate the feasibility of scaling the beam down concentrator to significantly higher capacities (20MW). With Beam-Down optics, the central reflector design and the ganged-type heliostats being the main departures from conventional designs.

Upon taking operation responsibility of the Beam-Down plant a measurement campaign was conducted to characterize the plant and investigate the unique design aspects. Based on our analysis we identified serious inadequacies in the flux measurement system that was employed to measure the plant's performance. In addition some challenges related to the concentration quality of the heliostats were reported. These challenges were ultimately attributed to the unusual design of the optical components (proposed by MES) [5].

Based on the test's preliminary results, developing a reliable measurement system became our number one priority. Especially considering that it will serve as a basis for any future design

decisions and performance forecasts for this kind of power tower lay out. Once the flux measurement system is shown to produce reliable flux mapping, it can be employed to assess the performance of the plant.

The flux mapping system in use, is a hybridization between an optical imaging device (a CCD camera), and heat flux transducers. The CCD camera provides images of the target plane lit by concentrated solar radiation. The heat flux sensors measure absolute heat flux on the target plane at specific measurement points. Theoretically the luminous intensity measured by the CCD camera can be calibrated by the heat flux sensor measurement to provide a heat flux map. This however is only possible if the heat flux sensors measurement is well corrected for variation in ambient conditions, if the CCD camera images are repeatable and if the target is a uniform diffuse (i.e. Lambertian) reflector.

The measurement system showed uncertainty in estimating flux, which is not suitable for accurate performance assessment. Nonetheless, the CCD camera images can provide useful preliminary information about flux distribution that can be used to study the concentration quality of heliostats. Hence this task was carried out in parallel with the work done on the measurement system.

Furthermore, the CCD images provide valuable information useful for the validation of an optical model of heliostats' concentration. The model is employed in studying the optical aberrations in the heliostat images at varying sun positions. It is also used to assess the effect of different sources of optical errors (mirror surface errors, sunshape, alignment errors etc.) on the concentration quality. The developed model can eventually be extremely useful in finding the optimal compromise between cost and quality of the optical design.

1.3 DESCRIPTION OF THE BEAM-DOWN CONCENTRATOR

1.3.1 *CONCEPT*

The Beam-Down Solar Thermal Concentrator (BDSTC) (Figure 1-1) is a point focus concentrator of around 280 m^2 of primary reflective area. The primary reflector system comprises of 33 2-axis tracking heliostats. As shown in Figure 1-2, the heliostats focus sunlight on one imaginary upper focal point. The radiation gets intercepted however, by a secondary Central Reflector (CR) on top of the tower, and is then redirected to a lower focal point close to ground level.

Figure 1-1 Beam Down Solar Thermal Concentrator, central reflector is illuminated by radiation from the heliostat field

The BDSTC is a central-tower like system but instead of collecting solar energy in the heat transfer fluid on top of the tower as is done in conventional tower plants, the receiver is located at the lower focal point close to ground. This is accomplished by a set of secondary optics of CR.

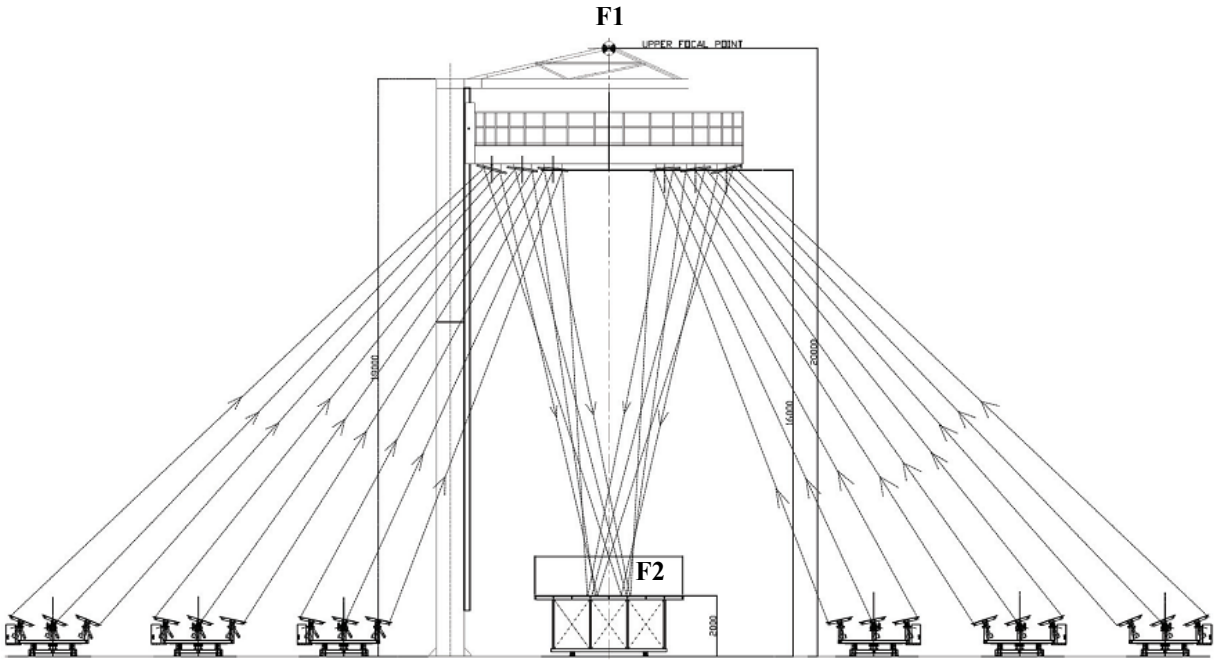

Figure 1-2 Vertical cross sectional view of 100kW pilot plant [6]

Such application of Cassegranian optics has been discussed in the literature [7][8]. As shown in Figure 1-3, when solar radiation is focused on the first focal point (F1) it will be redirected towards the lower focal point (F2). There are three configurations that can be implemented as discussed in [8]:

- Case 1: elliptic secondary reflector. This requires placing the reflector even farther than the focal point which not only increases cost but also increases images size with no added value.

- Case 2: hyperboloid secondary reflector placed between (F1) and (F2).
- Case 3: a flat reflector which can be also used as shown in Figure 1-3 but it might have to be wider than the reflector in Case2.

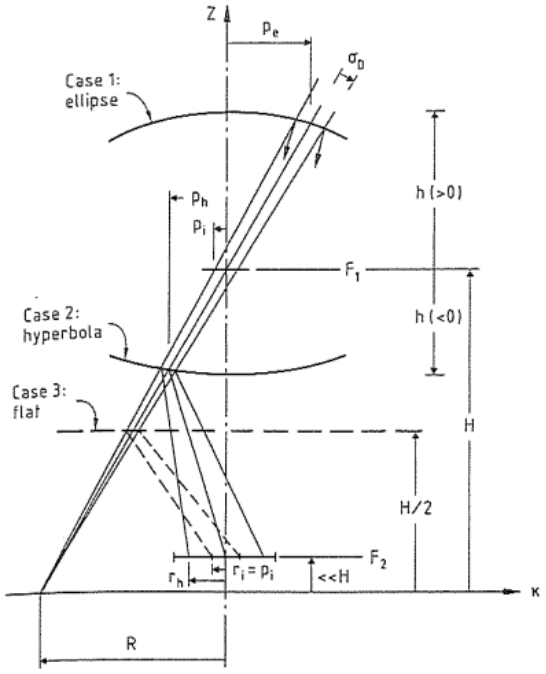

Figure 1-3 The aim point at height (H) serves as one focus (F1) for both the ellipse and the hyperbola, the other focus being at the receiver located near the ground at (F2). (Figure courtesy of [8])

In the BDSTC, a set of flat mirrors tracing the profile of a hyperbola are used as a secondary reflector (Case 2). They reflect the radiation back to the lower focal point as shown in Figure 1-2. The use of mirror segments instead of a continuous hyperbolic mirror have the advantages of reducing the manufacturing costs, lowering wind load on the tower structure and providing natural cooling for the mirrors hence reducing thermal stresses. However the use of flat mirrors in the secondary receiver poses some optical restrictions on the heliostats aiming and focusing capability, since each heliostat is restricted to focus its radiation to a single facet

otherwise it will be reflected off center. This imposes premature focusing of heliostat image to prevent radiation spillage and results in a reduction in the overall concentration on the target plane.

The Beam-Down concept faces several obstacles to realization [9] namely: the loss due to the extra reflection, the mechanical integrity of central reflector against wind load compared to the slender conventional towers, the dilution of beam concentration at receiver aperture due to the extra travel distance in addition the heliostat field configuration [9].

Besides the advantages outlined by Tamaura et al. related to having heavy receivers placed near ground level, perhaps the most attractive feature of the Beam-Down configuration is the possibility of using cavity receivers. Since all the radiation falls on the target from a narrow angle of less than 20^{o} cavity receivers are well suited for such configuration. Compared to open receivers commonly used in conventional tower plants, cavity receivers have a smaller aperture which means that thermal losses are strongly reduced and consequently higher temperature can be realized. This advantage has to compensate for the previously mentioned difficulties for the concept to be attractive in the end [8].

1.3.2 *HELIOSTAT FIELD*

The Beam Down heliostat field consists of 33 ganged-type heliostats of 8.505 m^2 reflector area. Heliostats are arranged in a surrounding field configuration in three main sectors of equal size, North, East and West. Depending on their distance from the origin the heliostats are labeled (A, B or C) as shown in Figure 1-4. 6 heliostats are in the A line 17.48 m away from the origin, 15 heliostats are in the B line 20.08 m away from the origin and 12 heliostats in the C line 36.68 m away from the origin.

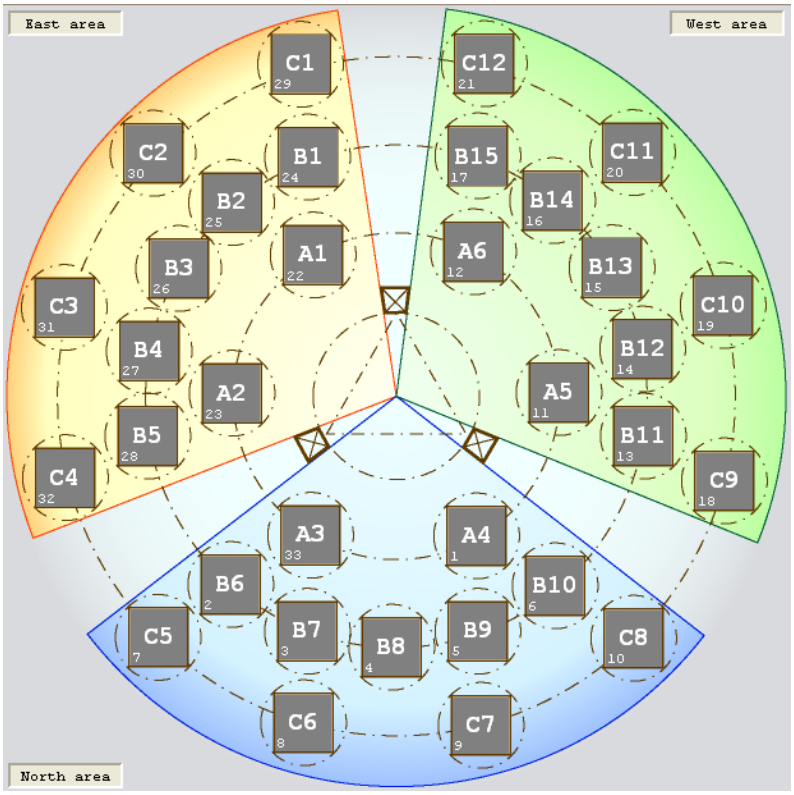

Figure 1-4 Heliostat Field Layout

The mirror facets of the heliostats are arranged in three banks each bank its own elevation axis of rotation as shown in Figure 1-5. A mechanical link connects the three banks together which allows elevation control using a single motor. A second motor is placed at the center of the heliostat and is used to rotate the whole platform holding the mirror banks axes parallel to ground plane, thus providing azimuth control for the heliostat.

Each mirror bank contains 14 mirror facets (450 mm x 450 mm) arranged in two rows. The middle bank has a central mirror and two half mirrors above and below it. The central mirror is called the control mirror because it is used, along with the tracking sensor, to control the position of the heliostat at each moment of time.

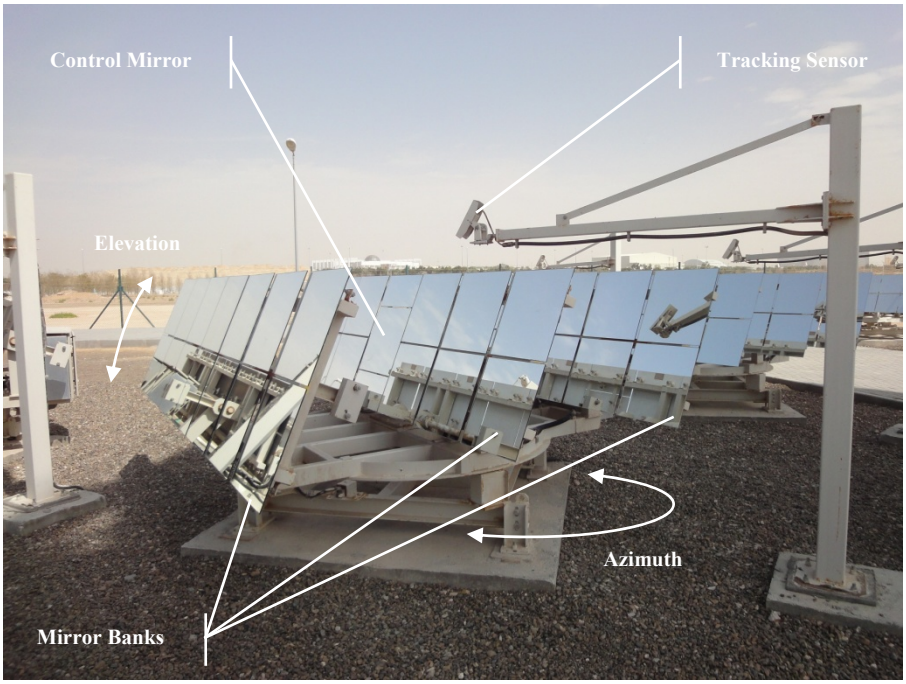

Figure 1-5 Typical ganged type heliostat and tracking sensor. The center of the control mirror, the tracking sensor and the focal point are aligned on a common line.

All heliostats should continuously change their elevation and azimuth angles so that solar radiation can be redirected towards the focal point. To do so, there are two tracking modes for heliostat positioning; one is the open loop or ephemeris mode. In this mode the heliostat controller will calculate the azimuth and elevation angles required at each point of time based on its location in the field, position of the sun and focal point. The sun position is calculated using well-known astronomical equations (see [10],[11] for details) that require precise knowledge of time, latitude and longitude. The heliostat control system uses a GPS to acquire the needed information. This open-loop control mode is used to roughly position the heliostat to the correct position. Fine adjustment is achieved by the feedback tracking sensor (see Figure 1-5) on which the second tracking mode is based. The sensor must be exactly coaxial with the line connecting

the center of the control mirror and the focal point. Hence, if the heliostat is tracking properly, the reflected radiation from the control mirror should enter parallel to the sensor axis. The sensor has four photosensitive cells arranged in a circle 90^{o} apart, unless the radiation enters parallel to the sensor axis, the cells won't give the same output, and the heliostat control system can adjust the position accordingly.

Since all the heliostat facets are flat, they have to be tilted relative to each other to focus the solar radiation; this process is called canting. The tilt angles of the mirrors depend on the distance between the heliostat and the focal point.

More details on the alignment of the tracking sensor and the heliostat canting can be found in chapter 6.

1.3.3 *FLUX MEASUREMENT SYSTEM*

In order to characterize the performance of the BDSTC, it is necessary to study the flux levels and distribution in the focal plane. This is an important step for receiver design and/or secondary concentrator design. It is also essential for optical alignment tests and commissioning of such a system.

To study energy flux distribution and its magnitude, concentrated solar radiation is intercepted by a 5m x 5m ceramic tile target, located 2.3m above ground level. These white tiles can withstand the high flux levels and are highly reflective in a diffuse manner approximating a Lambertian target. This allows a CCD camera located at the top of the tower to measure the distribution of luminous intensity. Embedded within the tiles at eight locations are heat flux sensors (HFS) to measure the concentrated solar flux. The HFSs only provide discrete flux data

and the CCD camera provides data of the luminous intensity on the target. A correlation is developed between the flux sensor data and the CCD camera data so that an accurate measurement of flux distribution can be obtained. In this way enough information of flux distribution on the focal plane can be acquired at each moment of time which allows the study of the plant's performance under various conditions.

It is necessary to control the temperature of the CCD camera to ensure that sensitivity of the sensing elements does not change during the measurement. The CCD camera temperature and humidity are thus controlled by a combination of heating and cooling devices. A PID controller regulates the air pressure supplied to a vortex cooler in order to keep the CCD camera temperature constant at around 23^{o}C. Air for the vortex cooler is supplied by a screw compressor and is passed through a drier to prevent any condensation in the CCD camera box. The heating element is used to raise the temperature of the box when ambient temperature drops below the set point.[12]

HFSs used in our measurement system also require cooling. Water cooling is used, where water is supplied from a well-insulated tank with enough thermal mass to prevent any abrupt change in the water temperature. For the sake of accurate measurement, it is more important to settle down transients in water temperature rather than keeping it precisely at certain set point. The water temperature going into the sensors and the outlet temperature of each sensor are recorded and then used in correcting the HFS output as needed using a correction model developed in the context of this work and discussed in greater detail in Chapter 3.

CHAPTER 2

GEOMETRICAL-OPTICS MODEL AND ERROR ANALYSIS OF CONCENTRATED FLUX DISTRIBUTION FROM A SINGLE HELIOSTAT

In this chapter we present a geometrical-optics model that was developed to study the concentrated flux distribution of the Beam-Down heliostats. More specifically, the model is required to get insight into the causes of the comatic aberrations noticed in the heliostats images on the target plane. The model is also employed to study the effect of heliostat facets canting on the quality of concentration and on the spillage of radiation around the central reflector mirror.

The heliostat facets and the CR facets are all flat mirrors; hence the optics can then be modeled using geometry and vector algebra. Compared to stochastic modeling (e.g. ray tracing) not only is the proposed model faster but also it yields better understanding of the causes of the

aberrations and of the propagation of optical errors. However it provides a less accurate representation of the true flux distribution maps. Flux maps can be obtained experimentally or using commercial ray tracing tools.

There are several commercial/research codes available for calculating flux distribution of central receiver plants. A comprehensive review of these codes is presented in [13]. Although many of the available codes are powerful and can produce accurate performance assessment, we opted to develop our own code in order to focus on representing and studying the unique aspects of the Beam-Down optics and the ganged-type heliostats used. This is added to the potential of reducing the computation time compared to generalized codes.

The heliostat flux distribution problem has been studied using analytical methods by Lipps [14]. He presented four different methods for formulating the heliostat density function integral. The pin-hole view is the closet to the approach that we follow, where the flux density integral is approximated as the convolution of the image due to a point sun with the real sunshape. Consequently, all errors, whether they result from tracking, optics or sunshape can be treated as if they are a result of tracking errors.

Igel and Hughes [15] presented a method for approximating the image size cast by heliostats on the target. Using Coddington equations they have presented an analysis of astigmatism, which is the major aberration describing optical off-axis image behavior for concentrating systems [15].

Collado et al.[16] presented an analytical model for the flux density due to a focused heliostat over the receiver plane of a tower solar plant. The model is based on several simplifying assumptions in order to achieve an analytical solution. Mainly they assumed that the sunshape is

represented by a Gaussian distribution and that the heliostats have on-axis alignment. They thus obtain an exact analytical convolution. However since we need to study the effect of different canting angles and varying sunshape and error distributions this approach cannot be adopted.

2.1 COORDINATE SYSTEM

A schematic of the Beam Down heliostat field and tower is shown in Figure 2-1, the origin point of the global coordinate system is taken at the center point at ground level, the positive X-axis is due north and the positive Y-axis is due east and the positive Z-axis is pointing upwards.

A local coordinate system used for each heliostat is used; the local axes (x, y and z) are parallel to the global axes and the origin point is taken at ground level in the center of the heliostat (i.e. on the azimuth rotation axis of the heliostat).

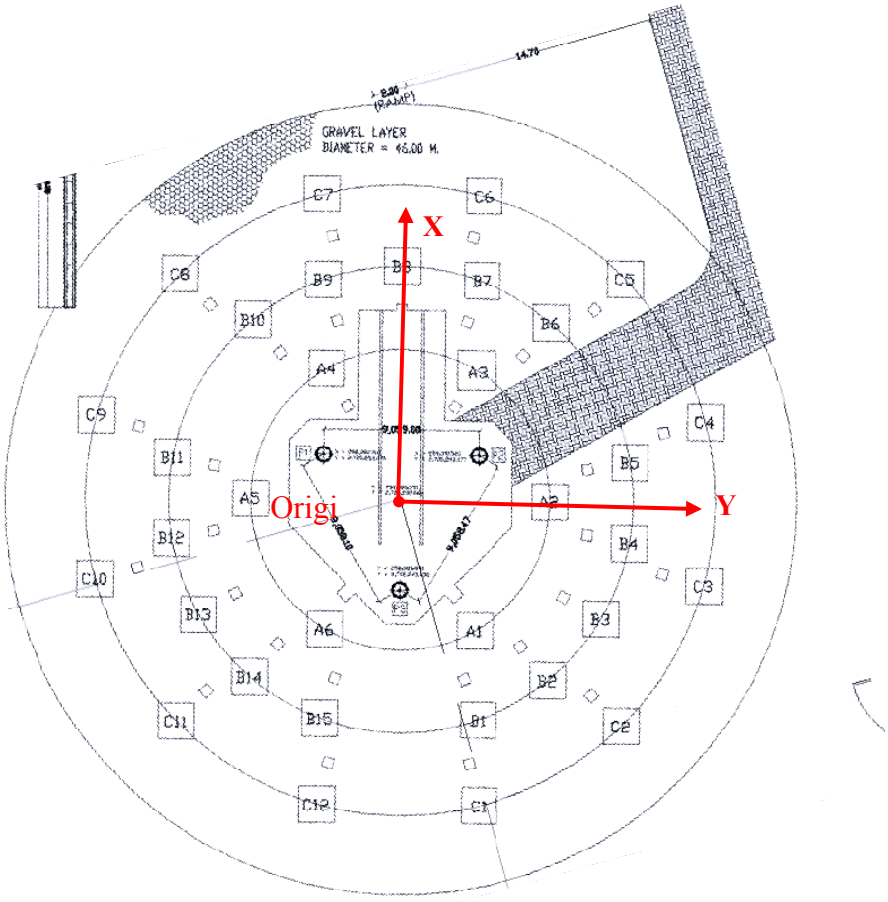

Figure 2-1 Schematic of the Beam Down Heliostat Field and Tower Position for Definition of the Global Coordinate System

The heliostat elevation angle is the angle between the control mirror surface normal and the x-y plane, so that when the heliostat is pointing upwards (i.e. flat) the elevation angle will be 90^{o}. The azimuth angle is the angle that any of the elevation axes make with the y-axis in the x-y plane, measured positive clockwise.

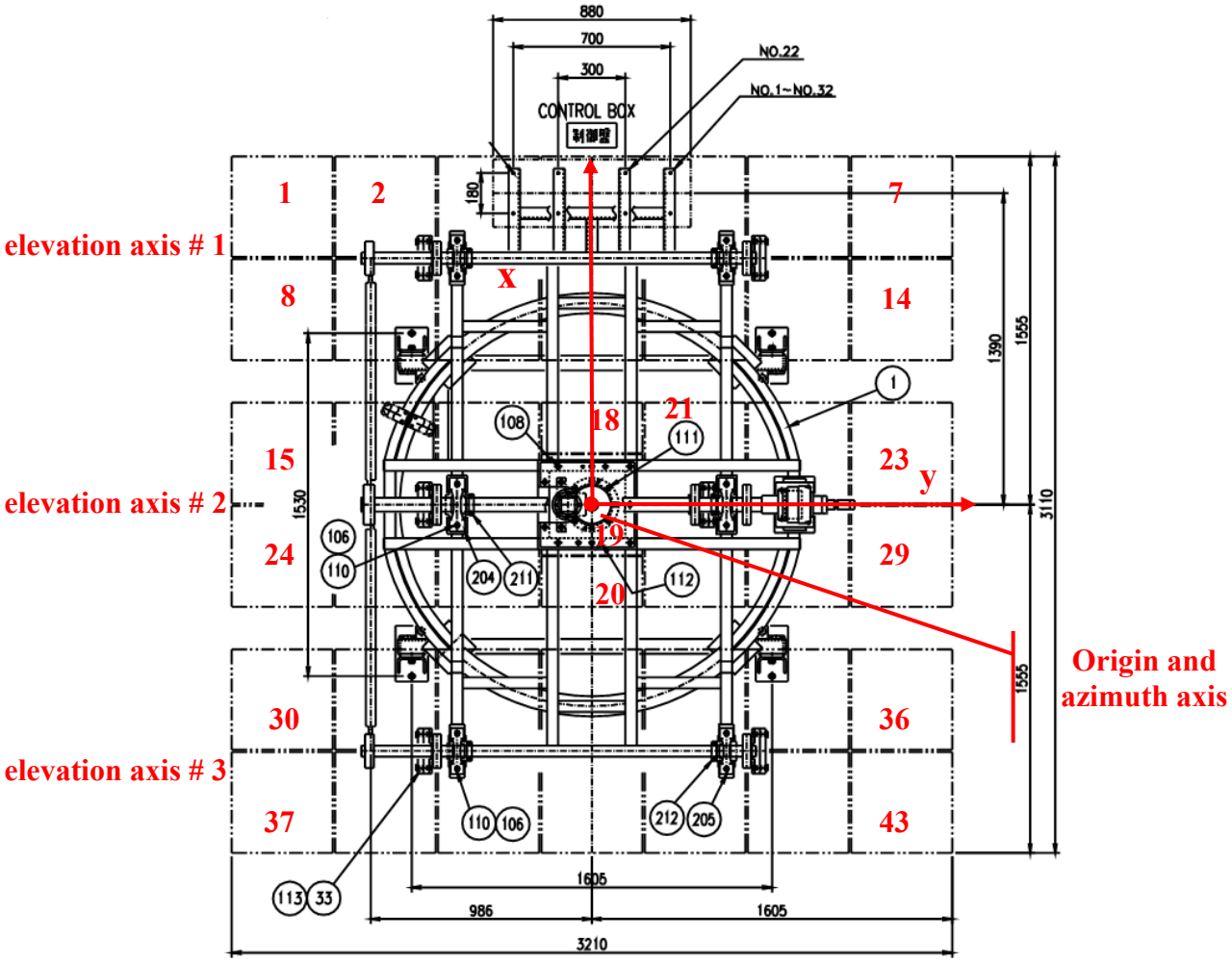

Figure 2-2 Schematic of a Heliostat and the Local Coordinate System (Figure courtesy of MES)

2.2 Defining Heliostat Geometry

The first step in modeling is to define the heliostat geometry and the way this geometry changes with changes in elevation and azimuth angles of the heliostat. This requires the knowledge of the position and orientation of each of the 43 heliostat mirror facets (41 normal size + 2 half size). Firstly, the center of each facet is defined assuming that the heliostat is at 90^{o} elevation and 0^{o}

azimuth (we call this our reference position). Secondly, at the reference position, we define the unit normal of each facet; this is done using the canting angles of the heliostat relative to the control mirror, which is level in the reference position.

Facet center and unit normal provide complete information about the position and orientation of each facet in the reference position. Subsequently, we adjust these values for the actual position of the heliostat. A correction is made for the elevation angle first and then for azimuth angle, i.e. as if the heliostat first moves in elevation and then in azimuth. This strategy is chosen for implementation convenience.

2.2.1 *POSITIONS OF FACET CENTERS AT DIFFERENT ELEVATION AND AZIMUTH ANGLES*

Since the facets are arranged in three banks with separate elevation axes, it is necessary to correct for each bank alone. The facet centers are given in the local coordinate system of the heliostat, so we will first move them to another coordinate system where the elevation axis of each bank coincides with the y-axis of that coordinate.

If c_k is the position vector of the center of the k^{th} facet in the heliostat local coordinate and e_1,e_2,e_3 are the vectors pointing to the centers of the elevation axes in the same coordinate system, then the facet centers relative to the elevation axes are given by,

$$c_k' = c_k - e_i \qquad 2\text{-}1$$

where k is the facet number from 1 to 43, i is the elevation axis number. For k=1 to 14 i=1, for k=15 to 29 i=2 and for k=30 to 43 i=3, see Figure 2-2. Next we rotate these centers around the elevation axes using the y-axis rotation matrix:

$$c_k' = R_y(\theta_{ele} - 90)c_k' \quad (2\text{-}2)$$

where θ_{ele} represents the elevation angle and the counterclockwise rotation matrix around the y-axis, $R_y(\theta)$, is given by:

$$R_y(\theta) = \begin{bmatrix} \cos(\theta) & 0 & \sin(\theta) \\ 0 & 1 & 0 \\ -\sin(\theta) & 0 & \cos(\theta) \end{bmatrix} \quad (2\text{-}3)$$

The new facet centers are referenced to the heliostat local coordinate system:

$$c_k = c_k' + e_i \quad (2\text{-}4)$$

Now we can correct for the azimuth angle, since all the facets are rotated on the same azimuth axis (z-axis), the rotation is performed once without distinction as follows:

$$c_k = R_z(\theta_{azi})\, c_k \quad (2\text{-}5)$$

where θ_{azi} is the azimuth angle of the heliostat and the counterclockwise rotation matrix around the z-axis, $R_z(\theta)$, is given by:

$$R_z(\theta) = \begin{bmatrix} \cos(\theta) & -\sin(\theta) & 0 \\ \sin(\theta) & \cos(\theta) & 0 \\ 0 & 0 & 1 \end{bmatrix} \quad (2\text{-}6)$$

2.2.2 *FACET TILT ANGLES AND ROTATION OF FACETS' UNIT NORMAL FOR ELEVATION AND AZIMUTH ANGLES*

The tilt angles of the heliostats are determined by first pointing the heliostat towards the focal point so that the line connecting the control mirror center and secondly by assuming that the focal point line is perpendicular to the surface of the control mirror. Then the other facets are tilted in such a way that the lines, originating from their centers and perpendicular to their plane,

will all intersect at a point which is twice the focal length of the heliostat. This procedure is called on-axis canting. These angles define the unit normal of each heliostat facet $\hat{n}_k$.

The unit normal is first defined on the reference position and then corrected for elevation and azimuth using the rotation matrices similar to what we have done for facet center position vectors:

$$\hat{n}_k = R_y(\theta_{ele} - 90)\hat{n}_k$$
$$\hat{n}_k = R_z(\theta_{azi})\hat{n}_k \qquad 2\text{-}7$$

2.3 GEOMETRICAL OPTICS MODEL

Since the control mirror orientation is controlled by the tracking sensor, it will ideally direct sunlight towards the focal point at all times. If we denote the reflected radiation from each facets as $\hat{r}_k$, the unit reflected vector. Then the unit reflected vector of the control mirror is given by $\hat{r}_{19} = \frac{f}{|f|}$, where f is the vector pointing to the upper focal point in the global coordinate system.

Using the reflection law we can calculate the position of the sun for each position of the heliostat since we know the unit normal of the control mirror $\hat{n}_{19}$ and the unit reflected $\hat{r}_{19}$.

$$\hat{s} = 2(\hat{r}_{19}.\hat{n}_{19})\hat{n}_{19} - \hat{r}_{19} \qquad 2\text{-}8$$

Where $\hat{s}$ is a unit vector pointing towards the center of the sun. Knowing the position of the sun and the unit normal for all the facets we can apply the same reflection law for all of the remaining facets to determine the orientation of their unit reflected.

$$\hat{r}_k = 2(\hat{s}.\hat{n}_k)\hat{n}_k - \hat{s} \qquad 2\text{-}9$$

The next step consists in solving for the intersection point of the reflected radiation from each facet with the corresponding CR mirror. The reflected radiation line can be represented in a parametric equation as follows:

$$x = c_{x,k} + t\hat{r}_{x,k}$$
$$y = c_{y,k} + t\hat{r}_{y,k} \qquad 2\text{-}10$$
$$z = c_{z,k} + t\hat{r}_{z,k}$$

Where the subscripts x,y,z represent the components in the corresponding axes. And the subscript k is the facet number.

The CR mirror surface can be represented by using the following general equation:

$$ax + by + cz + d = 0 \qquad 2\text{-}11$$

To find the intersection points ($P_{CR,k}$) of each ray with the CR mirror we have to solve the following system of equations for each facet k:

$$\begin{bmatrix} a & b & c & 0 \\ 1 & 0 & 0 & -\hat{r}_{x,k} \\ 0 & 1 & 0 & -\hat{r}_{y,k} \\ 0 & 0 & 1 & -\hat{r}_{z,k} \end{bmatrix} \begin{bmatrix} x_k \\ y_k \\ z_k \\ t_k \end{bmatrix} = \begin{bmatrix} -d \\ c_{x,k} \\ c_{y,k} \\ c_{z,k} \end{bmatrix} \qquad 2\text{-}12$$

The intersection points are given by $P_{CR,k} = [x_k\ y_k\ z_k]^T$. The CR unit normal can be readily found from the plane equation of the CR mirror as follows:

$$\hat{n}_{CR} = \frac{[a\ b\ c]^T}{\sqrt{(a^2 + b^2 + c^2)}} \qquad 2\text{-}13$$

Using the CR surface normal and the intersection points determined earlier, in addition to the vectors of the reflected radiation from the heliostat facets $\hat{r}_k$ we can infer the reflected radiation from the CR mirror towards the target $\hat{g}_k$.

$$\hat{g}_k = 2(\hat{r}_k . \hat{n}_{CR})\hat{n}_{CR} - \hat{r}_k \quad \text{2-14}$$

Finally we calculate the intersection points with the target following the same procedure illustrated for the intersection points with the CR mirror. The target is a flat surface parallel to the x-y plane, hence the target equation is $z=h_T$, Where h_T is the height of the target measured from ground level. Thus to find the points of intersection with the target ($P_{T,k}$) we solve the following system k times:

$$\begin{bmatrix} 0 & 0 & 1 & 0 \\ 1 & 0 & 0 & -\hat{g}_{x,k} \\ 0 & 1 & 0 & -\hat{g}_{y,k} \\ 0 & 0 & 1 & -\hat{g}_{z,k} \end{bmatrix} \begin{bmatrix} x_k \\ y_k \\ z_k \\ t_k \end{bmatrix} = \begin{bmatrix} h\_T \\ P_{CR,x,k} \\ P_{CR,y,k} \\ P_{CR,z,k} \end{bmatrix} \quad \text{2-15}$$

Then the intersection points are given by $P_{T,k} = [x_k\, y_k\, z_k]^T$.

2.4 HELIOSTAT POSITIONING

The heliostat positions itself in a way that allows it to redirect solar radiation to the focal point; to accomplish that, it is necessary to calculate the heliostat's zenith and azimuth angles at each point of time. This is the task of the tracking system. In our model, astronomical equations are used to determine the sun position at each moment of time (Sun position equations are readily found in standard solar engineering books e.g. [10] and [11]). The obtained sun position is used to determine the required heliostat position as a function of time.

Calculating the control mirror unit normal $\hat{n}_{19}$ will completely define the heliostat position; relative to it all other mirror unit normals can be determined. If we assume that the solar radiation falling on the center of the control mirror is in the direction of $\hat{s}$, the sun position vector, and that reflected radiation is in the direction $\hat{r}_{19}$, then $\hat{n}_{19}$ can be calculated.

Two equations are required to define the orientation of $\hat{n}_{19}$. Since the control mirror surface normal ($\hat{n}_{19}$), the sun vector ($\hat{s}$) and the vector pointing from the heliostat to the focal point ($\hat{r}_{19}$) are coplanar we get the first equation:

$$(\hat{s}X\hat{r}_{19}).\hat{n}_{19} = 0 \qquad 2\text{-}16$$

Our second equation comes from the equality between angle of incidence and angle of reflection, hence:

$$\hat{s}.\hat{n}_{19} = \hat{r}_{19}.\hat{n}_{19} \qquad 2\text{-}17$$

Finally, solving for $\hat{n}_{19}$ we can now calculate the required heliostat azimuth and elevation angles as follows:

$$\theta_{ele} = tan^{-1}\left(\frac{\hat{n}_{19_z}}{\sqrt{\hat{n}_{19_x}^{\,2} + \hat{n}_{19_y}^{\,2}}}\right) \qquad 2\text{-}18$$

$$\theta_{azi} = tan^{-1}\left(\frac{-\hat{n}_{19_y}^{\,2}}{\hat{n}_{19_x}^{\,2}}\right) \qquad 2\text{-}19$$

2.5 Optical Analysis and Error Propagation

The optical model of any CSP plant aims at predicting the solar radiation intercepted by the receiver in addition to its distribution. In analytical models of tower plants it is convenient to split the equation describing the geometry of the plant into five terms as follows:

- Cosine factor resulting from reduced effective reflective area due to non-zero angle of incidence.
- Overall reflectance (and transmittance) of the optical surfaces in the path of the redirected beam.
- Atmospheric attenuation of the beam travelling from the heliostat to the receiver.
- Blocking and shading between neighboring heliostats.
- Intercept factor which is the percentage of reflected radiation that will eventually hit the receiver, while the rest represents spillage.

The intercept factor captures most of the important effects influencing the radiation falling from the sun until it strikes the target. The intercept factor (γ) is defined as the fraction of radiation that is incident on the receiver of a solar concentrator taking into account all the effects that cause beam broadening. Intercept factors can be calculated by convoluting the optical errors of the concentrator, the angular solar flux distribution (sunshape) and the angular acceptance function (f) of the concentrator. Angular acceptance functions are geometrical functions of concentrators and they represent the fraction of rays that would hit the receiver if the optics and sunshape were perfect [17].

Pioneering work in the analytical modeling of solar concentrators was done in the late 1970s and the 1980s [17-21], models for intercept factor for parabolic trough and dishes were proposed, and to some extent similar models exist for regular tower plants.

In the following sections we will review the previous work done in the field of analytical modeling of solar concentrators and apply some of the concepts to model the Beam Down. One of the biggest obstacles in such an approach is the difficulty of representing the Beam Down

optics in a closed-form mathematical model; this is because unlike parabolic troughs and parabolic dished, central receiver plants have complicated changing geometry during operation, which is cumbersome to represent by means of simple mathematical functions. Nevertheless it proves advantageous to follow the procedure employed in modeling such concentrators and apply the outlines to a simplified computational scheme.

2.5.1 *INTERCEPT FACTOR*

The intercept factor (γ) is the integral of the product of the angular acceptance function of the collector (f) and the effective source (B_{eff}). While the effective source is the convolution of the optical errors and the angular distribution of the solar radiation (sunshape), the intercept factor is reads:[17]

$$\gamma = \int_{-\infty}^{+\infty} f(\theta) B_{eff}(\theta)\, d\theta \qquad 2\text{-}20$$

The effective source is described by the equation: [17]

$$B_{eff}(\theta) = \int_{-\infty}^{+\infty} \frac{1}{\sigma_{optical}\sqrt{2\pi}} * exp\left(-\frac{\theta'^2}{2\sigma_{optical}^2}\right) * B_{sunshape}(\theta - \theta')\, d\theta' \qquad 2\text{-}21$$

where γ is the intercept factor, f is the angular acceptance function of the, θ is the angular deviation of the falling ray from the ideal ray. For perfect optics and ideal point source θ will be zero mrad, B_{eff} is the effective source W/m^2/str, $B_{sunshape}$ is the angular solar distribution W/m^2/str, $\sigma_{optical}$ is the RMS width of the optical errors normal distribution mrad.

In the case of parabolic dishes, the effective source is given by the convolution in 3D that reads :[19]

$$B_{eff}(\theta_x,\theta_y) = \int\int_{-\infty}^{+\infty} \frac{1}{\sigma_{x,optical}\sigma_{y,optical}(2\pi)} exp\left(-\frac{\theta x'^2}{2\sigma_{x_{optical}}^2} - \frac{\theta y'^2}{2\sigma_{y_{optical}}^2}\right) B_{sunshape}(\theta - \theta' d\theta x'.d\theta y' \quad 2\text{-}22$$

Where we assume Gaussian optical errors and azimuthally symmetrical sunshape although the optical errors are allowed to be non-azimuthally symmetric.

Taking an effective optical error averaged over the whole aperture and assuming rotational symmetry of the errors the intercept factor can be reduced to a single integration using:

$$\gamma = \int_0^{+\infty} 2\pi\theta\, f(\theta) B_{eff}(\theta)\, d\theta \quad 2\text{-}23$$

Further simplification for a Gaussian sunshape is shown in [19].

Optical errors can be summarized in four categories, contour errors which are a result of the imperfection in the manufacturing process in reproducing the required geometrical shape, specular errors due to the imperfect reflection of the mirror, displacement error resulting from the misalignment between the receiver and the foal line of the parabola in addition to errors originating from the tracking system. If the errors are defined by their respective standard deviations the total effective optical error is given by:

$$\sigma_{eff}^2 = \sigma_{eff\_contour}^2 + \sigma_{specular}^2 + \sigma_{tracking}^2 + \sigma_{displacment}^2 \quad 2\text{-}24$$

2.5.2 *ANGULAR ACCEPTANCE FUNCTION*

As defined earlier, the angular acceptance function is a geometrical function that represents the fraction of rays that would hit the receiver if the optics and sunshape were ideal [17]. For

example, the angular acceptance function of a parabolic trough with a cylindrical receiver can be represented in closed form by the equation below from [20], where C is the concentration ratio, φ is the rim angle, and θ is the angle of incidence.

$$f(\theta) = \begin{cases} 1, & for\ |\theta| < \theta_1 \\ \cot\left(\frac{\phi}{2}\right)\left(\frac{2\tan\left(\frac{\phi}{2}\right)}{\pi C\theta} - 1\right)^{\frac{1}{2}}, & for\ \theta_1 < |\theta| < \theta_2 \\ 0, & for\ |\theta| > \theta_2 \end{cases} \qquad 2\text{-}25$$

$$with\ \theta_1 = \frac{\sin(\phi)}{\pi C}\ and\ \theta_2 = \frac{2\tan\left(\frac{\phi}{2}\right)}{\pi C}$$

Similarly the angular acceptance function of a parabolic dish is exact and can be expressed in closed form for a spherical receiver, for a flat receiver the exact solution is complicated and a polynomial expansion is given by [19]. The polynomial expansion approximates the angular acceptance function for parabolic dish with a flat receiver to a satisfactory accuracy.

For tower plants however, it is very complicated to represent the angular acceptance function in closed form solution. Furthermore a simple mathematical formula is not feasible due to the complexity of the interactions in the heliostat field and the non-modularity of central receiver plants. Based on that, in our analysis of the Beam Down we opted for a computational angular acceptance function.

2.5.3 *ERROR MAPPING BETWEEN SUN PLANE AND GLOBAL AZIMUTH AND ELEVATION COORDINATES*

The effective source is a representation of the errors of the concentrator and sunshape combined. It allows us to study their overall effect on concentration quality assuming that the concentrator is perfect, and that all errors come from a "degraded sun". The effective source is denoted by $B(\theta_x, \theta_y)$ or $B(w, v)$ in the plane of the sun, where w,v are the angles from the center of the sun along each of the axes, w and v.

The error resulting from the effective source (degraded sun) can be simulated by introducing an error in the heliostat tracking system. This is done by fixing the heliostat position at certain point in time, and applying a differential change on the sun vector, in elevation ($d\alpha$) and in azimuth ($d\phi$). To enumerate the simulation space, the effective source is scanned in two axes by varying $d\alpha$ and $d\phi$ at each point of time.

Since the effective source is defined in the plane of the sun, it is necessary to create a mapping between the plane of the sun and the global coordinates defined by the elevation and azimuth of the sun vector. Figure 2-3 illustrates the effective source plane; the center of the plane is where the ideal ray originates and where the ideal sun vector points at. dv, dw are elemental scans across the plane.

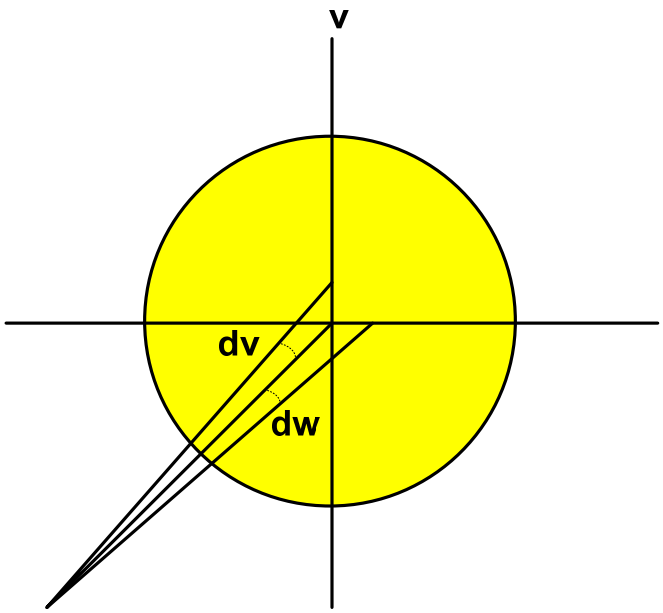

Figure 2-3 Elemental scanning of the sun plane, i.e the effective source

An elemental change in the *v* axis (*dv*) is directly proportional to an elemental change in the elevation angle of the heliostat (*dα*), this is because the two axis are parallel, hence:

$$d\alpha = dv \qquad 2\text{-}26$$

A scan in the w-axis is more complicated. In Figure 2-4, it can be seen that a change in the *w* axis (*dw*) depends on the elevation angle. Hence, in order to scan in the *w*-axis without affecting v-axis, a modification in the azimuth (ϕ) and elevation (α) angles is required. To find $d\phi$, from Figure 2-4, the small distance l is given by:

$$l = Rdw = rd\phi = \mathrm{R}\cos(\alpha)\, d\phi$$

Hence we can write,

$$d\phi = \frac{Rdw}{Rcos(\alpha)} = \frac{dw}{\cos(\alpha)} \qquad 2\text{-}27$$

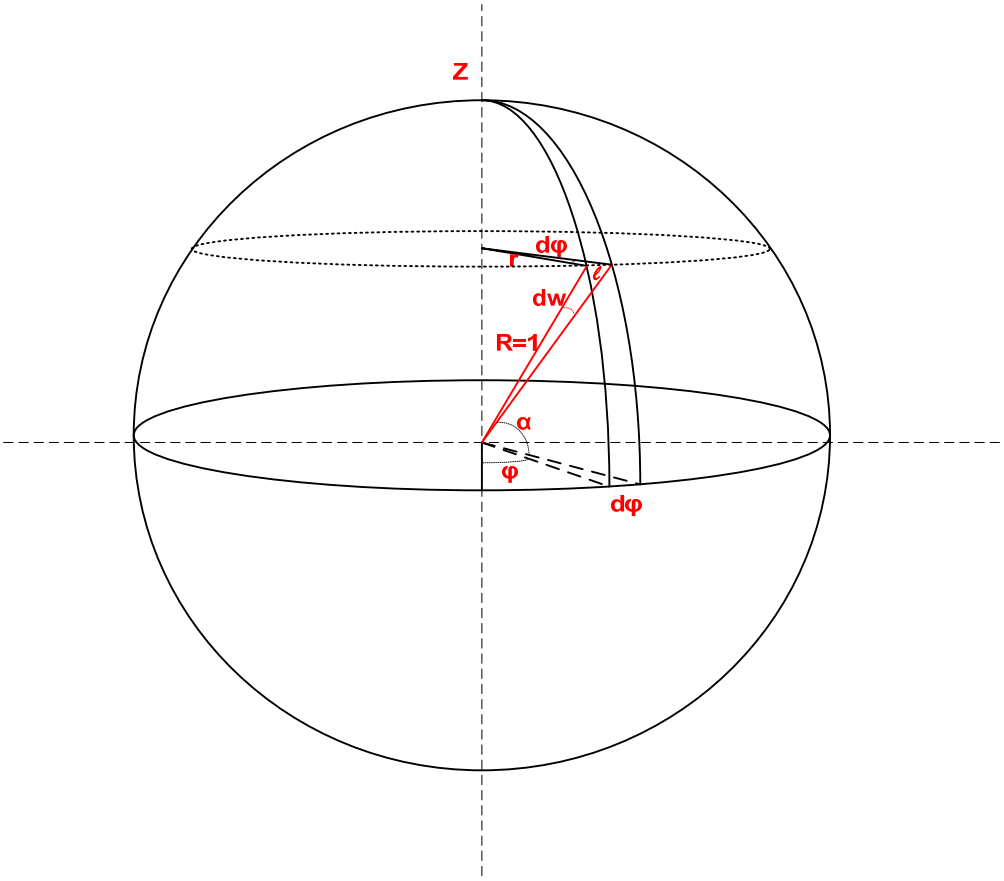

Figure 2-4 Differential change dϕ in global coordinates relative to the change dw in sun plane

The change in elevation angle ($d\alpha$) due to the change dw is illustrated in Figure 2-5, the increase $d\phi$ in the azimuth angle will require changing the elevation angle from $cos^{-1}(r/R)$ to $cos^{-1}(m/R)$ in order to remain on the sun plane without producing a change in dv. This change however is small and is given by:

$$d\alpha = \cos^{-1}\left(\frac{m}{R}\right) - \cos^{-1}\left(\frac{r}{R}\right)$$

(2-28)

$$= \cos^{-1}\left(\frac{\cos(\alpha)}{\cos(d\phi)}\right) - \cos^{-1}\left(\frac{r}{R}\right)$$

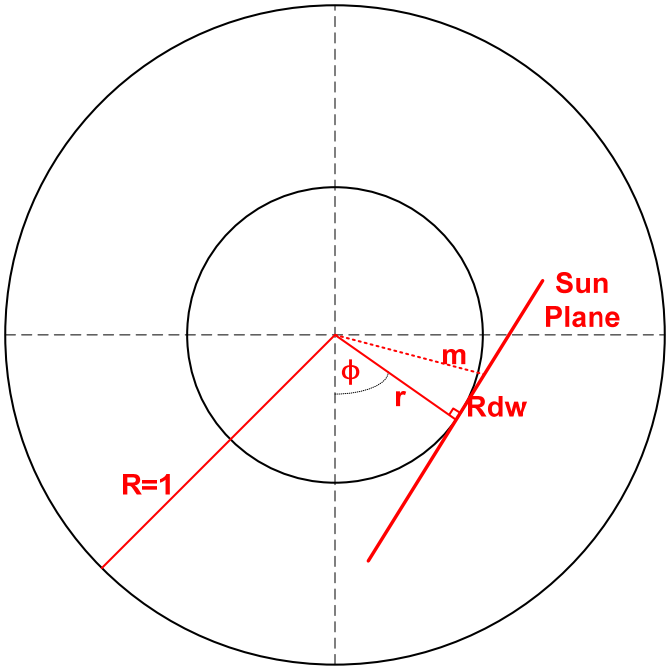

Figure 2-5 Top view of Figure 2-4 illustating the change in elevation angle due to the change dw (angles are exagurated for clarity)

Finally, the total change in elevation angle ($d\alpha$) is equal to the sum of the two differential changes due to *dw* and *dv*. Now we can map the changes in the sun plane into changes in elevation and azimuth in the global coordinate system.

2.6 Model Application to the Beam-Down B8 Heliostat

In this section we present the results of applying the aforementioned model on one of the heliostats of the Beam-Down. Using the model we can calculate the approximate shape of the

flux generated by a single heliostat at each point of time in addition to assess the effect of several error sources on the concentration quality. The parameters used for heliostat B8 are summarized in Table 2-1.

Table 2-1 Summary of model parameters for heliostat B8

Model Parameters					
a) Parameters in Global Coordinates					
Upper focal point (mm)			[0;0;20300]		
Target center point (mm)			[0;0;2300]		
B8 CR mirror center (mm)			[2850;0;16300]		
B8 CR Mirror tilt angle (measured from x-axis) (^{o})			12.1		
Heliostat local origin (mm)			[13540;0;0]		
b) Parameters in Heliostat Local Coordinates					
Center of elevation axis #1 (mm)			[1100;0;1321]		
Center of elevation axis #2 (mm)			[0;0;1321]		
Center of elevation axis #3 (mm)			[-1100;0;1321]		
c) Facets tilt angles in Reference Position					
Facet Number	**θx [^{o}]**	**θy [^{o}]**	**Facet Number**	**θx [^{o}]**	**θy [^{o}]**
1	-1.45	-1.65	23	-0.3	1.15
2	-1.45	-1.15	24	-0.3	1.65
3	-1.45	-0.55	25	0.3	-1.65
4	-1.45	0	26	0.3	-1.15
5	-1.45	0.55	27	0.3	-0.55
6	-1.45	1.15	28	0.3	0.55
7	-1.45	1.65	29	0.3	1.15
8	-0.85	-1.65	30	0.3	1.65
9	-0.85	-1.15	31	0.85	-1.65
10	-0.85	-0.55	32	0.85	-1.15
11	-0.85	0	33	0.85	-0.55
12	-0.85	0.55	34	0.85	0
13	-0.85	1.15	35	0.85	0.55
14	-0.85	1.65	36	0.85	1.15
15	-0.3	-1.65	37	0.85	1.65
16	-0.3	-1.15	38	1.45	-1.65
17	-0.3	-0.55	39	1.45	-1.15
18	-0.45	0	40	1.45	-0.55
19	0	0	41	1.45	0
20	0.45	0	42	1.45	0.55
21	-0.3	0.55	43	1.45	1.15
22	-1.45	-1.65			

Figure 2-6 is a visualization of the model applied on heliostat B8 at the reference position. The sun position is represented by the yellow line falling on the control mirror, the dashed black line adjacent to the sun vector represents a sun vector with errors (dα ,dϕ). Each of the red lines represents the surface normal of the heliostat 43 facets calculated at the given elevation and azimuth angles. The green lines depict the rays reflected from the center of each facet, then reflected again from the CR mirror (depicted in blue) and finally falling on the target 2.3 m above ground level. Intersection points on the receiver (red) and on the CR mirror (blue) are calculated. These are later used to compute the amount of radiation which does not hit the target.

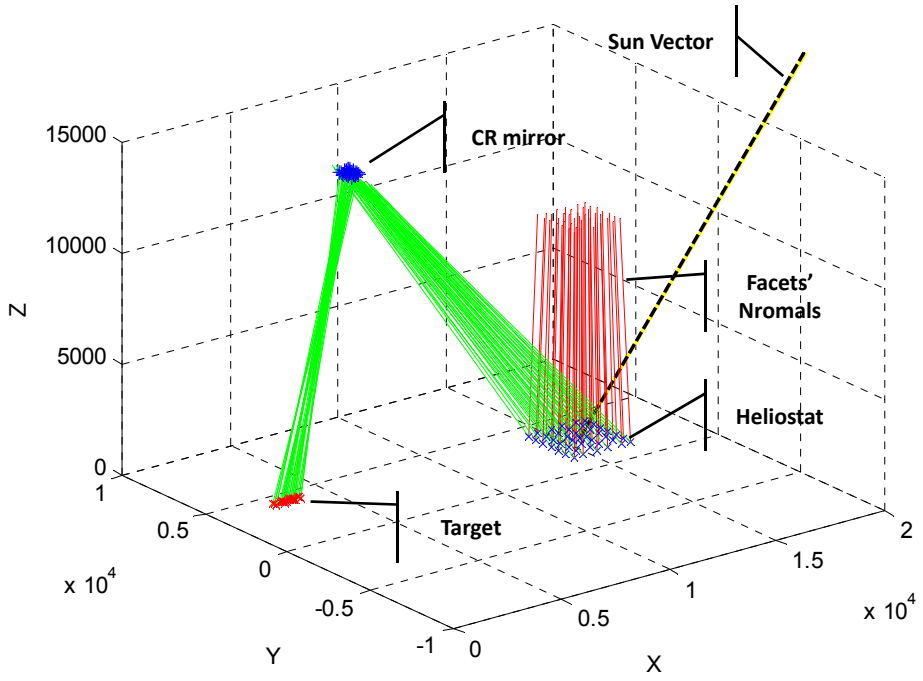

Figure 2-6 Visualization of the model applied to heliostat B8 in the reference position (i.e zero azimuth, 90^{o} elevation). Dimensions in (mm).

The approach discussed in section 2.5 will be employed to combine all error sources and sunshape into a single effective source distribution (B_{eff}). We will make use of equation 2-21 for this purpose, where we assume azimuthal symmetry of the effective optical errors.

The total error in the heliostat is given in [22] to be 3.7 mrad, this error originates from errors in heliostat mirror facets, tracking sensor error, vibration and tracking system, the error in the central reflector mirror is 0.55 mrad [22]. Hence the total effective error is $(3.7^2 + 0.55^2)^{0.5}$ = 3.74 mrad.

For the sunshape we will assume a CSR ratio (CSR is the ratio of circumsolar irradiation to the total irradiation) of 5% and we will use Neumann standard profiles given in [23]. The sunshape, effective errors distribution and the resulting effective source are depicted in Figure 2-7.

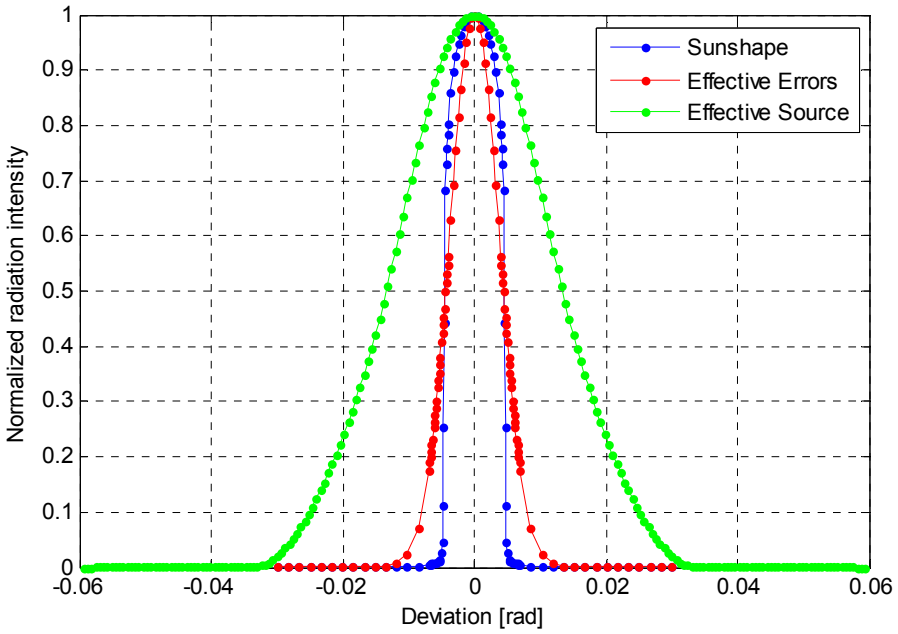

Figure 2-7 Sunshape, effective errors and the resulting effective source distribution

The error resulting from the non-ideal effective source is illustrated in Figure 2-8, which shows the deviation of facets' centers from their location assuming an ideal effective source (point-source). The deviation is shown for different heliostat facets and for different sun positions. It can be seen that the error is not varying much with sun position nor with different facets. This is due to the fact that the change in path length traveled by the beam during different heliostat positions does not change significantly, and hence the image spread is not significant. A more significant effect that depends on heliostat position results from off-axis aberrations and astigmatism as it will be shown later in this chapter.

It can also be observed that the curves are discontinuous or missing for some facets at certain sun-positions/deviations. This indicates that the ray does not get intercepted by the CR mirror (misses the mirror); hence it is removed from the graph.

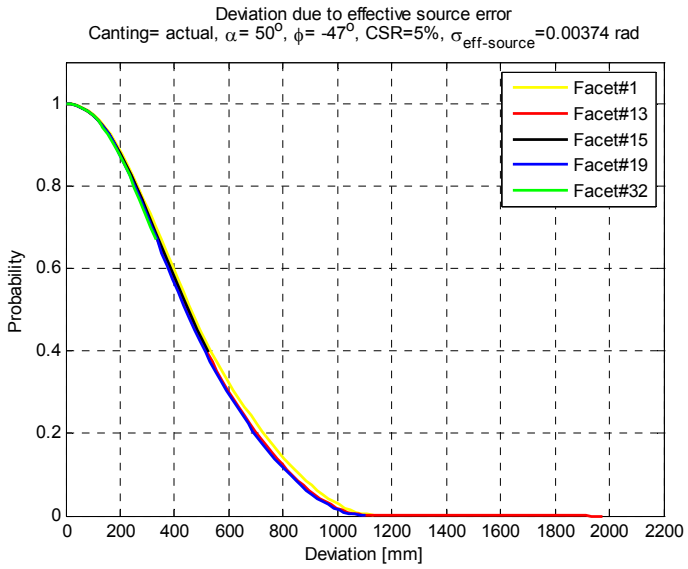

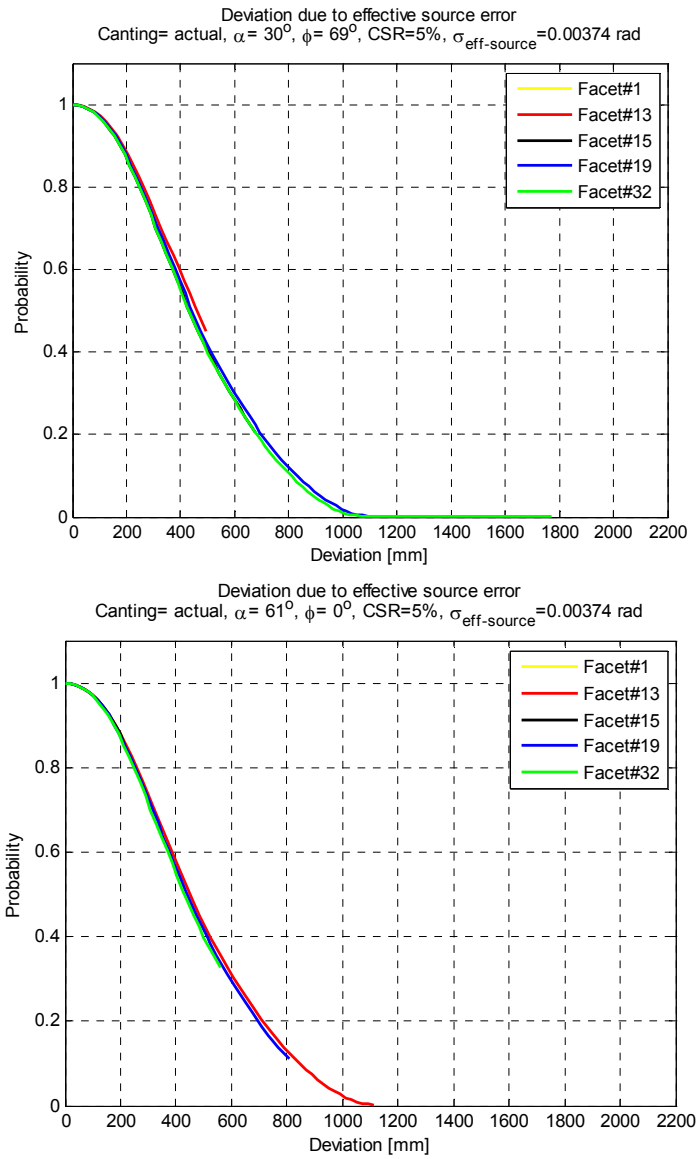

Figure 2-8 Error in various facets of B8 heliostats at different sun positions. Deviation is the distance between the location of the facet center at target plane assuming an ideal effective source compared to using the actual effective source. This deviation does not include the effect of aberrations.

In Figure 2-9-left we can see the deviation of facet centers from the ideal position at origin and for different sun positions. The facet centers are shown for an ideal effective source in red, and including an effective error in azimuth and elevation in blue.

The spread in facets centers at noon is mainly due to the used canting angles, something which will be discussed later. The canting angles at which these graphs were calculated are the actual canting angles employed in the field.

On the right side of Figure 2-9, the actual flux maps taken by the CCD are shown, these flux maps were obtained at the corresponding sun position. Visually comparing the simulated and actual flux maps, one can infer that the model is able to predict off-axis aberrations (occurring at non-normal angles of incidence). In addition the size of the actual heliostat image is a bit larger than the simulated image. This is expected since the model only traces the facets' centers and not the edges.

Our modeling procedure allows generating a more detailed image of the heliostat focus but it requires significantly higher simulation time than needed to produce only a map of centers. The map of the centers however enables rapid prediction of the change in the heliostat image at different sun positions and the aberrations associated with that image.

Furthermore, the model computes the percentage of lost radiation that does not fall on the CR mirror corresponding to the heliostat in question. One can see that spillage is minimum at noon (second plot) and increases as it deviates from that point. In the actual flux maps we can see some of the radiation reflected by the wrong CR mirror around the heliostat main focus, the intensity of this scattered radiation is seen to increase with the spillage percentage reported by the model. At noon spillage is very small while the intensity increases in morning and afternoon.

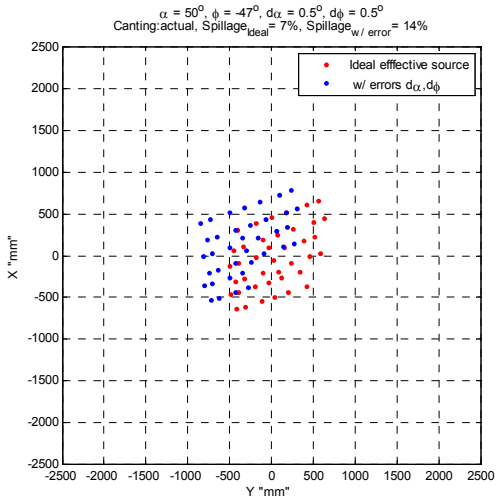
α = 50°, ϕ = -47°, dα = 0.5°, dϕ = 0.5°
Canting:actual, Spillage_Ideal= 7%, Spillage_w/ error= 14%
Ideal efffective source
w/ errors dα,dϕ
X "mm"
Y "mm"

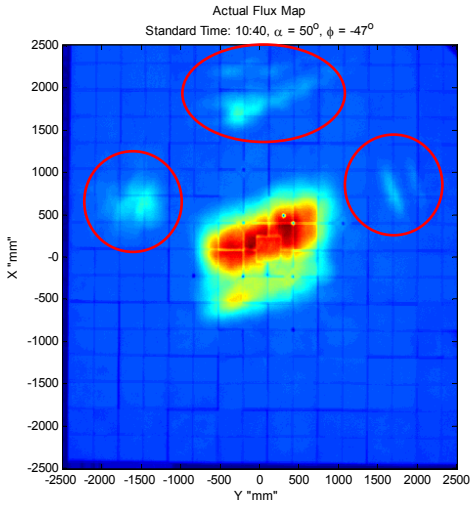
Actual Flux Map
Standard Time: 10:40, α = 50°, ϕ = -47°
X "mm"
Y "mm"

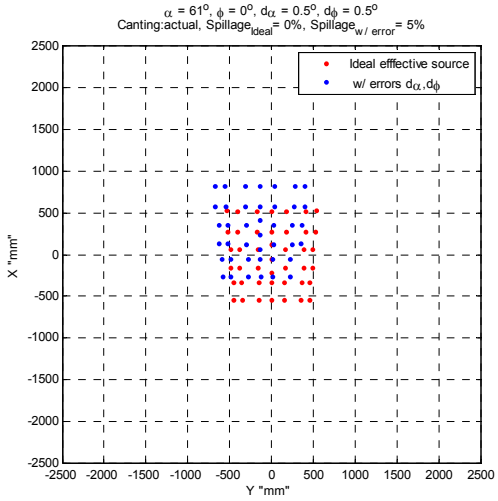
α = 61°, ϕ = 0°, dα = 0.5°, dϕ = 0.5°
Canting:actual, Spillage_Ideal= 0%, Spillage_w/ error= 5%
Ideal efffective source
w/ errors dα,dϕ
X "mm"
Y "mm"

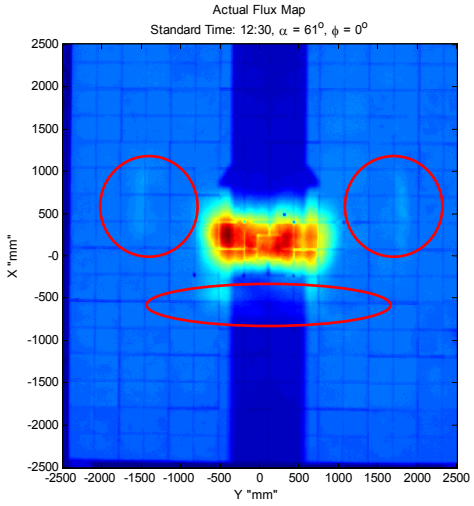
Actual Flux Map
Standard Time: 12:30, α = 61°, ϕ = 0°
X "mm"
Y "mm"

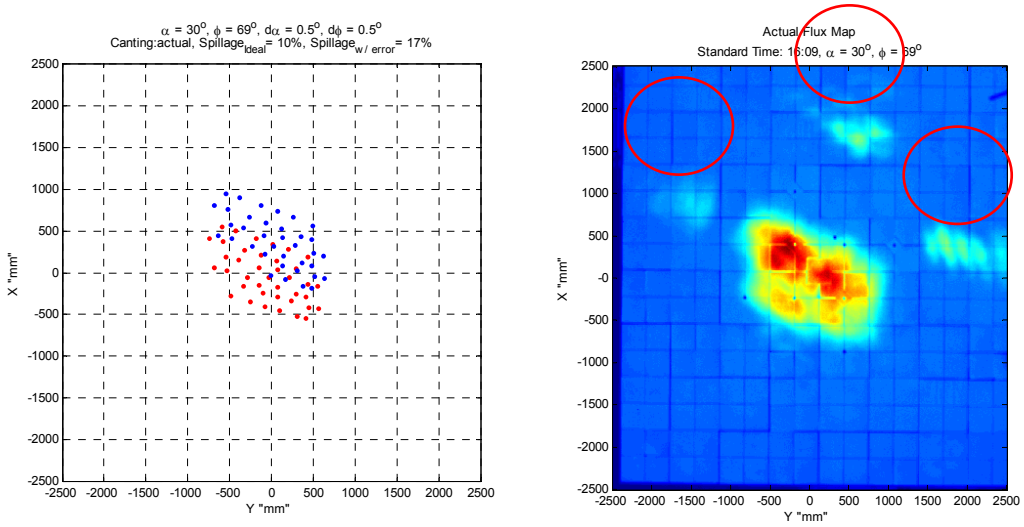

Figure 2-9 Left: facet centers on target plane deviated from ideal location at origin (0,0). Red points showing deviation assuming an ideal effective source. Blue points include both aberrations and an effective error in elevation and azimuth, of dα and dφ respect

Summary

The proposed model helps in better understanding the sources of aberrations in the flux maps obtained experimentally at different sun position during the day. This fast algorithm can be employed in assessing different heliostats designs to obtain an improved concentration quality. It was noticed that although ganged type heliostats might have better blocking and shading performance, they yield poorer concentration quality.

The model is also used to analyze the effect of different errors and sunshapes on the quality of concentration. The ability to introduce changing values of errors and sunshapes while still maintaining the calculation speed high, helps in simulating different scenarios and study the effect of varying sunshapes and design parameters such as canting angles, receiver size etc. without the need for long simulation times or complex ray tracing tools.

CHAPTER 3

HEAT FLUX MEASUREMENT SYSTEM

Flux distribution measurement is an essential step in characterizing the optical performance of solar concentrating systems; especially during the receiver and/or secondary concentrator design phase. A combination of optical (using CCD cameras) and thermal radiometry (using heat flux sensors) methods are often used for providing the required flux maps. While heat flux measurement is accurate and reliable, it is only feasible to be implemented at discrete points on the target. Optical methods on the other hand are less accurate but offer the convenience of easy implementation, at least ideally, and very high resolution. These two methods complement each other. One can, in principle, use heat flux measurement as a reference for calibrating the optical

system and hence combining the advantage of the two methods. Similar hybrid measurment systems have been used to measure heat flux on the target of parabolic dishes [24] and tower plants [25] [26].

Several heat flux sensors (HFS) are available for point flux measurement: slug type, thin foil, thin film and thermopile based transducers. Depending on the application the appropriate transducer is chosen [27]. Thermopile sensors are suitable for low range measurement > $10kW/m^2$, because of their high sensitivity, this is type of sensors is used to measure lower intensity flux around the center of the receiver (sensors 5 to 8 in Figure 3-1). For higher ranges Gardon type foil based sensors are used (sensors 1 to 4 Figure 3-1).

Although HFSs provide information about the flux intensity in 8 places around the target with good accuracy (given proper corrections and operation), they fail to give enough information on how the flux changes around these discrete measurement points. Thus a CCD camera is used to get information about the flux changes on the target with high resolution; 705 X 705 points of measurement. The CCD output, however, is reported in units of cd/m^2 and has to be converted into proper flux intensity units (kW/m^2). This conversion is affected by the temperature of the camera, quality of the target which has to be Lambertian, spectral changes in the solar radiation, changes in angles of incidence on the target in addition of to the accuracy of the HFS measurement which is used as a reference for this correlation. All of these issues are discussed in [28] [12]. In this chapter we will focus our attention on the proper operation and necessary corrections needed to achieve high measurement accuracy of radiation flux using the HFS. We start our discussion by presenting a sensor model for improved solar irradiation measurement at low fluxes which is necessary for low flux measurement conditions e.g. single heliostat test [29].

Next we present a generalized model that achieves lower accuracy at low fluxes but is extendible to higher fluxes under normal operation conditions.

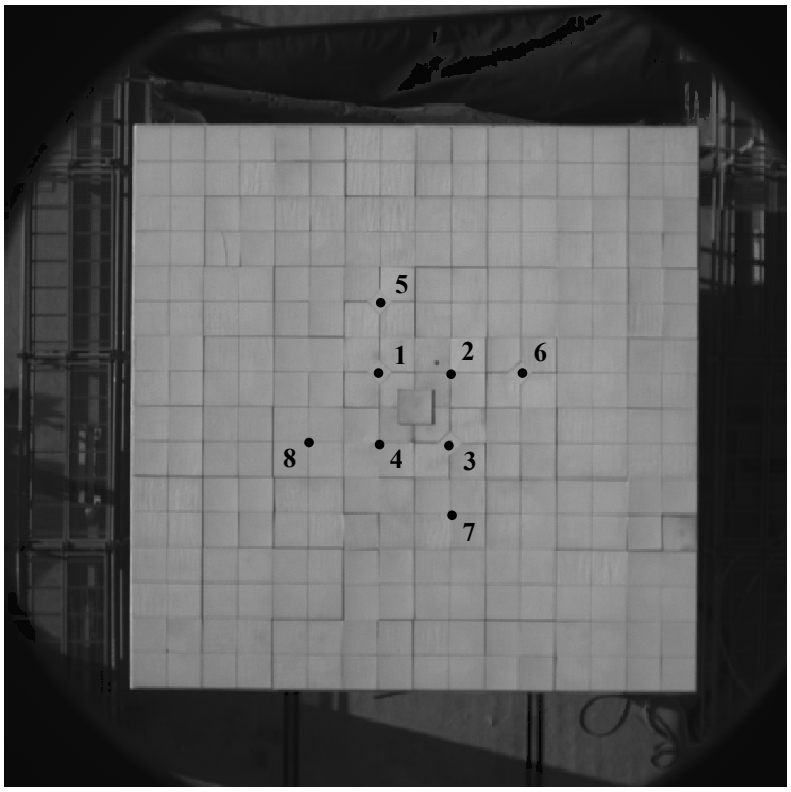

Figure 3-1 Target plane as seen by the CCD camera. Heat flux sensors locations are shown, 5-8 Schmidt-Boelter thermopile based sensors, 1-4 Gardon type foil based sensors.

3.1 A Model for Improved Solar Irradiation Measurement at Low Flux using Heat Flux Sensors

As was introduced in Chapter 1, a CCD camera affixed to the top of the tower is used to measure the concentrated flux distribution on a white Lambertian ceramic tile surface ~2.3 meters above ground level. Embedded within the tiles at eight locations are heat flux sensors (HFS) to measure the concentrated solar flux. HFSs are used to calibrate the images of the CCD camera to get an

absolute flux map. However previous studies using similar CCD-HFS systems have highlighted several inaccuracies in using these HFSs for solar radiation measurement [30-32],[26].

In recent years, the National Institute of Standards and Technology has developed a standard method for calibrating heat flux sensors [33] . A variable temperature blackbody (constructed from an electrically heated graphite tube) is used to maintain the radiation incident on the heat flux sensor. Similar calibration techniques have been used by the Vatell Corporation [34] which set the blackbody temperature at 1123 K, or at 2580 nm according to Wien's Displacement law. The spectral mismatch between these calibration methods and their use for solar radiation measurement has been noted to cause inaccuracies due to the varying spectral absorptive characteristics of the black surface (often Zynolyte) as a function of wavelength [30],[31],[26].Ballestin et al. [31] compared HFS calibrated at a blackbody temperature of 850C, between Air Masses (1-4) and with two different black coatings (Zynolyte and colloidal graphite) resulting in an average overestimation of 3.6% and 27.9% respectively. According to Ulmer et al. [26] spectral differences can cause an even larger error when using a windowed HFS.

The angular response of the HFS is also important to note. Previous measurements by Ulmer et al. [26] have shown that there is only an acceptable cosine response when the angle of incidence is less than 35 degrees. As the angle of incidence increases, the response decreases. The factory calibration of the devices assumes hemispherical radiation, which is not always the case for CSP applications. Error ranging from + 5.3% to +27% for non-windowed and windowed sensors, respectively [26].

Based on the findings of the aforementioned studies, non-windowed sensors with Zynolyte coating were chosen as most suitable for the present application. Since the sensors are intended for solar radiation measurements, calibrations were performed under ambient solar radiation to decrease any spectral mismatch errors.

Although non-windowed sensors have a better spectral and angular response compared to their windowed counterparts, they suffer from an inherent problem; increased error due to variations in ambient conditions, where convection and radiation from the surface of the HFS will affect its output. This is especially significant when the measured flux is low.

The difficulties in measurement and calibration of heat flux sensors lead NIST to develop calibration facilities for convective and radiative heat flux measurement, in order to become a standard for calibration to a desired uncertainty of ±2%.[35] [36]

As will be shown, the model we proposed for calibration reduces the measurement error significantly, especially at low radiation fluxes. Using the sensor without correction will result in underestimated output. An RMSE of more than 100 W/m^2 can be expected for uncorrected measurement of the HFS in measurements below 1.0 kW/m^2, however by using the proposed model and by keeping the transients in cooling water temperature to a minimum, significantly higher measurement accuracy can be achieved, and RMSE of less than $10W/m^2$ can be obtained. Moreover, since the model is based on easily measurable variables it can be applied conveniently to existing measurement systems.

3.1.1 *PRELIMINARY TESTING OF HEAT FLUX SENSORS*

Depending on the location of the HFS on the target, solar irradiation and number of heliostats in focus the measured flux can vary from less than 1(kW/m2) to more than 100(kW/m2). Hence the HFS's are required to measure in that range, with the greatest percentage uncertainties expected in the range <1.0 (kW/m2).

Figure 3-2 shows that the calibration coefficient is not adequate at low fluxes; an RMSE of more than 100 W/m^2 was calculated. To enhance the accuracy of measurement in this range a correction is needed to account for the factors that cause this error. It can also be noticed from Figure 3-2 that the error is highest at low flux, when the measured flux increases, the error in measurement decreases. (Note that we refer to the difference between the actual solar radiation and the measured solar radiation by the sensor as "the measurement error". It should be understood that this error results from the fact that the sensor is sensitive for all parts of the heat flux and not only incident radiation. Hence, it is not actually an error in the sensor measurement rather it is the sensitivity for variables other than the desired one)

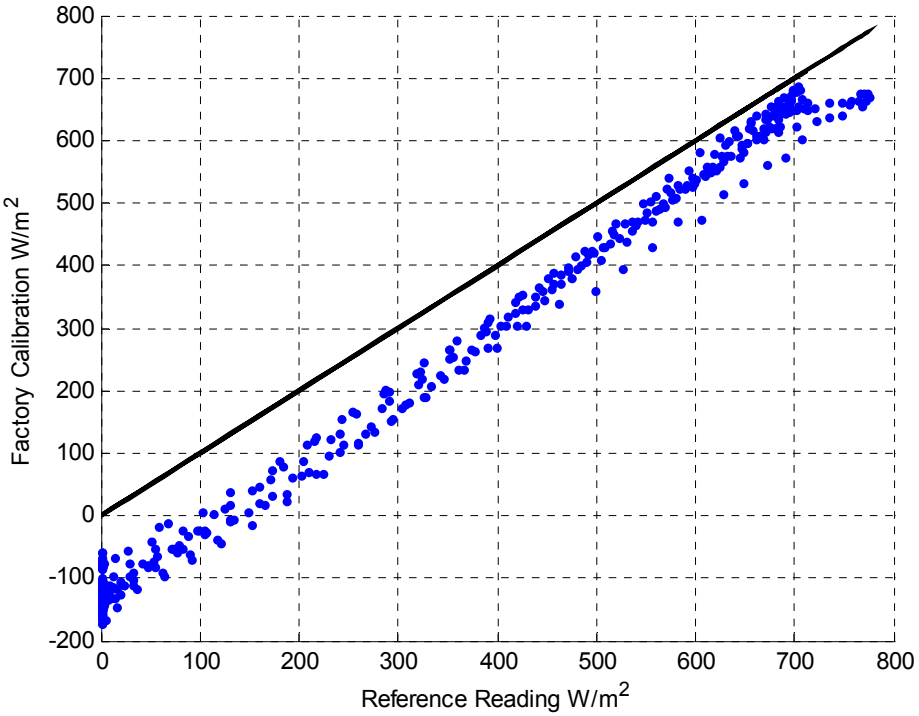

Figure 3-2 Radiation flux using factory calibration versus the radiation flux measured by the reference instrument (RMSE= 115 W/m^2).

In the 1980's Mulholland and Edgar, performed calibrations of similar sensors for solar applications, where they used polynomial fits for calibrating the sensors under realistic operation conditions [37]. In this chapter we present an in-situ method for calibrating non-windowed HFS for the use in BDSTC flux measurement system, in contrast with [37] however, the calibration model we are suggesting is based on a physical heat transfer model which employs easily measurable variables and which can therefore account for variations in ambient and operation conditions.

3.1.2 *Principle of Operation of Heat Flux Sensors*

A typical Schmidt-Boelter HFS is shown in Figure 3-3. The sensing element (SE) consists of a thin substrate (aluminum wafer in this case) across which a temperature gradient is established by the net heat flux.

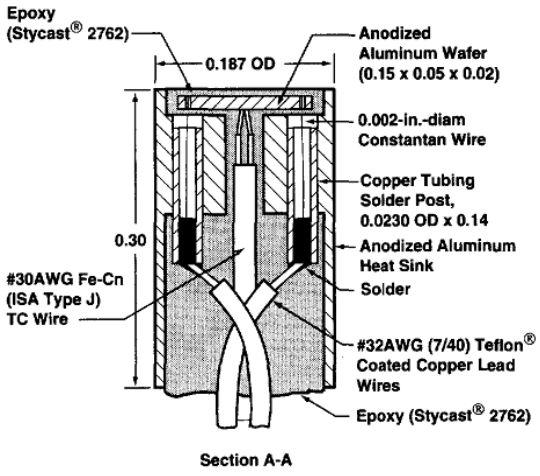

Figure 3-3 Inner construction of a typical HFS (but not of the exact model used) [38]

Assuming a unidirectional axial conduction for a very thin wafer, this heat flux is related to the temperature gradient just below the top surface by Fourier's law:

$$q_{net} = -k\frac{dT}{dx} \tag{3-1}$$

A thermopile wired between the top and bottom faces of the sensing wafer measures the developed temperature gradient and thus the steady state net heat transfer can be inferred using the finite difference form of Equation 3-1:

$$q_{net} \cong -k\frac{\Delta T}{\mathrm{L}} \tag{3-2}$$

where ΔT is the temperature difference, L is the thickness of the sensing wafer and k is the thermal conductivity of the wafer material.

The thermopile voltage output is given by the Seebeck relation, where n is the number of hot (or cold) junctions of the thermocouple circuit and δ is the Seebeck coefficient mV/K (more details on this can be found in [38]):

$$V = \delta\, n\, \Delta T \tag{3-3}$$

Hence from the above two equations 3-2 and 3-3 we can write that the sensitivity (S) of the HFS in mV/W (or other suitable units) as:

$$S = \frac{V}{q_{net}} = \delta\, n \frac{L}{k} \tag{3-4}$$

3.1.3 *HEAT TRANSFER MODEL*

A simple energy balance on the sensing element shows that this measurement will be affected by convection and radiation in addition to conduction in the radial direction.

$$q_{net} = q_{solar} - q_{convection} - q_{sky\ radiation} - q_{conduction\_radial} \tag{3-5}$$

Since the sensing wafer is very thin, the radial conduction term can be neglected. However, convective and sky radiation terms can be quite significant and have to be considered for accurate measurement. Thus equation 3-5 can be expanded to give:

$$\frac{k}{\delta n L} V = \alpha_{SE} G - h_{cn}(T_{SE} - T_a) - \tilde{h}_{cf} u_e (T_{SE} - T_a) - \sigma \epsilon_{SE} \left(T_{SE}^4 - T^4{}_{sky}\right) \tag{3-6}$$

where α_{SE} is the solar absorptivity of the sensing element, G is the incident solar radiation on the surface of the sensor W/m^2, h_{cn} is the natural convection heat transfer coefficient Wm^{-2}K^{-1}, $\tilde{h}_{cf}u_e$ is the forced convection heat transfer coefficient W m^{-2} K^{-1}, v is local wind speed m s^{-1}, σ is Stefan-Boltzmann constant Wm^{-2}K^{-4} and ϵ_{SE} is the emissivity of sensing element. The temperatures are T_{SE} for the sensing element, T_a for ambient temperature and T_{sky} for effective sky temperature. The calibration coefficient given by the manufacturer W/m^2 per mV includes the effect of the solar absorptivity along with the term $\left(\frac{k}{\delta nL}\right)$, hence:

$$G_{HFS} = G - \frac{h_{cn}}{\alpha_{SE}}(T_{SE} - T_a) - \frac{\tilde{h}_{cf}u_e}{\alpha_{SE}}(T_{SE} - T_a) - \frac{\sigma\epsilon_{SE}}{\alpha_{SE}}\left(T_{SE}^4 - T^4{}_{sky}\right) \quad 3\text{-}7$$

3.1.4 *EXPERIMENTAL SETUP*

The experimental setup in Figure 3-4 consists of a thermopile type (Schmidt-Boelter) HFS with an open and flat receiving surface. Cooling water is supplied to the sensor from a well insulated tank with enough thermal mass to eliminate the transients in water temperature. The flow rate through the sensor is high and constant to ensure that the sensor body temperature is as uniform as possible. Inlet and outlet temperatures are monitored using T-Type thermocouples inserted inside the tubes using a T-joint pointing upstream to enhance heat transfer. The high flow rate keeps the average difference between the inlet and outlet below about 0.3 K. Cooling water temperature has to stay above the dew point temperature at all times to prevent condensation on the sensor surface.

Figure 3-4 Right: BDSTC tower and heliostat field with experimental setup in front, left: details of the experimental setup

The sensors were tested under ambient sunlight and solar irradiation (GHI) was measured by a ventilated Eppley precision spectral pyranometer (PSP) (we use a reference sensor with the correct spectral response for calibration, rather than a reference source). In addition a LI-COR PV pyranometer is also used for comparison. A ventilated precision infrared radiometer (PIR) is used to measure sky radiation; compensation is done using the temperature measurement of both the dome and the case to infer the sky temperature. The equation is provided by the manufacturer (Eppley Labs) and is shown here after rearranging and including dome heating correction. A value of $\tilde{k}$ between (3.5 and 4) is recommended by [39] as cited in [40]

$$G_{IR} = -\sigma\epsilon\left(T_{case}^4 - T_{sky}^4\right) + \tilde{k}\sigma\left(T_{dome}^4 - T_{case}^4\right) \quad 3\text{-}8$$

An ultrasonic 2 axis wind sensor measures wind speed and direction, unlike typical 3-cup anemometer this sensor does not have a measurement dead zone at the beginning of its range (the 3-cup can only measure starting from 0.4 m/s). In addition it has better resolution. Ambient temperature is measured using a shielded T-type thermocouple. The sampling rate of the whole acquisition system is 0.1Hz.

3.1.5 *LINEAR REGRESSION MODEL*

Figure 3-5 shows an approximate electrical circuit analog used to model the HFS. The resistance between the mean water temperature T_w and the sensing element temperature T_{SE} is an effective resistance for many conductive paths that depend on the construction of the sensor.

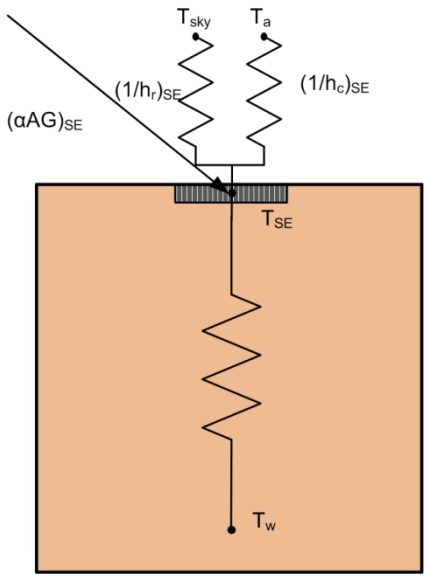

Figure 3-5 Electrical analog for the HFS heat transfer model

Figure 3-6 shows that the temperatures T_{SE} and T_w shown in Figure 3-5 vary almost in unison in the companion sensor (which is equipped with body and sensor thermocouples). And we note

that the variations in $T_{SE} - T_w$ (RMSE <0.5K) are much less than the variations in T_{SE}-T_a , based on this, in the proposed linear model of equation 3-9 we have replaced T_{SE} by T_w, this was done since T_w can always be measured whereas most sensors are not equipped with SE thermocouples.

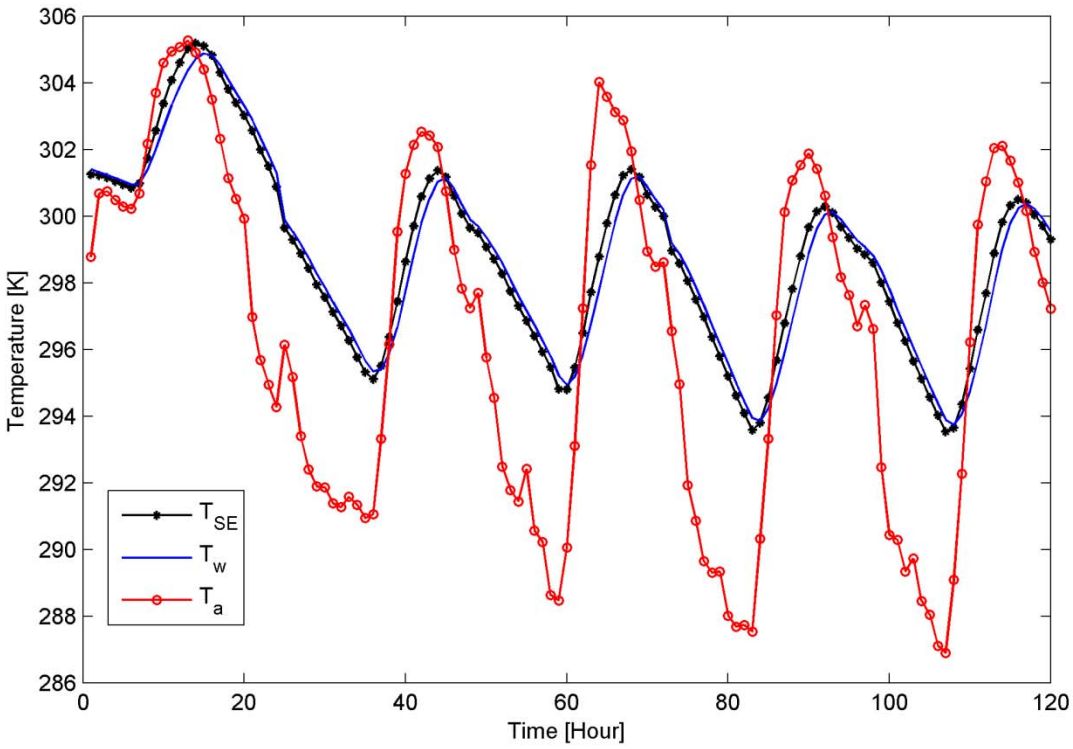

Figure 3-6 Variation of sensing element temperature T_{SE}, mean water temperature T_w and ambient temperature T_a.

Therefore we propose a regression model based on Equation 3-7; with T_w substituted for T_{SE} as follows:

$$G_{PSP} = c_0 G_{HFS} + c_1(T_w - T_a) + c_2 u_e(T_w - T_a) + c_3\left(T_w^4 - T^4{}_{sky}\right) \quad 3\text{-}9$$

The original data set used for regression consists of 16 days, with data sampled at 10-second intervals; the data set in use is reduced to only 10 days. The other 6 days were removed from the data set because they were cloudy/hazy days or due to measurement interruptions. The data set is further split into training and test data sets where every other day is taken for one set. Hence each set consists of 5 days.

Table 3-1 below shows the coefficients of the regression model of equation 3-9. As expected c_o is very close to unity (c_o= 1.070) which the physical model in equation 3-7 suggests. The increase from the ideal value of unity might be a result of degraded absorptivity of the SE coating (the sensor was in use and exposed to sand, dust, thermal transients and condensation for ~1 year) which the model compensates for by an increased value of c_o. In addition from equation 3-7 we expect that the last coefficient (c_3) be the product of the emissivity of the sensing element (ϵ_{SE}) and Stefan-Boltzmann constant (σ) divided by the absorptivity of the coating(α_{SE}), hence it should be close to Stefan-Boltzmann constant of (5.67 E-8 W. $m^{-2}.K^{-4}$), which is the case. These results indicate that the model adequately represents the physical operation principles of the HFS. Moreover, the t-statistics of the coefficients and the confidence intervals support this opinion.

Table 3-1 Coefficients and statistics of the regression model of equation 3-9, RMSE =6.31W/m^2,R^2=99.94%

Explanatory variable	Coefficient		Confidence	Interval	t-statistic
G_{HFS}	co=	1.070	1.069	1.070	1153.400
$(T_w - T_a)$	c1=	8.601	8.573	8.629	152.000
$u_e(T_w - T_a)$	c2=	3.138	3.113	3.162	63.161
$T_w^4 - T^4{}_{sky}$	c3=	5.666E-08	5.661E-08	5.672E-08	503.850

Figure 3-7 shows the radiation flux predicted using the proposed model applied to the output of the HFS versus the radiation flux measured by the reference instrument (PSP).

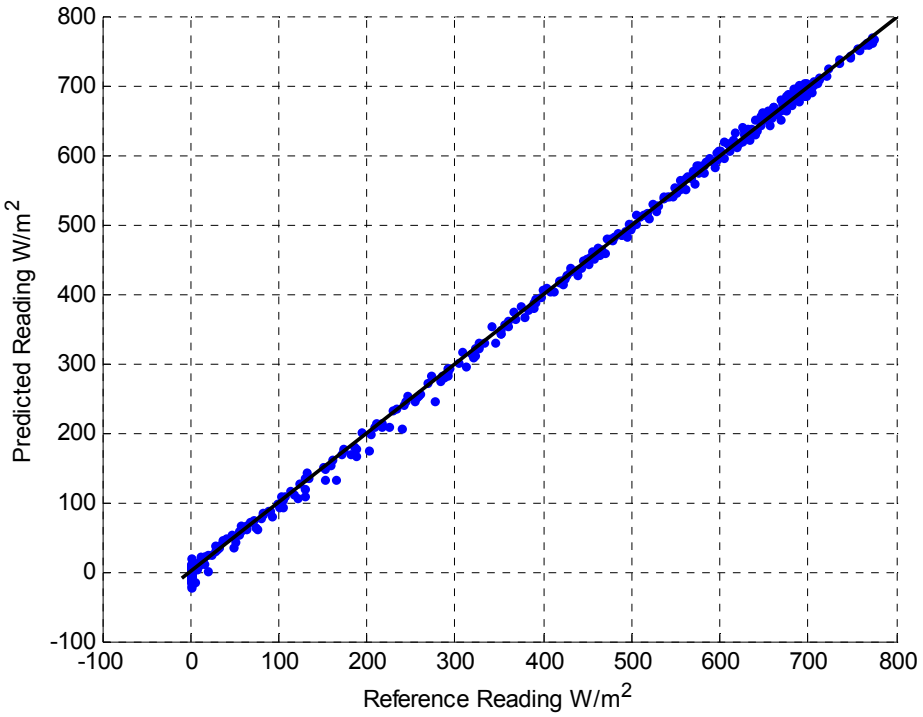

Figure 3-7 Radiation flux predicted using the proposed model of equation 3-9 versus the radiation flux measured by the reference instrument (RMSE=6.3 W/m^2).

We can see that the proposed model in equation 3-9 accurately represents the reading of the HFS with an RMSE of around 6.3 W/m^2 compared to RMSE of around 115 W/m^2 for the uncorrected reading.

3.1.6 *RESIDUALS ANALYSIS*

We noticed some records with very high error in both the raw and the corrected readings of the HFS. The data shown is an average of 60 records which indicates that these errors are not a result of measurement noise but that of a phenomenon which lasts more than 10 minutes (60 samples). After investigating the setup, it was noticed that a nearby post (one of the BDSTC tower posts) was partially shading the test rig in the early mornings. This phenomenon is shown in the Figure 3-8. Data points that experienced this phenomenon (two points, i.e. 20 minutes data) were removed from the training data set and regression was run again. In addition, there was another extreme point removed, but the reason behind the high error was not determined.

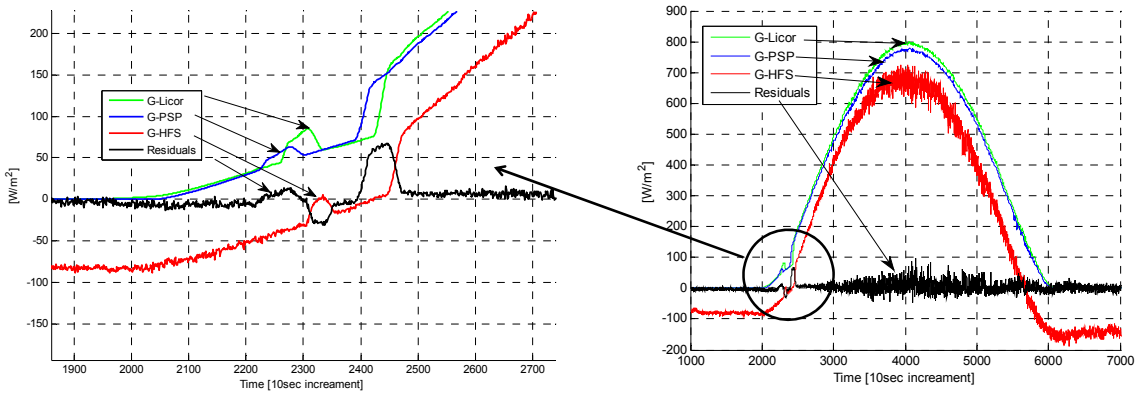

Figure 3-8 Error due to shadowing of the test rig in early morning. On the left a zoomed-in view where one can observe how shadow is progressing, first shading the PSP then the Licor and last the HFS.

Figure 3-9 depicts the residuals of the model against the four explanatory variables. It can be seen from the figures that the errors are for the most part randomly distributed. A minor linear

trend can be noticed when the residuals are plotted against the reference solar radiation, which might be a result of the non linearity of the HFS thermopile output and/or the conductivity of the SE material with temperature changes. However this trend can be neglected for the sake of a simplified model, a linear fit to the residuals gives a very small slope (3.816 E-4).

Four points draw attention in Figure 3-9. These points appear to be outliers and after investigation it was found that these points are successive and belong to the morning of one day, we have not determined the reason that caused this error though.

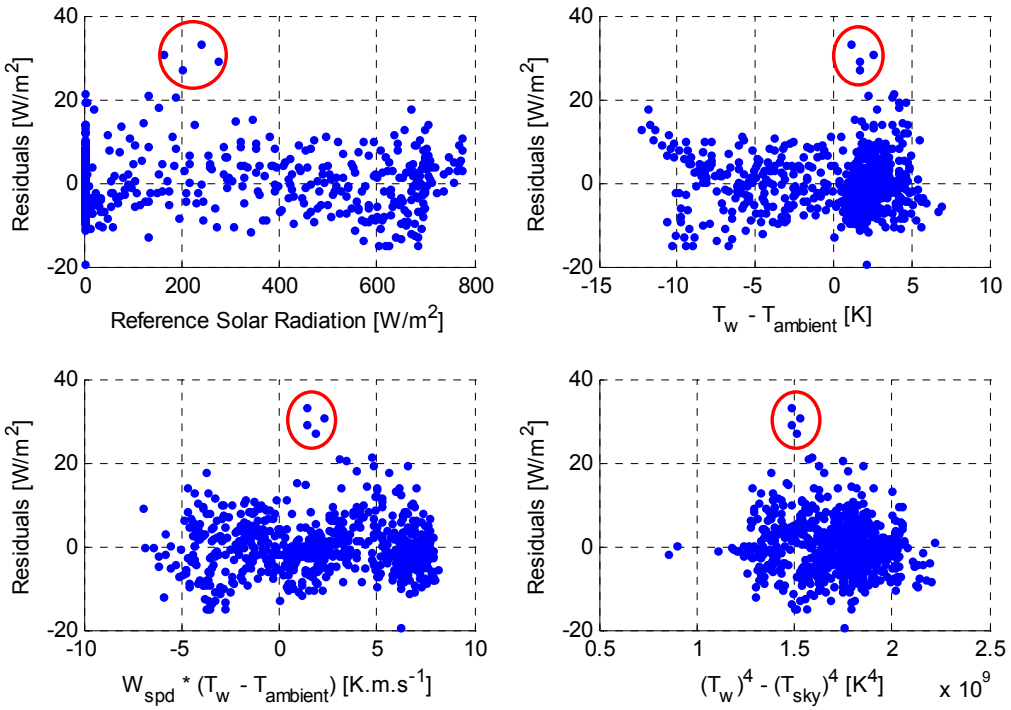

Figure 3-9 Residuals distribution versus explanatory variables

To further test the model we applied it on a test data set of measurements which were taken on different days with similar conditions. The residuals distributions for the test data set are shown

in Figure 3-10. The RMSE of the test data set was found to be around 6.6 W/m^2 which is close to the original RMSE of the training data set of around 6.3W/m^2.

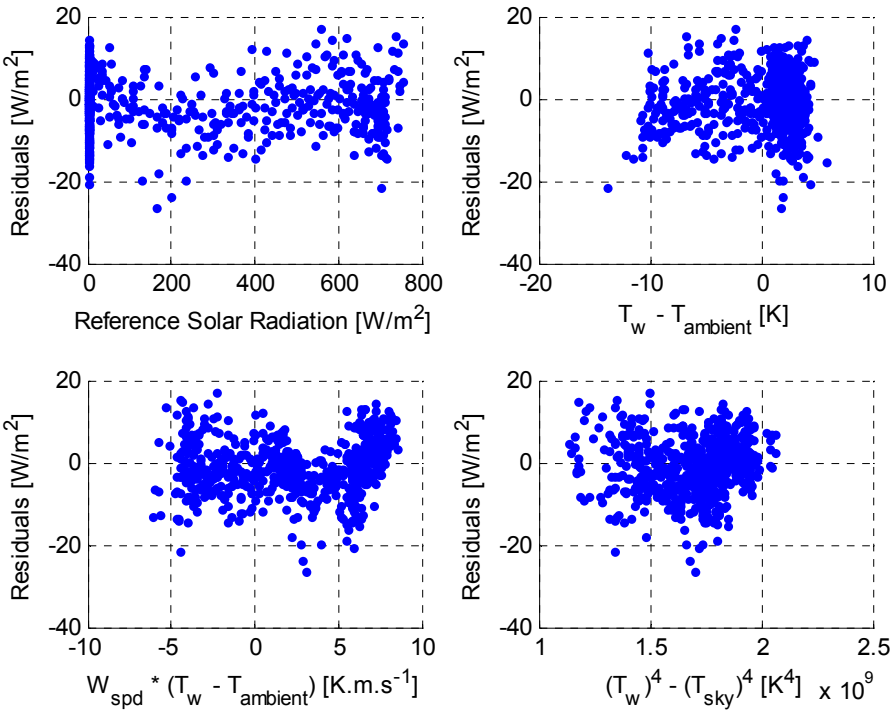

Figure 3-10 Residuals distribution versus explanatory variables for the test data set

3.2 In situ Calibration of Heat Flux Sensors

The model developed in 3.1 has been used to improve the measurement of heat flux sensors under low irradiation conditions. To obtain the model parameters a test was performed under one sun for one HFS with very stable cooling water temperature. A reference measurement device (Eppley PSP) and longwave radiation measurement device for estimating sky radiation (PIR). In addition wind speed was measured close to the sensor using a 2 axis ultrasonic wind sensor. Water temperature was measured close to the inlet and outlet of the sensor cooling channels

using thermocouples immersed counter-flow. These measures were aimed at achieving high accuracy in the measurement of the HFS.

Under normal testing conditions, however, it is more practical to perform the calibration while the sensors are attached in their positions on the target. Compared to the previous test, all the eight sensors are calibrated at the same time. The sensors are placed on a large flat plate compared to the small table used in the old test which can affect the convection conditions. Moreover, now the sensors have a different view factor of the sky, since part of the sky is blocked by the CR. Hence it was necessary to device this new in-situ calibration model for all the heat flux sensors.

The reference measurement is taken from a nearby pyranometer (PSP) and so is infrared sky radiation. The calibration is also done under one sun. In contrast with the previous model discussed in 3.1, instead of predicating the output of the PSP using HFS measurement and a loss model for each sensor, we will force the losses model to be the same for all eight sensors, this can be assumed since they all have the same geometry and all receive the same flux (under calibration conditions of one sun).

3.2.1 *EXPERIMENTAL SETUP*

Figure 3-11 depicts the setup of heat flux sensors used for measuring concentrated flux on the target plane. The sensors attached to the target from underneath. Coolant flows to the sensors from a well insulated tank with a sufficient thermal mass to prevent temperature fluctuations. During our tests we noticed that temperature fluctuations and transients profoundly affect the measurement of the HFS. The measurement of the HFS does not depend on the temperature of the coolant but rather on its stability. Hence we replaced the old cooling system that our

collaborators from Tokyo Institute have used. The old system employed a cooling loop which maintained the sensors temperature around 25^{o}C using a chiller with on/off control of the compressor. This meant that the cooling temperature will be changing continuously. Although the small tank in the chiller will reduce the fluctuations, a bigger well insulated thermal mass close to the sensors eliminates transience almost entirely and we phased out the chiller since the required cooling load of the sensors is small and can be handled by the thermal mass alone. (Typical increase in storage tank temperature in one day is ~11K. A typical temperature difference between inlet and outlet temperatures at solar noon is ~1.5K (average between all 8 sensors))

The coolant from the tank is distributed to the sensors using a manifold to ensure even flow to the sensors. Surface temperature measurement using thermocouples is used to measure outlet coolant temperature of the each sensor; insulation material is applied around the sensor where the measurement is performed to enhance accuracy. Coolant inlet temperature was measured in the supply tank.

Seven of the eight sensors needed re-painting to replace the absorptive coating that was degraded due to extensive use; this was an extra motivation to perform the calibration. The sensor thermopile output and all thermocouples are directed to the main data logger using an AM25T multiplexer located under the receiver. In addition ambient temperature and RH are recorded.

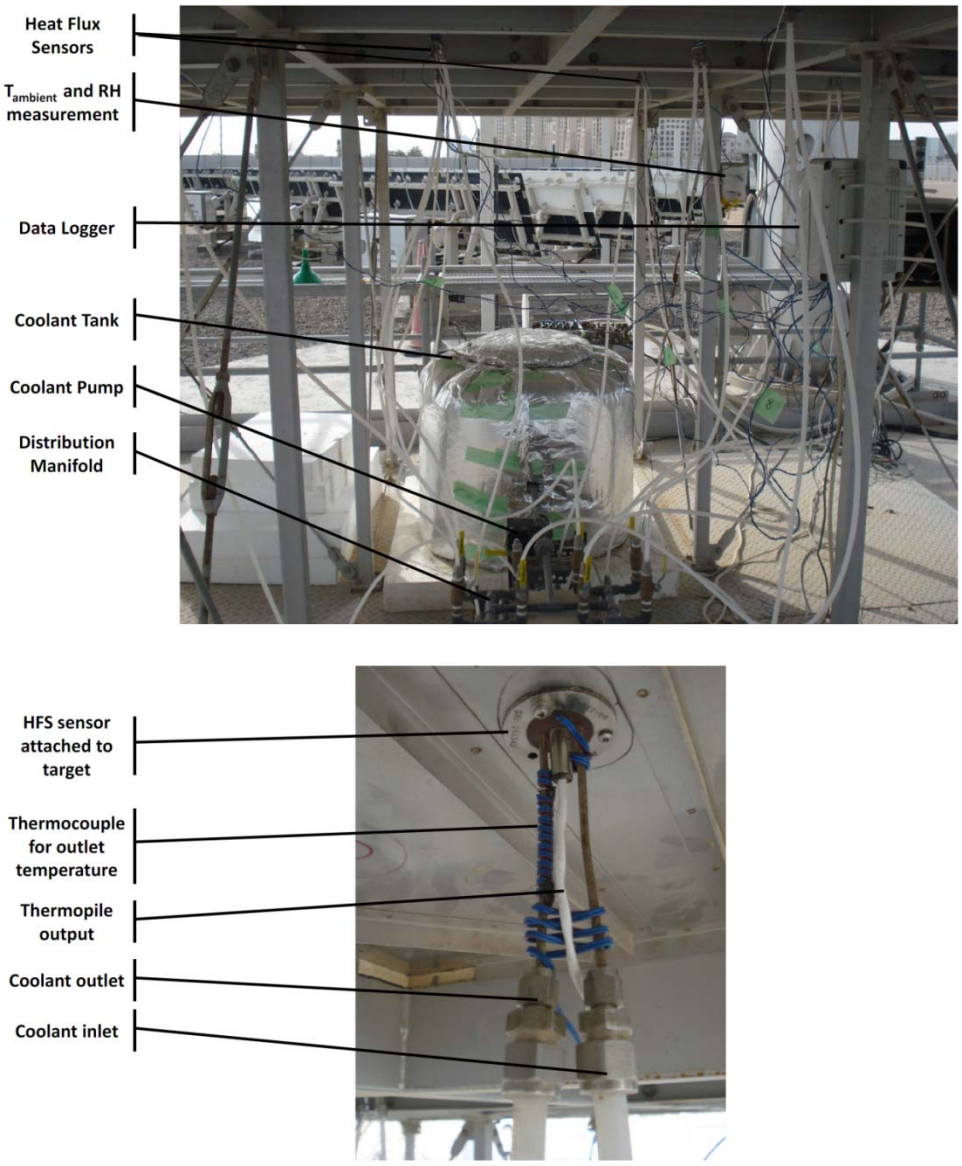

Figure 3-11 Experimental setup of heat flux measurement on the target plane using HFS. Up: A view of the sensors attached to the target from underneath. Coolant flows to the sensors from a well insulated tank with a sufficient thermal mass to prevent temperature fluctuations. The coolant is distributed to the sensors using a manifold to ensure even flow. Ambient temperature and RH under the target are recorded Bottom: thermocouples are used to measure coolant outlet temperature of each of the eight sensors in addition to coolant temperature in the tank, thermopile output of the sensor and all thermocouples are directed to the main data logger using an AM25T multiplexer.

3.2.2 *GENERALIZED CORRECTION MODEL*

The model is similar to the model suggested in equation 3-9, however we modify the convection loss term and force the losses to be the same for four sensors we are calibrating. We first use the measurements of four sensors only for identifying models of the sensors with the highest sensitivity measuring up to 10kW/m^2. Then we apply the same model for the other four sensors using their measured responses.

The convection model is based on the correlation of Nusselt number for a horizontal plate, we assume a laminar flow on the receiver surface since the Reynolds number (Re_L) on the receiver is for the most part lower than the transitional Reynolds number ($Re_{x,tr}$= 5.0E5) [41].

$$\overline{Nu_x} = \frac{\overline{h_x}L}{k} = 0.664\, Re_L^{\frac{1}{2}}\, Pr^{\frac{1}{3}} \qquad 3\text{-}10$$

Where $\overline{Nu_x}$ is the average Nusselt number on the receiver surface, $\overline{h_x}$is the average heat transfer coefficient W/m^{2}K, L is the length of the receiver, Pr is Prandtl number of air, Re_L is Reynolds number given by $Re_L = u_e L/v$. u_e is air wind speed m/s, v is the kinematic viscosity, k is the conductivity.

The convection heat transfer coefficient h_x is dependent on wind speed raised to the power ½. Hence the regression model can be formulated as follows

$$G = c_0 G_{HFS} + c_1 {u_e}^{\gamma}(T_w - T_a) + c_2\left(T_w^4 - {T^4}_{sky}\right) \qquad 3\text{-}11$$

Where v wind is speed and γ is the exponenet equal to ½ for laminar flow. We have tried several values for the exponent γ and the value of minimum RMSE for the model is indeed close to ½, hence it will be used in the model for physical significance.

In order to force the loss term coefficients (c_1 and c_2) to be the same for all the sensors, the data for all the sensors is combined in one regression problem as follows:

$$E = \begin{matrix} G_{HFS1} & 0 & 0 & 0 & u_e{}^{\gamma}(T_m - T_a) & (T_m^4 - T_{sky}^4) \\ \vdots & \vdots & \vdots & \vdots & \vdots & \vdots \\ 0 & G_{HFS2} & 0 & 0 & u_e{}^{\gamma}(T_m - T_a) & (T_m^4 - T_{sky}^4) \\ \vdots & \vdots & \vdots & \vdots & \vdots & \vdots \\ 0 & 0 & G_{HFS3} & 0 & u_e{}^{\gamma}(T_m - T_a) & (T_m^4 - T_{sky}^4) \\ \vdots & \vdots & \vdots & \vdots & \vdots & \vdots \\ 0 & 0 & 0 & G_{HFS4} & u_e{}^{\gamma}(T_m - T_a) & (T_m^4 - T_{sky}^4) \end{matrix} \quad \text{3-12}$$

$$C = \left[c_{0,1}\ c_{0,2}\ c_{0,3}\ c_{0,4}\ c_1\ c_2\right]^T$$

$$Y = [G_{PSP}^T\ G_{PSP}^T\ G_{PSP}^T\ G_{PSP}^T\ ]^T$$

$$C = (E^T E)^{-1} E\ Y$$

where $c_{0,1}\ c_{0,2}\ c_{0,3}\ c_{0,4}$ are the c_o coefficients of each of the four sensors. Using the data of several days of testing and after filtering hazy/cloudy days. The regression coefficients are shown in Table 3-2.

Table 3-2 Coefficients and statistics of the regression model of equation 3-12. RMSE=16.215 W/m^2, R^2=99.74%

Explanatory variable	Coefficient		Confidence	Interval	t-statistic
G_{HFS1}	$c_{o,1=}$	**1.028**	**1.034**	**1.029**	**376.3**
G_{HFS2}	$c_{o,2=}$	**1.035**	**1.040**	**1.035**	**376.9**
G_{HFS3}	$c_{o,3=}$	**1.026**	**1.031**	**1.026**	**377.9**
G_{HFS4}	$c_{o,4=}$	**1.036**	**1.041**	**1.036**	**376.9**
$u_e{}^{\gamma}(T_w - T_a)$	$c_{1=}$	**12.731**	**13.095**	**12.768**	**68.7**
$(T_w^4 - T^4{}_{sky})$	$c_{2=}$	**5.80E-08**	**5.89E-08**	**5.81E-08**	**133.0**

It can be seen from the regression coefficients (the c_o's) that the deviation from manufacturer calibration coefficient is not very high ranging between 2.6%-3.6% for the four sensors used in the regression, this deviation is likely to be caused by degraded absorptivity of the sensors. It is reasonable to assume that similar degradation affected the other higher range sensors (since they all experienced the same environmental conditions), therefore, we will take the mean value of c_o of the low range sensors and use it for the other high range sensors, and the coefficients of the loss term will be the same for all the sensors. Hence:

$$c_{o,5-8} = \bar{c_o} = \ 1.031 \qquad 3\text{-}13$$

Figure 3-12 depicts the residuals of the model against the three explanatory variables. Some structure can be noticed in the errors which can be attributed to non-linearity in the loss model in addition to errors in the measurement system. This structure in the residuals was not noticed in the model presented in 3.1; this might be due to the fact that greater care was practiced in obtaining the data for that model under well controlled measurement conditions. However moving to the operational setup we opted for ease of implementation by sacrificing a little in the accuracy of the measurements. Although structure is evident, the errors are mostly bound between +/- 20 W/m^2 with an RMSE of ~17.0 W/m^2.

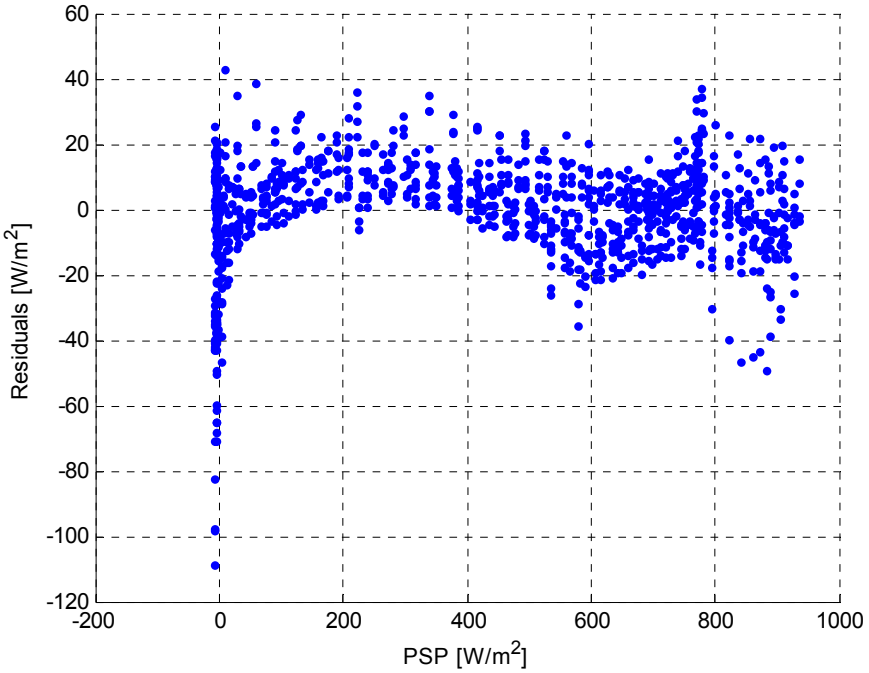
60
40
20
0
-20
-40
-60
-80
-100
-120
-200
0
200
400
600
800
1000
Residuals [W/m2]
PSP [W/m2]

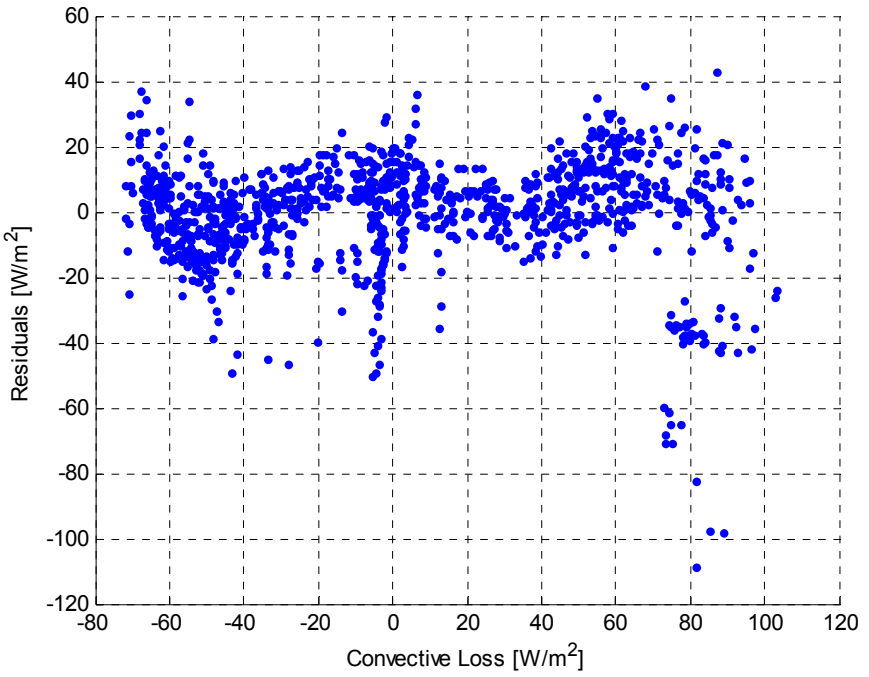
60
40
20
0
-20
-40
-60
-80
-100
-120
-80
-60
-40
-20
0
20
40
60
80
100
120
Residuals [W/m2]
Convective Loss [W/m2]

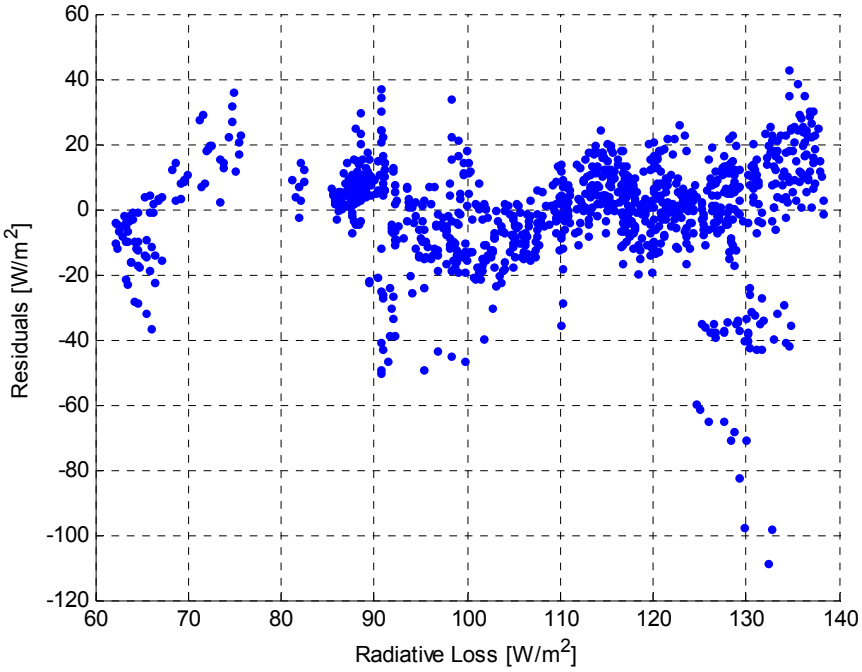

Figure 3-12 Residuals distribution versus explanatory variables

3.3 SUMMARY

The proposed model for heat flux sensors calibration reduces the measurement error significantly, especially at low radiation fluxes. Using the sensor without correction will result in underestimated output. An RMSE of more than 100 W/m^2 can be expected for uncorrected measurement of the HFS in measurements below 1.0 k W/m^2. However using the proposed model and by keeping the transients in cooling water temperature to a minimum, significantly higher measurement accuracy can be achieved, and RMSE of less than 20 W/m^2 can be obtained in measurements below 1.0 kW/m^2, hence enhancing the accuracy 5 folds (from 10% to 2%

assuming 1kW/m2 measurement). Moreover, since the model is based on easily measurable variables it can be applied conveniently on existing measurement systems without major modifications.

At higher fluxes experienced at normal operation conditions, the model was not verified because of the lack of a reference instrument. Since a convective and radiative heat loss model was used, it is expected that it will be applicable at higher flux levels, especially considering that the sensor temperature is kept within a reasonable range of roughly (+/-5^{o}C). The c_o term of the model compensates for deviation from the calibration coefficient of the manufacturer. This can be a result of sensor calibration at different spectrum or due to degradation of the absorptivity of the coating. On average this coefficient was around 1.031, which is a significant (3.1%) deviation at high fluxes since the correction is directly proportional to flux level, unlike the loss term which is only related to sensor temperature. In summary, we think that this model is adequate for correcting the heat flux sensors output, however although the model is trained under one sun, it is necessary to validate the model using a reference instrument at high fluxes.

CHAPTER 4

HELIOSTAT FIELD PERFORMANCE CHARACTERIZATION

A test for studying the performance of individual heliostats was performed; this test helps us to better understand the unique aspects as well as the problems associated with the unusual heliostats used in this pilot plant (ganged-type heliostats, see Figure 1-5) in addition to the plant's unique optical design. The data was also helpful in pinning out an important characteristic of the concentration quality of these heliostats which we diagnosed as a form of off-axis aberration through the model presented in Chapter 2. In this chapter we will present the method used in assessing the performance of each heliostat and then apply it to the test data obtained for the entire heliostat field.

4.1 CONCENTRATION QUALITY

There are two important features of a flux distribution map which are of interest, one is the total energy sum and the other is the distribution of the flux on the receiving plane, the latter includes two more parameters of interest, centering and concentration quality.

By centering we mean the deviation of the centroid of a certain flux map from the geometrical center of the target (see Figure 4-1), this is mainly a result of errors in aligning the secondary reflector mirrors or/and the tracking photo-sensor of the heliostats. Centering is a problem that could be easily resolved relative to other problems, thus we will isolate it by basing all our analysis of the flux maps on their centroid rather than the geometrical center of the target. The offset between the geometrical center and the centroid of the flux map will be used as a measure of centering error.

To facilitate the comparison of flux distribution maps of all the heliostats in a field, it is advantageous to combine the other two important merits into one quantity (total energy and concentration). Problem heliostats can then be identified for further visual and statistical inspection of individual flux density maps or for other more detailed studies.

Figure 4-1 illustrates a typical flux density map of (980x980) pixels; the area of interest to us is a square within the 980 x 980 pixel region of approximately 705 x 705 pixels which corresponds to the 4.876m x 4.876m target. Thus a pixel covers 6.9163 x 6.9163 mm. The design focal point of the beam down configuration is the center of the square traget.

4.2 WEIGHTED FLUX MAP

For the upcoming analysis we will assume a receiver with two concentric circular apertures as shown in Figure 4-1. The inner region is where most of the energy and the highest concentration are expected; physically this can be the aperture of the main high temperature receiver, the radius of this aperture is r_1. Some of the concentrated radiation will reach the region between the two circles ($r_1<r<r_2$), generally this radiation will have less concentration and less energy than the inner region, thus it can be used for pre-heating the HTF before entering the inner receiver. According to the previous argument, for each point in the matrix a weighted value can be calculated by the following formula:

$$Q(x,y) = \begin{cases} 1\,, r \le r_1 \\ G * \left(\frac{r_2 - r}{r_2 - r_1}\right)\,, r_1 < r < r_2 \\ 0\,, r \ge r_2 \end{cases} \qquad 4\text{-}1$$

In equation 4-1) , G, the flux intensity, is multiplied by 1 in the inner region, while in the outer region the flux points are multiplied by zero (to reflect its usefulness) and the flux is linearly weighted in the region in between the two apertures. Overall the weighting function will be trapezoidal, see Figure 4-1.

The flux map produced by the CCD camera contains luminance (cd/m^2) values; these values are assumed to be a measure of flux intensity G. To convert luminance values into heat flux units, a constant conversion factor is assumed (for a non-Lambertian target this factor might be varying [12]). G is then normalized by the DNI at the time of the measurement. DNI records are

available from the weather station every ten minutes thus interpolation was required to get DNI values at the step times of the test.

Before we can use equation 4-1), the centroid of the flux map should be calculated, and the receiver dimensions (r_1 and r_2) should be selected.

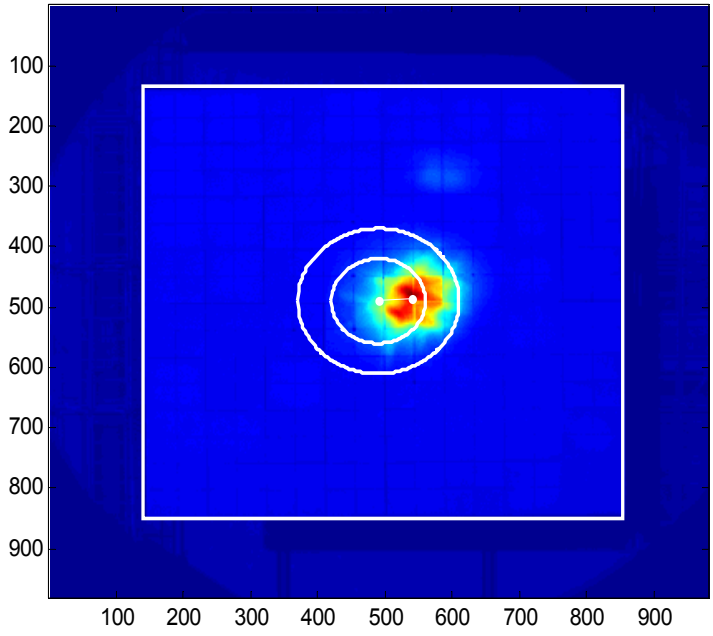

Figure 4-1 Typical flux density map generated by the overhead CCD camera (Resolution: 980x980 pixels).

4.3 Centroid and Offset Calculation

The first step in analyzing the flux map is to find the flux map centroid. This could be easily done by finding the x and y coordinates of the centroid Cx, Cy respectively:

$$C_x = \frac{\sum G(x,y) * x}{\sum G(x,y)} \quad and \quad C_y = \frac{\sum G(x,y) * y}{\sum G(x,y)} \qquad 4\text{-}2$$

Applying this equation on the raw flux map will result in unwanted results as the calculation will be affected by the ambient radiation falling on the receiver (since we are dealing with low concentration of only one heliostat at a time) thus some filtering of the flux map is necessary in order to calculate the centroid coordinates.

The points of the flux map which should be filtered are those of ambient radiation on the plane of the receiver. These will generally correspond to the lowest points in the flux map unless there is a shadow on the receiver cast by the central reflector or one of its three pillars. Thus the filtered flux map is given by equation 4-3) below, where $g_{ambinet}$ is the ambient radiation, k is the filter parameter, G(x,y) is the original flux map, G'(x,y) is the filtered flux map :

$$G'(x,y) = \begin{cases} G(x,y) - k * g_{ambient}, & G(x,y) - k * g_{ambient} > 0 \\ 0 \quad , & G(x,y) - k * g_{ambient} \leq 0 \end{cases} \qquad 4\text{-}3$$

4.3.1 *FINDING $G_{AMBIENT}$*

$g_{ambient}$ is found using the Matlab function (mode) which gives the most frequent value (MFV) in the flux map. MFV will most probably correspond to a point outside the region of heliostat radiation, and thus will correspond to ambient radiation (eg. See Figure 4-1).

Shadows make the detection of the value of $g_{ambient}$ a bit more complicated, since the lowest value of the flux map doesn't correspond to ambient radiation anymore, thus instead of finding MFV of the whole flux map, we find it for each of the four corners of the flux map; these areas

don't normally have any radiation from the heliostat, and at most 3 corners could be shaded at a time, thus $g_{ambient}$ will most probably correspond to the maximum of the 4 MFVs that we found for each corner. We also increase the odds of finding $g_{ambient}$ by rounding the matrix values to the nearest integer and thus increasing the number of pixels having similar values.

4.3.2 *FILTERING FOR CENTROID CALCULATION*

To calculate the centroid correctly we need to get rid of ambient radiation points from the flux map using equation (4-4), ideally we should only remove ambient radiation points thus setting k to 1 in equation (4-5). However some scattered radiation coming from the heliostat may also affect the calculation, for which we use a value slightly greater than 1, k=1.2 was found to give good centroid detection.

4.3.3 *FILTERING FOR CALCULATING CUMULATIVE POWER CURVE*

In order to calculate the curve in Figure 4-3, we should make sure the energy in the flux map is only from the heliostat and does not include any ambient radiation (GHI). Thus we use a value of k=1 for this purpose.

After calculating the centroid, the offset (distance between the geometrical center and the flux map centroid) can be easily calculated to measure the error in the flux centroid position resulting from misalignment in the heliostats, in the tracking sensor, or in the corresponding secondary reflector mirror.

4.4 SELECTING HYPOTHETICAL RECEIVER DIMENSIONS

In order to dimension the hypothetical receiver that we are going to use in the analysis we selected four of the best flux maps and we based the receiver dimensions on these four maps. In Figure 4-2 the mean radiation at a given radial distance from the flux map centroid is plotted as a ratio of the theoretical maximum or upper limit for possible radiation. This limit is based on the concentration factor of the heliostat. The heliostats used in the beam down have flat facets which are canted to one imaginary focus point at the focal point of the secondary reflector. Thus the upper limit for the power indicated by one of the pixels in the flux map will be (DNI*NumberofHeliostatFacets*PixelArea). From the figure it can be seen that the power drops to lower than 3% of the theoretical maximum for radial distance greater than 100 pixels or 0.571m, moreover, it can also be seen that none of the flux maps exceeds 25% of the theoretical maximum.

Figure 4-3 depict the flux map in cumulative form; total power included in the circular region of radius (r) around the centroid is normalized by the maximum power that can be reflected to the receiver, (DNI*Heliostat Area).

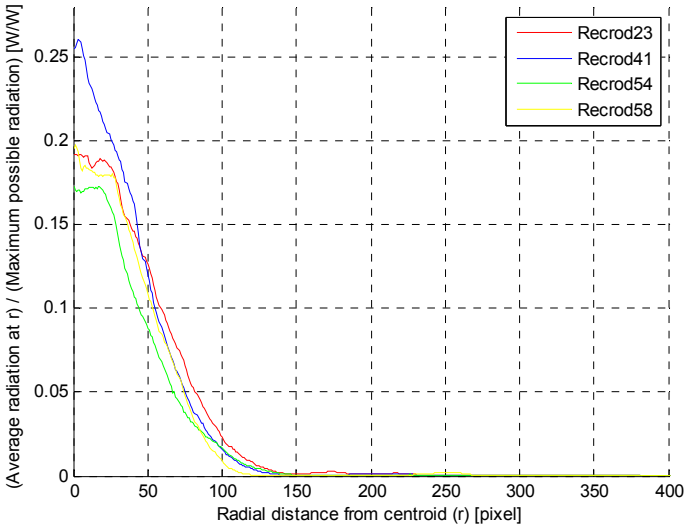

Figure 4-2 Mean radiation at a radial distance (r) from the centroid of the flux map, normalized by the theoretical maximum power given by (DNI*number of flat heliostat facets*area of one pixel), this theoretical maximum is the upper limit of radiation concentration as it clearly ignores cosine factor, incidence angle, reflectivity of the mirrors in addition to other things.

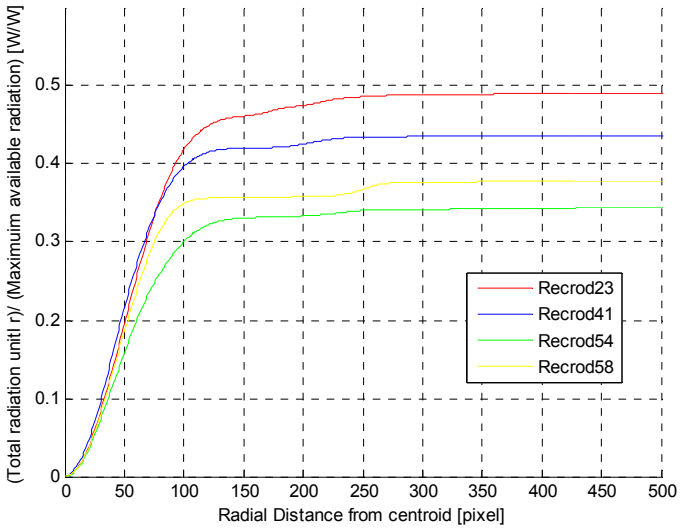

Figure 4-3 Cumulative power intercepted by the receiver from the centroid until the radial distance (r), normalized by the maximum theoretical total power (DNI * Heliostat Area). This theoretical maximum is the upper limit of radiation concentration as it clearly ignores cosine factor, incidence angle, and reflectivity of the mirrors in addition to other things.

Figure 4-3 has a significant value in comparing heliostat performance. Not only is it a measure of the amount of energy that the heliostat is reflecting to the receiver compared to what is available, but it also indicates how well the heliostat is concentrating the reflected energy. For example if we take a look at Record23, it is clear that it is the best heliostat that approaches the theoretical limit. Moreover it achieves a more than 42% within a radial distance of 100 pixels, compared to Record 41 which achieves the same ratio at 112 pixels.

We can notice some crossing-over between the curves (e.g. Records 54&58 and 23&42) and this means that the quality of each flux map depends on the chosen radii of the receiver. Choosing a receiver radius under 50 pixels will favor Record41 over 23, however if the receiver radius was above 75 Record 23 will be favored. In practice optimal r1 and r2 involve many system design parameters pertaining to power cycle temperature, receiver losses and their cost parameters. However by studying Figure 4-2 and Figure 4-3, we can choose reasonable values for example r1=70 and r2=120. This way we can make use of the highly concentrated radiation in the inner receiver and still make of use a considerable amount of the energy by having the second receiver (e.g. CPC) at r2.

Figure 4-4 is similar to Figure 4-3 but with the x axis scaled to better show the region of interest. The curves are normalized by the actual total power instead by the theoretical total power. Actual power is the total power reflected from the heliostat to the target (thus, ambient radiation is excluded), this is calculated using equation (4-6) setting k to 1 and then integrating the flux map over the target area.

We can see from the figure that by choosing a radius r_1=70, for all the shown records more than 60% of the total power will be intercepted in the inner receiver, and that more than 90% of the

power will be intercepted by the whole receiver. Figure 4-5 depicts the corresponding flux maps with the receiver apertures.

We assume that the designers have aimed for a certain flux distribution (concentration and optical efficiency) knowing that there is some uncertainty in achieving the said target. Now faced with the real flux distribution one can design a receiver optimized for a given (range of) operating temperature. Since receiver design is not the subject of this chapter, we aim only to intercept some reasonable fraction of the reflected power incident on the whole target.

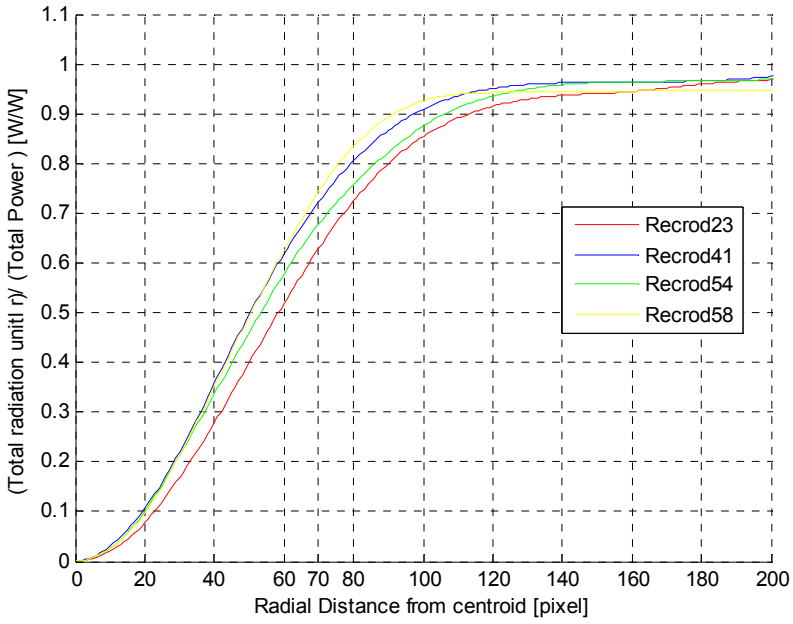

Figure 4-4 Cumulative power intercepted by the receiver from the centroid until the radial distance (r), normalized by the total power.

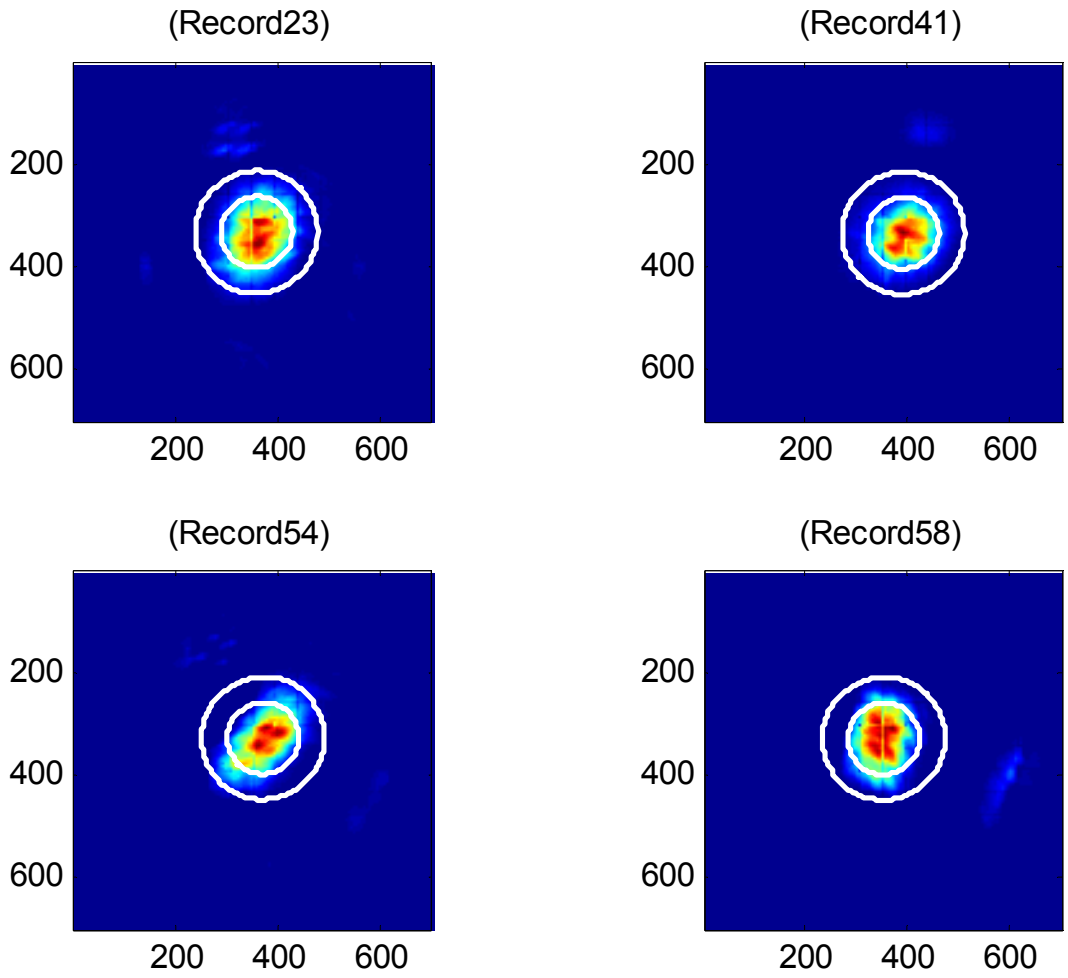

Figure 4-5 Flux maps with receiver apertures drawn around the centroid, flux maps where filtered using equation 3 and a k value of 1.

4.5 RESULTS

One of the aims of this test is to assess the performance of the individual heliostats in each of the three fields (sectors), and to compare it to the performance of other heliostats. One sector was tested each day for five time steps which are chosen throughout the day (the middle time step being at solar noon). At each time step all heliostats of that sector were tested.

Data were collected for 6 days (twice for each field) in March 2010. March represents one of the best months of the year in terms of DNI because summer haze and dust are frequent in Abu Dhabi. Unfortunately we had to discard the data of one of the test days of the east field because the heliostat sequence was accidently scrambled.

Three performance parameters are chosen to interpret the data collected; we include here a summary of the results for space constraints. First is the amount of power intercepted by the receiver aperture (weighted using equation 4-1)) normalized by the DNI * Heliostat Area at time of measurement. This parameter is a measure of the overall optical performance of the heliostat and how well it concentrates the radiation inside the aperture. Since the calculation is based around the centroid of the flux map and not on the center of the receiver, this parameter does not include centering.

Table 4-1 Intercepted power normalized by incident DNI * Heliostat Area. The number next to the field-name represents test day in March (e.g. 18 -> March 18th)

	North18	North20	East22	West27	West29
Average	24.0%	25.1%	21.8%	15.8%	25.1%
Standard Deviation	10.2%	9.5%	9.1%	7.1%	9.3%
Minimum	0.5%	1.2%	7.5%	2.4%	4.4%
Maximum	43.2%	40.9%	64.4%	30.4%	44.8%

Table 4-1 summarizes the statistics of this parameter for the data set. It can be seen that the average values range from around 15.8% up to 25.1%. Generally the maximum percentage of intercepted DNI lies around 45% for most of the cases, but for some heliostats it can reach values as high as 64.4% as in East22.

A better representation of concentration quality of a certain heliostat can be obtained by the ratio of the intercepted power and the total power reflected on the target (the latter given by equation (**Error! Reference source not found.**)), or as is commonly referred to as the intercept factor. Table 2 summarizes the results of the intercept factors of our hypothetical receiver. Generally the receiver intercept factors are high, by design, average values are around 75% while maximum values can reach more than 97%.

Table 4-2 Intercept Factor.
The number next to the field-name represents test day in March (e.g. 18 -> March 18th)

	North18	North20	East22	West27	West29
Average	76.4%	76.0%	72.1%	74.4%	73.5%
Standard Deviation	11.2%	11.2%	10.7%	13.7%	13.8%
Minimum	48.3%	47.0%	40.1%	28.0%	37.0%
Maximum	97.0%	97.2%	95.3%	95.3%	95.0%

Centering is measured by the offset, which is the distance between the calculated flux map centroid and the geometrical center of the receiver. Deviation from the ideal value of zero is most probably due to misalignment in the tracking sensor or in the secondary reflector mirror corresponding to the heliostat in question. Compared to other errors, offset can be easily fixed, that is why the values for offset are reported separately in Table 4-3.Values around 40 pixeles (~277 mm) are typical as can be seen from the table. Maximum values are quite far however, but this might be a bit misleading as error in calculating the centroid will dramatically affect the offset calculation; this is probable when the power levels are low or when aberrations are high.

Table 4-3 Flux map offset.
The number next to the field-name represents test day in March (e.g. 18 -> March 18th)

Field-Day	North18	North20	East22	West27	West29
Average	40.0	37.6	39.9	44.3	44.1
Standard Deviation	22.9	18.7	22.9	19.4	16.0
Minimum	1.8	3.0	1.8	5.0	8.8
Maximum	139.0	108.3	138.8	127.0	103.4

One of the important aspects of this test is the ability to spot irregularities in the heliostat field and/or to get better understanding of the heliostat field and some complex aspects of blocking and shading especially for such an unusual optical design of both the tower and the heliostats.

4.5.1 *TOWER SHADING*

As it is hard to inspect each and every flux map in detail, the previously discussed parameters can lead us to the discovery of some issues which are hard to detect manually, when suspicious values are detected. For example heliostats A3 and A4 (North sector) at noon time-step had very low ratios of intercepted power to incident DNI, looking at the corresponding flux maps in Figure 4-6 .We can see that there is only ambient flux on the receiver in addition to the shadow casted by one of the three pillars of the central reflector. The two heliostats were completely shadowed by the central reflector for the entire noon period. This problem could have been avoided by moving the heliostats in the North sector farther from the tower. The sun elevation angle at the time of the test was around 60^{o}.

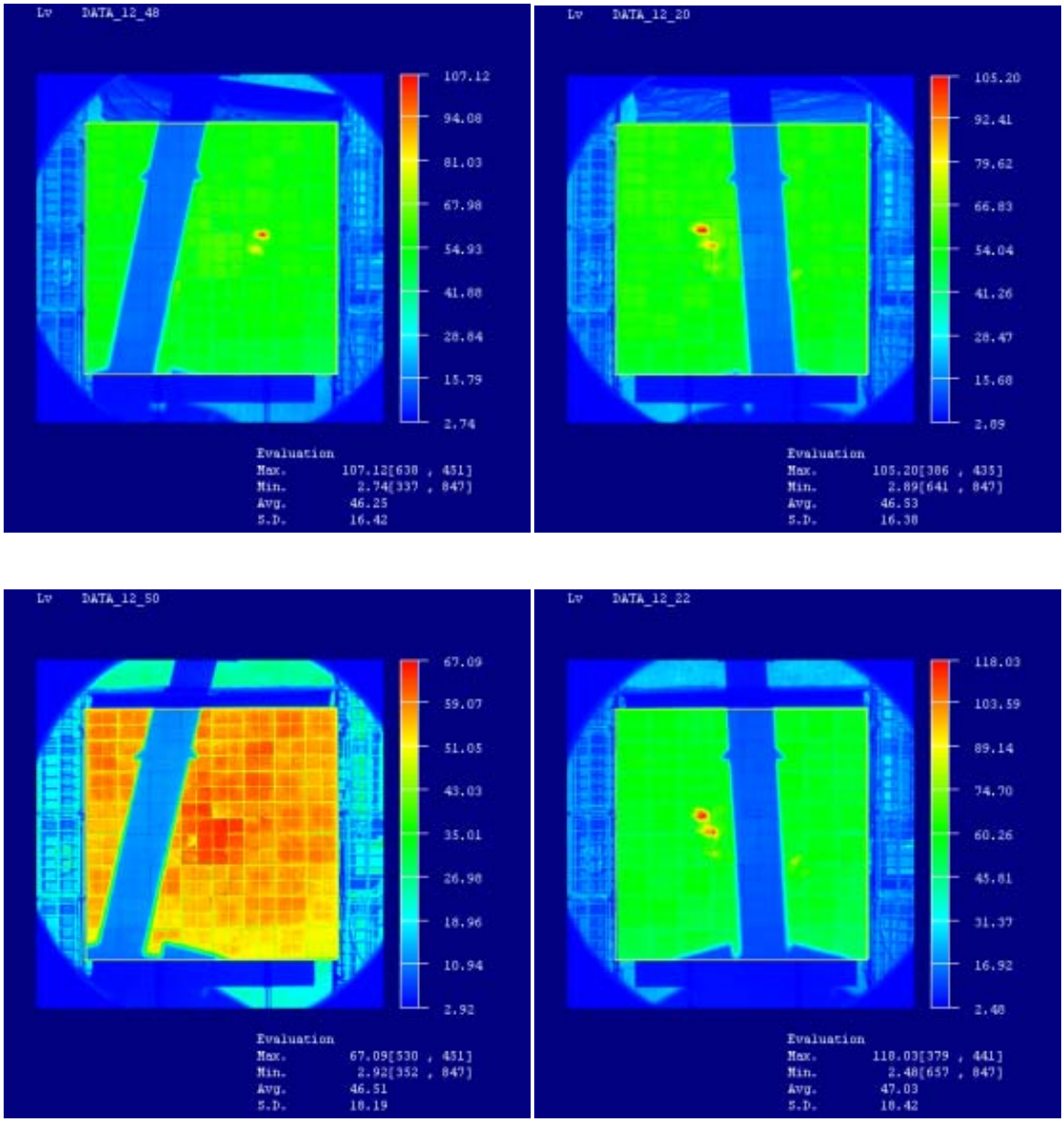

Figure 4-6 Complete shading of "A-line" heliostats in the North sector around solar noon, sun elevation angle ~60^{o}.

4.5.2 *HELIOSTAT CONCENTRATION ERRORS*

There are some undesirable patterns which were spotted by looking at the flux maps and the performance parameters. These patterns seemed to happen at high azimuth angles. As we came

to know through the model presented in Chapter 2, this is a result of off-axis aberrations, mainly astigmatism. Canting errors of the heliostat mirrors and deformed central reflector mirrors can also affect the performance of the heliostats, it is worth mentioning that was noticed some deformed CR mirrors which subsequently have been corrected by the manufacturer. The flux maps below show some examples of undesirable heliostat concentration.

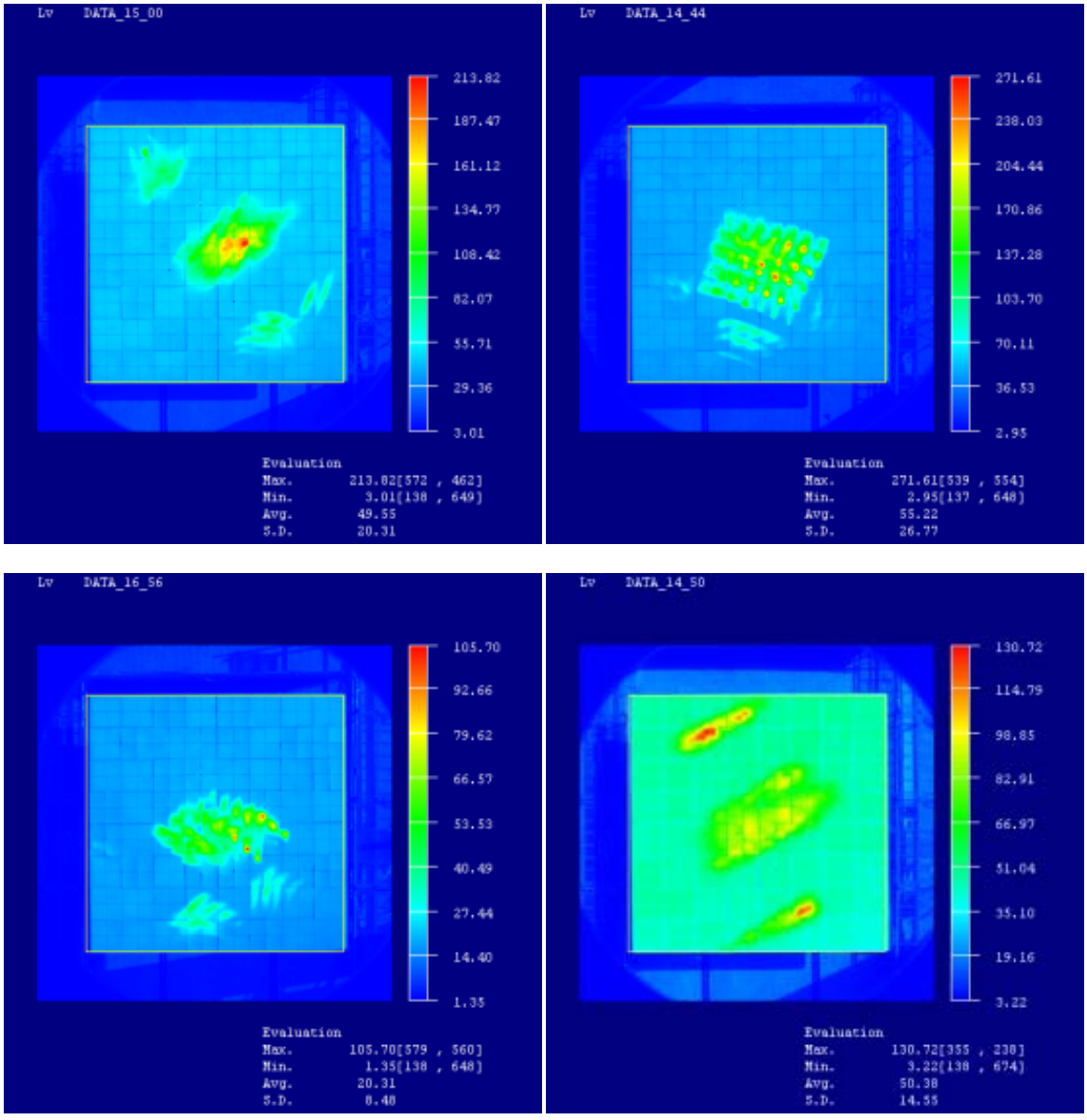

Figure 4-7 Heliostat concentration errors showing scattering and aberrations

4.6 SUMMARY

In this chapter the test used for assessing the performance of individual heliostats in the plant was discussed and results were presented. The methodology is helpful in identifying any current/future problems in the heliostat field easily, whether they results form design problems or flexible implementation issues like canting or optical alignment problems. It also allows studying the unique aspects of the non-conventional heliostat design.

CHAPTER 5

ANALYSIS OF BEAM-DOWN PERFORMANCE UNDER FULL CONCENTRATION

In this Chapter an analysis of the Beam-Down performance under full concentration is done, it is based on a hypothetical receiver design to assess the performance under varying operating temperatures. The heat transfer fluid (HTF) assumed in the design is liquid Sodium which has high specific heat and can reach very high temperatures. Such HTF was used in central receiver plants in the 1970s [8].

5.1 RECEIVER NET USEFUL POWER

Under steady state conditions the net useful power output of the receiver is the difference between the absorbed solar radiation and the thermal loss from the receiver surface. [10]

$$\dot{Q}_u = A\left(\alpha\dot{Q}_{incident} - U_L\left(T_{pm} - T_e\right)\right) \quad 5\text{-}1$$

Where ($\dot{Q}_u$) is the useful power output of the receiver, α is the absorptivity of the receiver in the solar spectrum, $\dot{Q}_{incident}$ is the incident solar power on the receiver aperture, U_L is the overall heat loss coefficient, T_{PM} is the Mean Plate Temperature (MPT) and T_e is the air temperature.

The MPT is difficult to measure or calculate since it is a function of the receiver design, incident solar radiation and the entering fluid conditions [10]. Equation 5-1 can be reformulated to become in terms of the inlet fluid temperature (T_{fi}) and a parameter called the heat removal factor (F_R): [10].

$$\dot{Q}_u = A\,F_R\left(\alpha\dot{Q}_{incident} - U_L\left(T_{fi} - T_e\right)\right) \quad 5\text{-}2$$

The heat removal factor (F_R) is given by:

$$F_R = \frac{\dot{m}C_p}{AU_L}\left(1 - \exp\left(-\frac{AU_LF'}{\dot{m}C_p}\right)\right) \quad 5\text{-}3$$

Where $\dot{m}$ is the mass flow rate, C_p is the specific heat of HTF and F' is a parameter that accounts for the difference between plate and fluid temperatures.

$$F' = \frac{1}{U_LD_o[\frac{1}{U_LD_i} + \frac{1}{\pi D_ih_f}]} \quad 5\text{-}4$$

Where D_o is the outer tube diameter, D_i is the inner tube diameter and h_f is the convection heat transfer coefficient between the inner wall and the fluid.

For liquid metals like liquid sodium HTF, convection heat transfer correlation is given by [42]:

$$\begin{aligned} Nu_f &= 6.3 + 0.0167 Re_D^{0.85}\, Pr^{0.93} \quad && for\ turbulent\ flow \\ Nu_f &= 4.36 && for\ laminar\ flow \end{aligned} \qquad 5\text{-}5$$

The MPT used for evaluating the losses can be calculated as follows:

$$T_{mp} = T_{fi} + \frac{Q_u}{AF_R U_L}(1 - F_R) \qquad 5\text{-}6$$

The aforementioned equations can be rearranged in different forms in order to evaluate the unknowns; in the following analysis we assume that the receiver is operating under varying mass flow rate to achieve a constant output temperature. Since the heat loss from the receiver is dependent on the MPT and thus the fluid output temperature, an initial guess is used to evaluate the coefficients and then an iterative process is used to update the variables.

5.2 Receiver Thermal Losses

The overall heat loss coefficient U_L is an important parameter in determining the performance of the solar receiver, this section is dedicated to formulating the equations needed to evaluate this parameter. There are five main loss mechanisms associated with the receiver of a concentrated solar plant: convective loss, radiative loss, conductive loss, loss due to reflection, and spillage. In a well designed receiver thermal losses account for 5%-15% of total available energy, hence a reasonable estimate using mean plate temperature (MPT) is adequate to determine receiver performance [8].

In the following analysis we will assume a plate external receiver (i.e. without cover). The absorptivity of the receiver in solar spectrum is assumed α_s= 95% and the longwave emissivity ε= 10%.

Forced Convection from the receiver surface is calculated using Nusselt number correlations for horizontal plates, we assume a laminar flow on the receiver surface since the Reynolds number (Re_L) on the receiver is for the most part lower than the transitional Reynolds number ($Re_{x,tr}$= $5x10^5$) [41] or ($Re_{x,tr}$= 10^5) [42]

$$\overline{Nu}_{forced} = 0.664\, Re_L^{\frac{1}{2}}\, Pr^{\frac{1}{3}} \qquad 5\text{-}7$$

Where $\overline{Nu}_{forced}$ is the average forced convection Nusselt number on the receiver surface, Pr is Prandtl number of air = 0.69, Re_L is Reynolds number given by $Re_L = u_e L/v$. u_e is wind speed m/s, L is the characteristic length of the receiver (diameter) and v is the kinematic viscosity of air = 16.1E-6 m^2/s. All fluid properties where calculated at an average temperature of 700 K.

Natural Convection can be significant at elevated temperatures. Therefore a mixed flow regime is expected. The Grashof number is given by [42]:

$$Gr_L = \frac{\beta \Delta T g L^3}{v^2} \qquad 5\text{-}8$$

Where ΔT is the temperature difference between the MPT and the fluid temperature (ambient temperature), g is the gravitational acceleration m/s^2, and v is the kinematic viscosity of the fluid m^2/s.

The Nusselt number for laminar and turbulent flows are given by :[42]

$$\overline{Nu}_{natural} = 0.54(Gr_L Pr)^{1/4}, \quad 1E5 < (Gr_L Pr) < 2E7 \quad Laminar$$
$$\overline{Nu}_{natural} = 0.14(Gr_L Pr)^{1/3}, \quad 2E7 < (Gr_L Pr) < 3E10 \quad Turbulent \qquad 5\text{-}9$$

For mixed convection, natural and forced convection Nusselts numbers are combined using: [42]

$$\overline{Nu}^{7/2} = \overline{Nu}_{forced}{}^{7/2} + \overline{Nu}_{natural}{}^{7/2} \qquad 5\text{-}10$$

Therefore, the convection heat transfer coefficient (in W/m^{2}K) is given by $\bar{h}_c = \frac{kNu}{L}$, where k is the conductivity of air = 0.02705 W/mK.

Radiative heat loss is given by the following equation

$$\dot{Q}_{rad} = A\epsilon\sigma\,(T_{mp}^4 - T_{sky}^4) \qquad 5\text{-}11$$

Where $\dot{Q}_{rad}$ is the radiative heat loss in W, T_p is the MPT in K and T_{sky} is the effective sky temperature in K. Hence the radiative heat transfer coefficient relative to air temperature is given by:

$$h_r = A\epsilon\sigma\frac{T_{mp}^4 - T_{sky}^4}{T_{mp} - T_e} \qquad 5\text{-}12$$

Conductive losses are assumed to be negligible and losses due to *spillage* are accounted for in the calculation of incident power as will be shown in the next section.

Hence the overall heat loss coefficient is given by:

$$U_L = h_r + h_c \qquad 5\text{-}13$$

5.3 Incident Power Variation

The amount of power incident on the receiver aperture is a function of the receiver size. Ideally solar radiation should be concentrated on a single point, however due to various error sources and sunshape the concentrated flux scatters around the central point as shown in

Figure 5-1. Hence the amount of power incident of the receiver will change depending on the receiver size.

It can be seen from

Figure 5-1 that the amount of power intercepted by the receiver is proportional to the aperture radius. At the same time, thermal losses are proportional to the receiver size and thus an optimal receiver size at a certain operating temperature is expected.

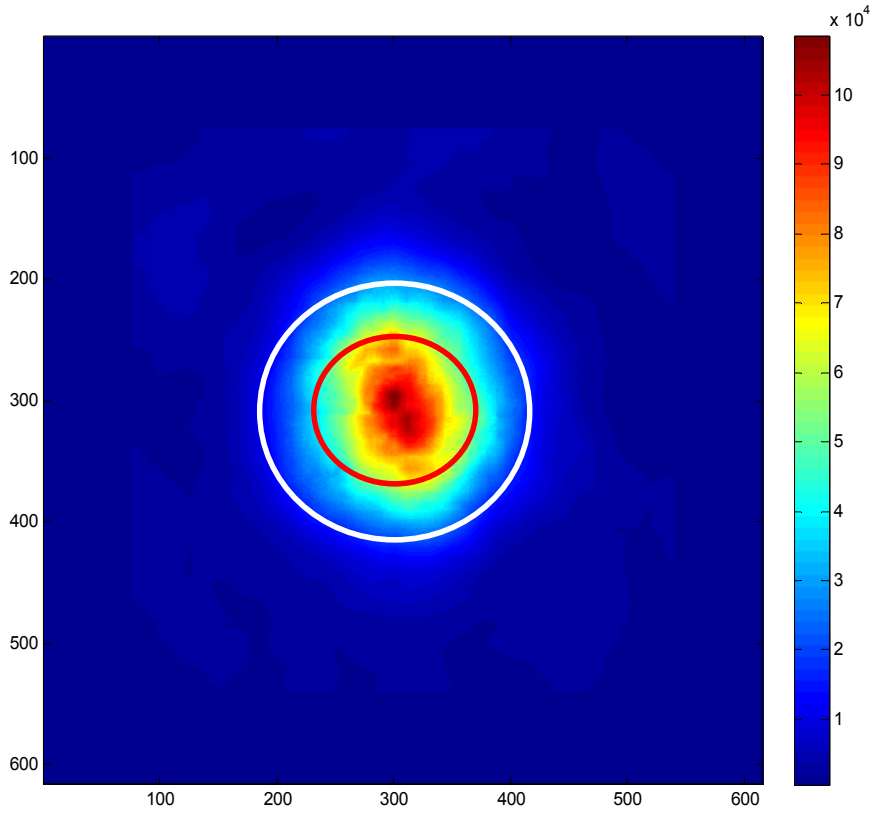

Figure 5-1 A typical flux map showing a conceptual two-aperture receiver, inner receiver for high temperature superheating and outer receiver for low temperature preheating.

Figure 5-2 shows the cumulative power (P_{cum}) intercepted by the receiver at varying receiver sizes and for different times of the test day. It can be seen that the amount of power intercepted increases with the receiver size until it saturates at high receiver sizes. Cumulative power (*Pcum*) can be calculated as follows:

$$P_{cum} = \int \int G(r,\theta) d\theta dr \qquad 5\text{-}14$$

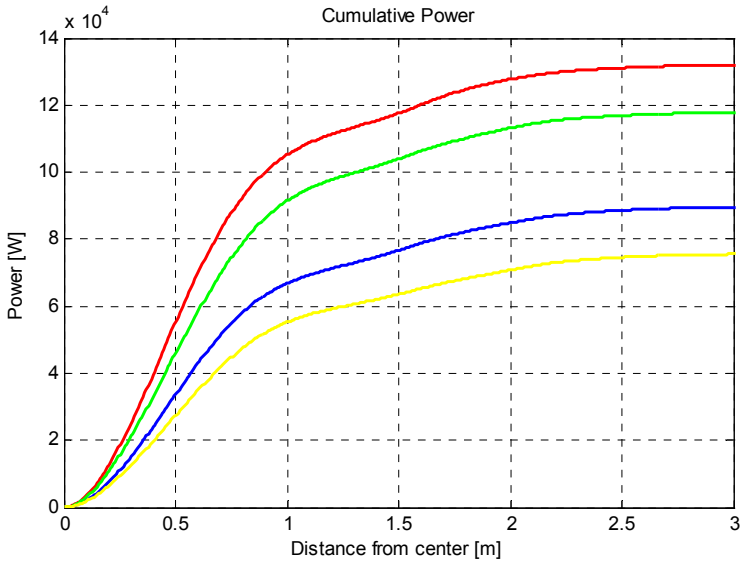

Figure 5-2 Cumulative power (*Pcum*) intercepted by the receiver starting from the centroid until a radial distance (*r*). Curves are shown for different times of the day.

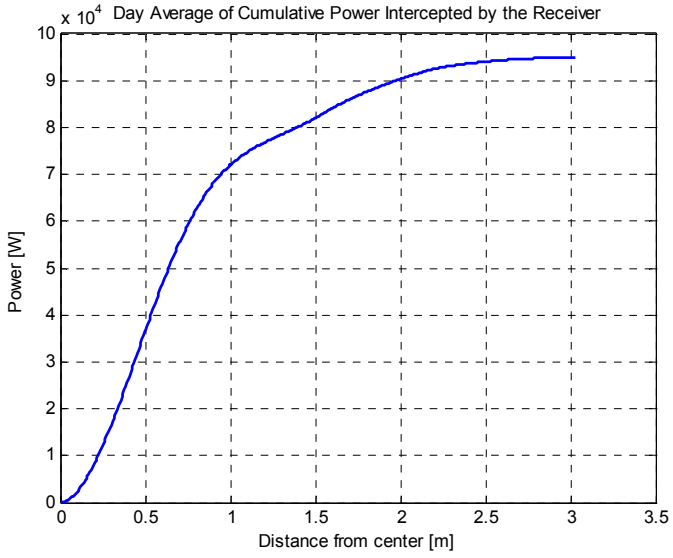

Figure 5-3 Daily average cumulative power (*Pcum*) intercepted by the receiver starting from the centroid until a radial distance (*r*).

The day-average cumulative power intercepted by the receiver at varying receiver sizes is shown in Figure 5-3. The day average reaches ~95 kW at a receiver radius of 3.0 m.

5.4 RECEIVER SIZING

The optimal receiver size, at a certain output Mean Fluid Temperature (MFT), is decided by maximizing the day average of equation 5-1. Figure 5-4 illustrates the incident power, convection and radiation losses in addition to the net useful power collected by the receiver. The curves are calculated for output MFT of 500°C. It can be seen that a maxima for net power occurs at a certain receiver radius.

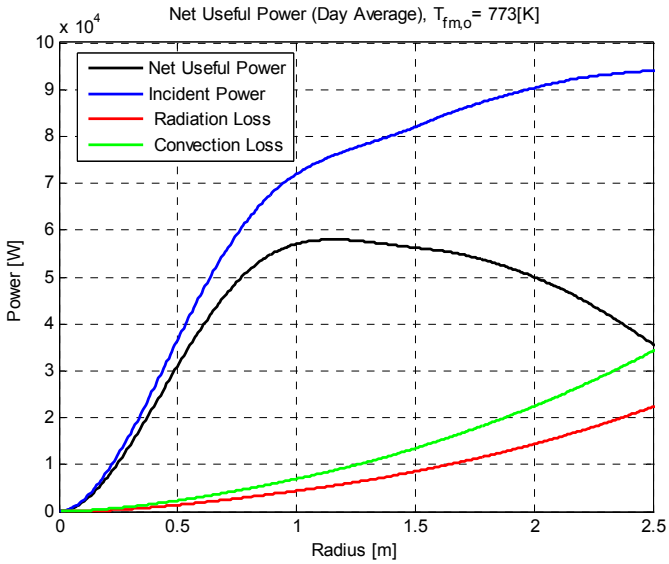

Figure 5-4 Net power collected as a function of receiver radius. Convection and radiation losses are also shown as a function of receiver size.

5.5 RECEIVER PERFORMANCE

Figure 5-5 depicts the optical efficiency of the receiver at varying output MFT. Optical efficiency represents the amount of energy that is intercepted by the receiver aperture normalized

by incident DNI * Heliostat Area. This optical efficiency accounts for all the factors that attenuates the concentrated radiation until it reaches the receiver but before it gets converted into thermal power. Optical efficiency includes cosine factor, reflectivity of both heliostats and the CR mirrors, beam attenuation, incident angle modifier, blocking and shading of heliostats and last but not least; the intercept factor of the receiver.

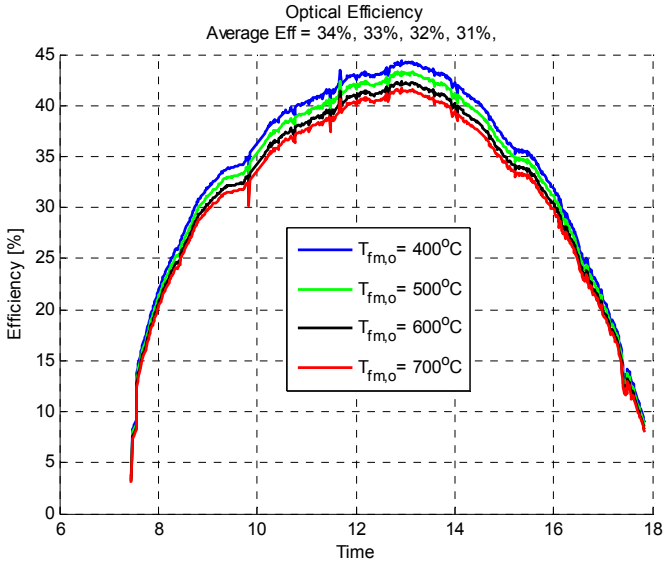

Figure 5-5 Optical efficiency of the receiver

The average efficiency of the receiver is varying slightly with temperature from 31% to 34% on average. This is because the optimal receiver size is changing based on the required output MFT. Since higher temperatures require smaller receivers, the optical efficiency is less; this was shown in Figure 5-4.

Figure 5-6 depicts the variation of receiver efficiency throughout the day and for varying output MFT. As expected higher temperatures will result in receiver efficiencies due to heat loss. The average receiver efficiency varies from 64% to 72% for different output MFT.

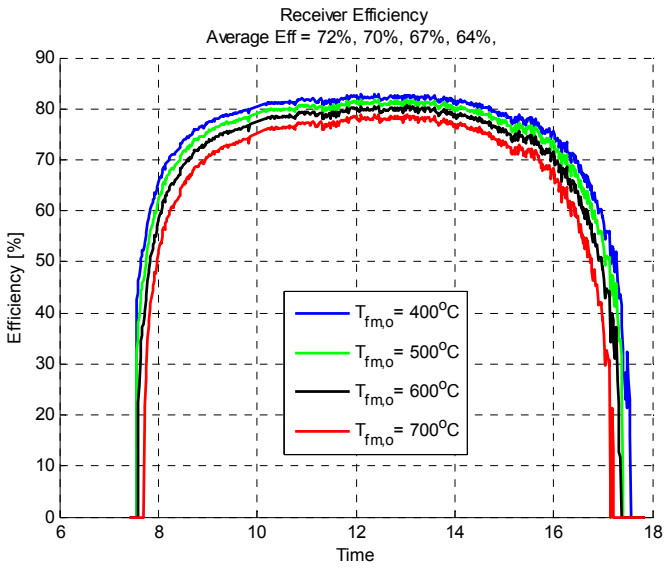

Figure 5-6 Receiver thermal efficiency

The overall efficiency of the receiver is shown in Figure 5-7. It is the product of optical and thermal efficiencies of the receiver, and on average it is varying from 22% to 26%.

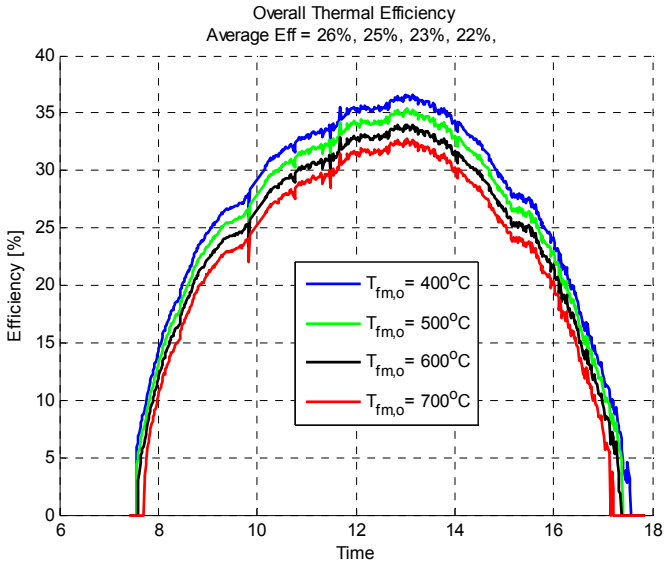

Figure 5-7 Overall efficiency of the receiver

The useful power that can be collected by the receiver throughout the day and for varying output MFT is depicted in Figure 5-8. The peak power is changing from ~84 kW for an output MFT of 700 ^{o}C to ~95 kW for an output MFT of 400^{o}C.

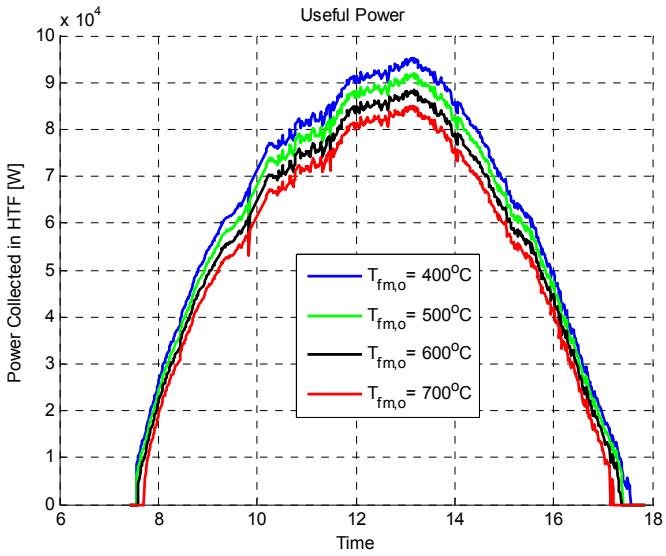

Figure 5-8 Useful power collected in the HTF

The useful power collection is a bit misleading, since it fails to show the quality of the energy collected. Figure 5-9 depict the maximum possible work (Exergy) that can be done by the fluid for varying temperatures, it is clear that higher temperatures (up to a point) can achieve higher net work although the actual thermal energy collected is less. Figure 5-10 illustrates the variation of mean maximum possible work as a function of output MFT a maxima is evident around an output MFT of 923 K (650^{o}C).

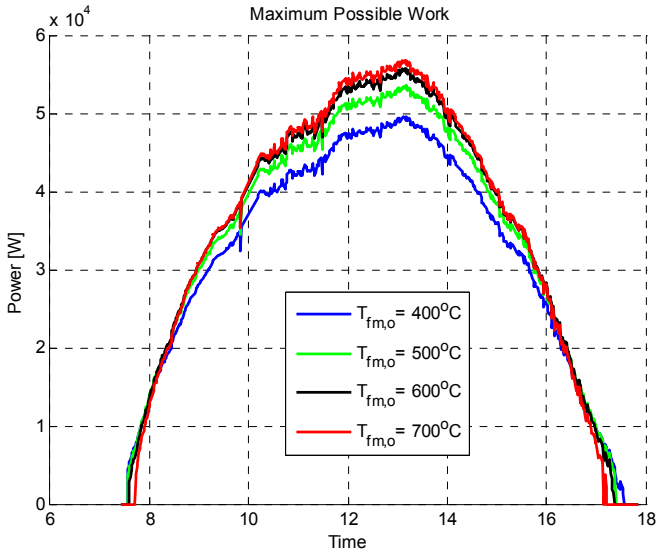

Figure 5-9 Maximum possible work rate (Exergy)

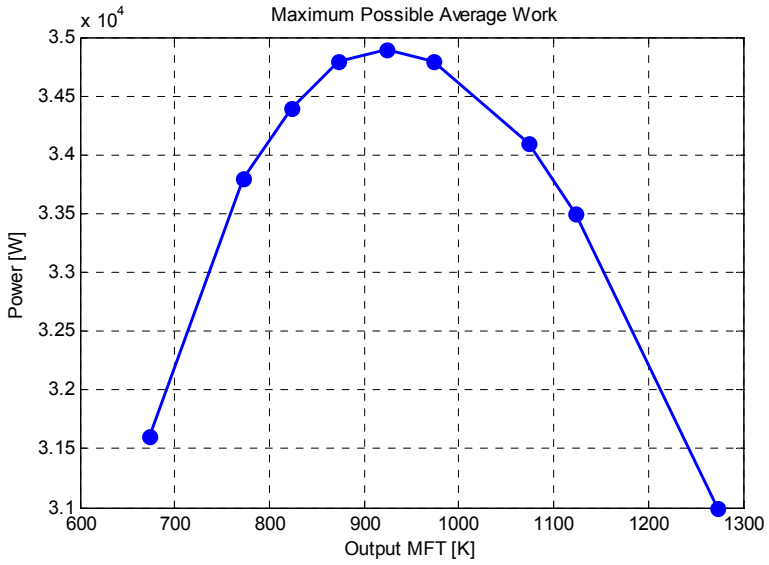

Figure 5-10 Day average of maximum possible work as a function of output MFT

5.6 SUMMARY

In this Chapter an analysis of the Beam-Down performance under full concentration was presented. The analysis is based on a hypothetical receiver design to assess the performance

under varying output MFTs. The receiver design parameters are mainly the size of the receiver, the output MFT of the HTF, in addition to the heat loss coefficients, which are correlated to the previous two parameters.

An optimal receiver size is computed for each condition based on maximizing the daily energy collection of the receiver. Based on maximum energy collection, it is obvious that operating the receiver at the lowest output MFT is more efficient. However if maximum work is the target, then operating the receiver at around 650^{o}C output MFT yielded the maximum possible mechanical power. Further increase in the temperature will cause higher losses and less energy while lower temperature will result in lower availability and hence lower overall mechanical power.

CHAPTER 6

PRACTICAL CONSIDERATIONS IN THE BEAM-DOWN SOLAR THERMAL CONCENTRATOR

6.1 OPTICS ALIGNMENT

The tracking sensor (see Figure 1-5) is an essential part of each heliostat that ensures accurate operation. The sensor reduces collective inaccuracies of the heliostat's tracking system, drives, structure and positioning. Hence careful positioning and alignment of the sensor is crucial, any error in this alignment will be directly translated to an error in the focus of the heliostat.

When the sensor is illuminated by radiation from the heliostat's control mirror it sends two differential voltage signals to the tracking system controller, these represent the position error signals, one voltage represents the difference between the right and left sensing elements and the other represents the difference between the upper and lower sensing elements. The four sensing elements will all read the same if and only if the radiation is parallel to the axis of the sensor. Aligning the sensor axis to intersect with the focal point ensures that the heliostat will point to the correct focal point at all times.

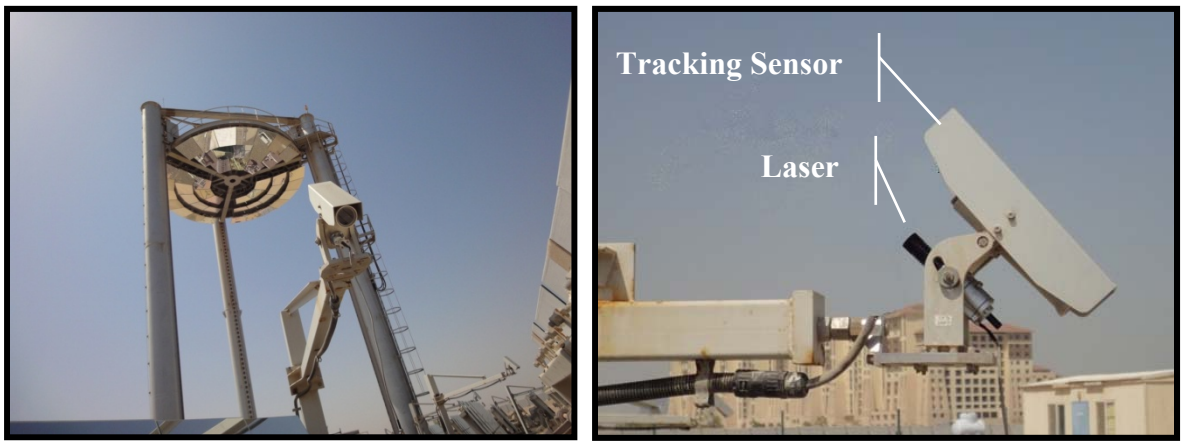

Figure 6-1 Tracking feedback sensor with laser pointer used for the alignment

The alignment procedure of the sensor requires adjusting elevation and azimuth angles of the sensor in order for it to intersect the upper focal point (~20 m). It also requires translational adjustment of the sensor position in space so that the sensor will be in line with the line joining the control mirror center and the focal point. The alignment is done by lowering the CR and shooting a laser beam parallel to the sensor axis, the beam should be intercepted by a small target on the focal point, the intercept point will be within a certain offset from the center of the target since the laser pointer is offset of the sensor axis. Another laser beam originating from the other

end of the laser pointer should be intercepted by the control mirror at its center; and this beam should be reflected back to its source when the heliostat is pointing at the focal point.

The central reflector (CR) mirrors control the intersection point of the radiation on the target. After ensuring that the radiation is directed by the heliostats to the focal point using the tracking system and the feedback sensor, it is necessary to ensure that the radiation will get reflected to the center of the target. Alignment of CR mirror is also checked with the help of a laser beam. With the CR in its upper position, the laser beam directed towards the focal point will be reflected by the CR mirror to the target, the position of the laser on the target indicates whether the CR mirror inclination angle is correct. Figure 6-2 depicts Intersection points of laser beam on the target plane. Experiment was done four times for each heliostat at different laser pointer rotation angles, differences are due to mechanical inaccuracies in the laser attachment bracket which are magnified by long travel distance. It can be seen that most of the heliostats have close intersection points with the target which indicates that the sensor and the CR mirror are well aligned. On the other hand some heliostats need adjustment e.g. B5 and A6.

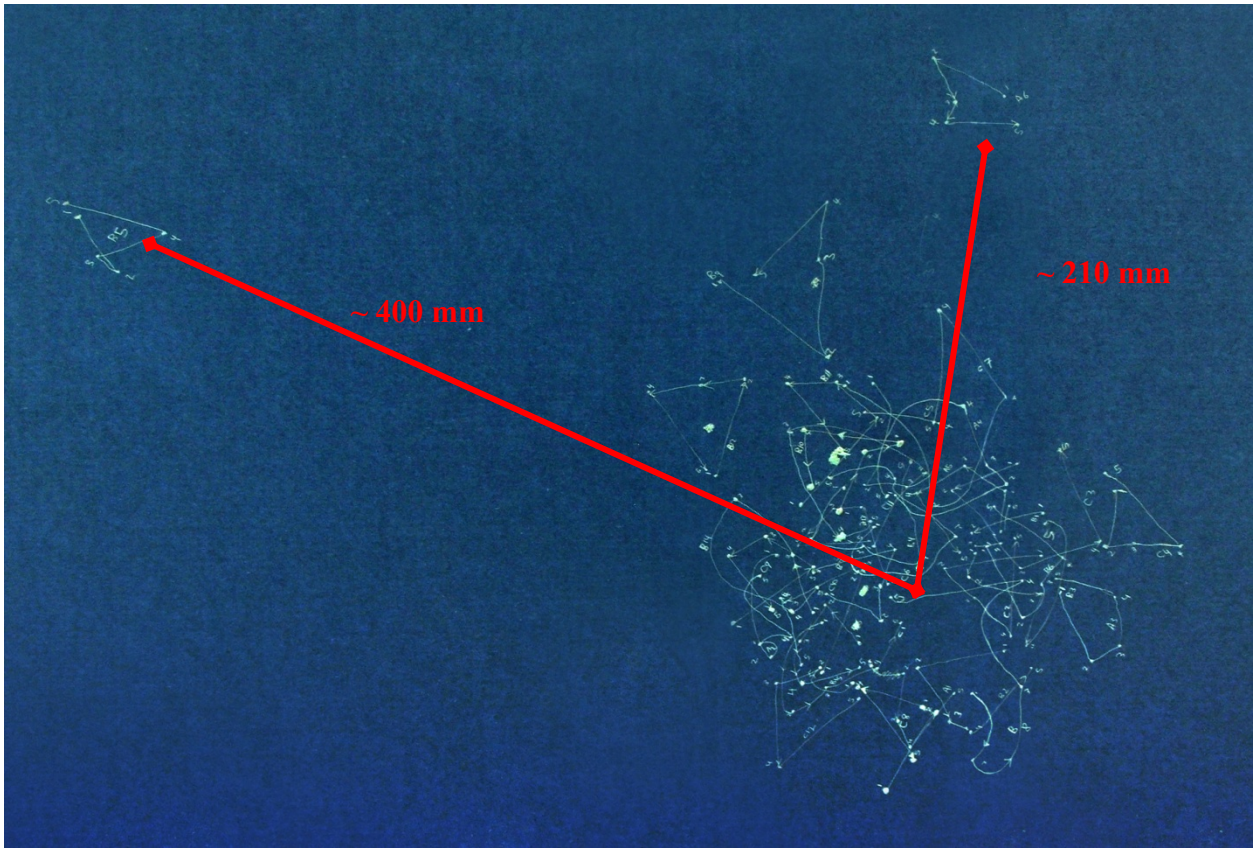

Figure 6-2 Intersection points of laser beam on the target plane. Experiment was done four times for each heliostat at different laser pointer rotation angles, differences are due to mechanical inaccuracies in the laser attachment bracket which are magnified by long travel distance.

Case of Heliostat B8

Misalignment of the sensor or the CR mirror result loss of power and concentration quality. Figure 6-3 shows the effect of sensor misalignment combined with low focus of canting angles resulting in some of the radiation being reflected by the wrong CR mirror. The heliostat B8 should focus radiation on the CR mirror in the middle ring; however some of the radiation falls on the CR mirror on the outer ring.

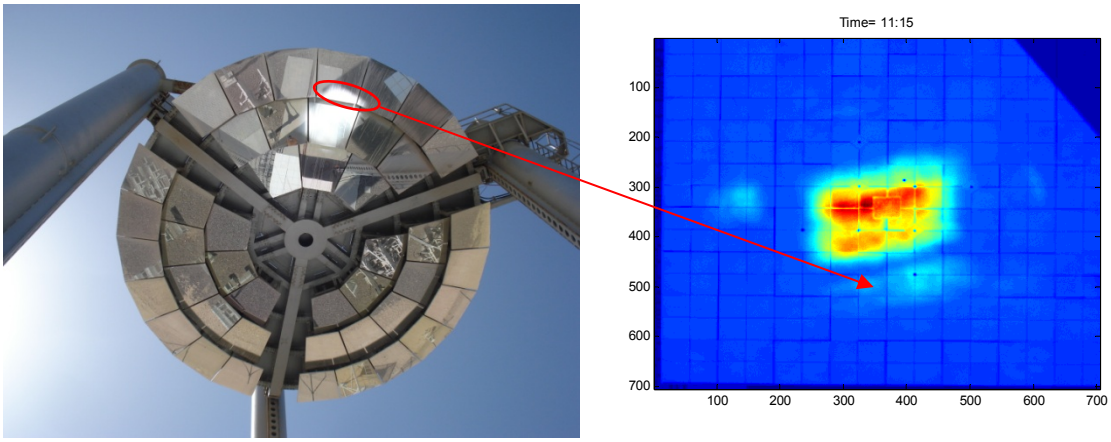

Figure 6-3 Heliostat B8 having some radiation falling on the outer CR mirror (Time: 11:15, 1:15 before solar noon).

Correcting the feedback sensor position will correct the position of the reflected radiation to be centered on the correct CR mirror (Figure 6-4). However, the image is still larger than the CR mirror and we can now see spillage from the four directions around the flux centroid.

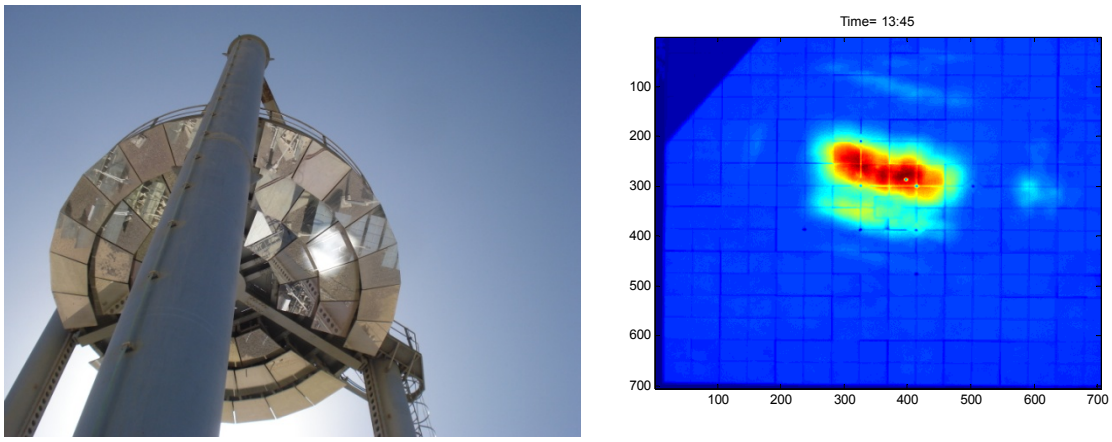

Figure 6-4 Heliostat B8 with better centering on the correct CR mirror however with scattered radiation of the four adjacent CR mirrors, and with the center of the radiation moving farther from the true target center. (Time: 13:45, 1:15 after solar noon)

Moreover the centroid of the flux on the target is shifted away from the true center of target. This can be rectified by adjusting the inclination angle of the CR mirror.

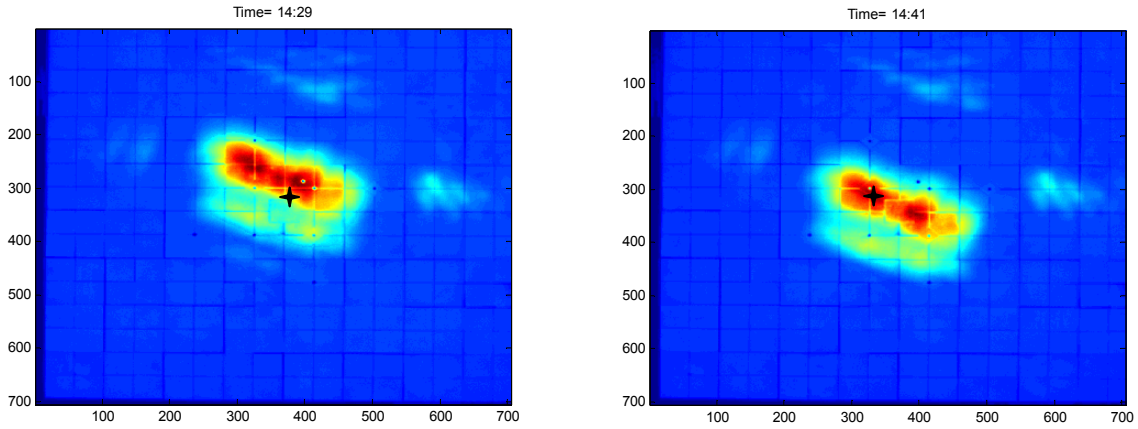

Figure 6-5 Left: B8 concentrated flux deviated from the center point. Right: B8 concentrated flux after correcting CR mirror inclination

6.2 CANTING AND SPILLAGE

Canting is the procedure of tilting the individual heliostat's facets with certain angles to trace the profile of a parabola in each axis. This normally depends on the position of the heliostat relative to its focal point. There are two main heliostat-facets canting methods as described in [43]:

1. On-axis canting is achieved by tilting the individual facets so that their surface normals would intersect at a distance twice the focal length of the heliostat. This is normally done by calculating the necessary focal length of each heliostat based on its distance from the target. The tilt angles are then implemented using inclinometers, a laser system or a look back camera system. It is called on-axis since it is optimized for the condition when the target, the sun and the heliostat center are all on the same line (ironically, a situation that will never happen due to shadowing of the heliostat by the tower!).

This is the procedure which is used for canting Beam Down heliostats using a laser system; it is performed for each set of mirror banks before they are installed. For each heliostat of 3-mirrror banks, each bank has the same set of canting angles, however the elevation rotation axis have relative angles of rotation to account for the offset location of each bank from the center.

2. Off-axis canting is implemented during operation by tracking the sun and changing the tilt angle of the individual facets in order to minimize the size of the reflected radiation on the target. In this case the facets normals do not intersect on a single point.

It should be noticed that both methods provide optimal performance of the heliostat for only one particular geometry [43]. According to Jones, Off-axis canting is fast, easy to implement and is inexpensive, however its performance is highly dependent on time of canting. In addition, although off-axis canting could theoretically have better performance it was found that On-axis canting have uniformly higher performance. Buck et al discussed several variations of canting methods and found that on-axis canting will actually have the worst performance of all canting methods [44], a clear contradiction.

In any case, the beam down plant, unlike normal tower plant, has an extra constraint that has to be taken into account before deciding on the optimal canting method. In normal tower plants, heliostats are canted with a focal length for each heliostat that corresponds to a single point target. In the beam down however the focal length of the heliostats is different than the focal length of the whole plant. While the focus of the heliostat field as whole occurs on the target plane 2.3 m above ground level, the focus of the individual heliostats occurs in almost 10 m above the target, see Figure 6-6.

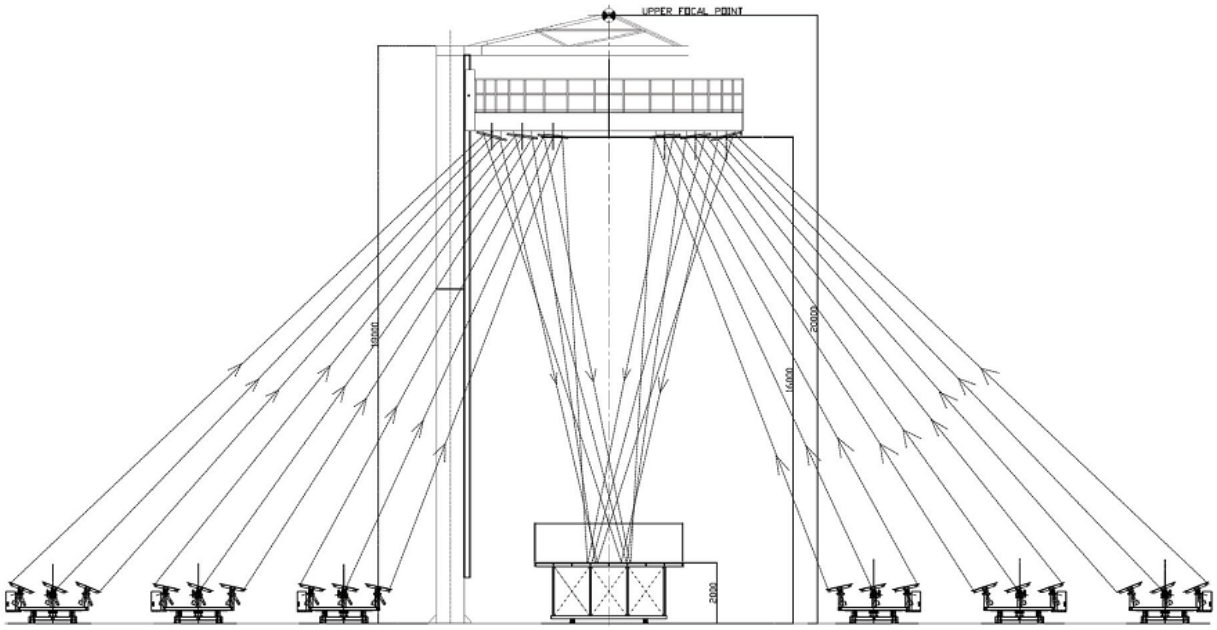

Figure 6-6 Vertical cross sectional view of Beam Down concentrator showing individual heliostat focus well above the target plane [6]

The reason for this premature focus of the heliostats is the small size of the CR mirror. If the focal length of the individual heliostats was set to have the focus on the target plane then the image size as it reaches the CR mirror surface will be too big and a significant amount of the radiation will be lost around the CR mirror. Hence it was necessary to cant the heliostat facets in a steeper set of angles to ensure that the most of the radiation will be intercepted by the CR mirror. This can be shown by using the geometrical model we developed in chapter 2 before.

Figure 6-7 illustrates the effect of having different canting angles of the heliostats on concentration quality and spillage. It can be seen that the spillage is higher (33%) when the heliostat is canted with the steeper angles compared to the original canting angles (spillage of 7%) although the concentration quality on the target is better for the steeper canting angles.

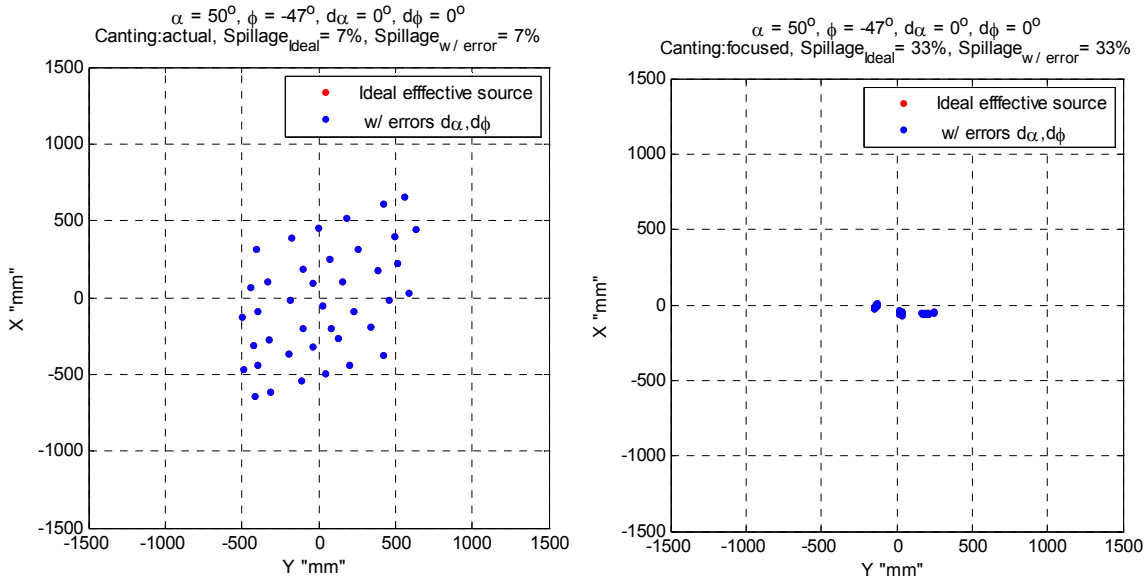

Figure 6-7 Effect of canting angles on the spillage of the reflected radiation and on the quality of the concentrated radiation on the target plane. Left: Actual canting angles used. Right: "Focuced" canting angles.

Figure 6-8 describes how the spillage of a heliostat changes during the day for different sets of canting angles. It shows that actual canting angles have significantly less spillage. It also shows that spillage increases as the sun deviates from solar noon at zero sun azimuth (with respect to heliostat/tower angle)

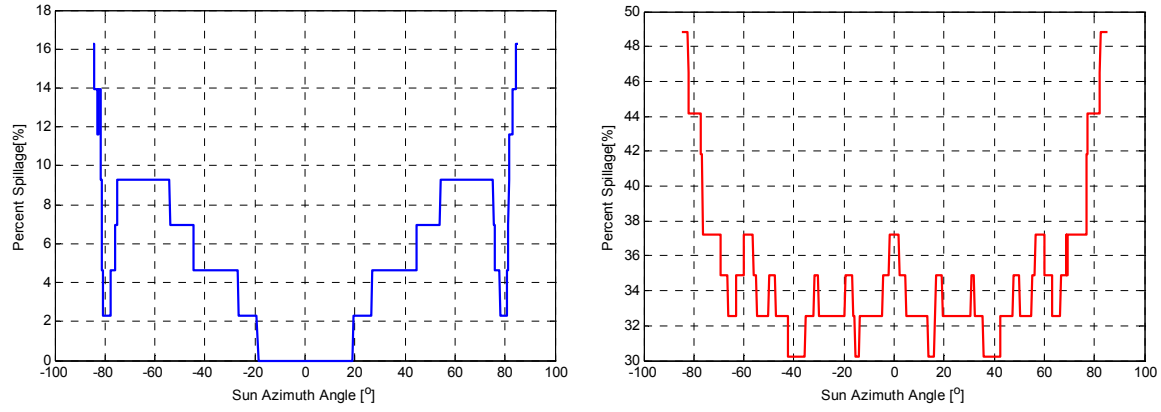

Figure 6-8 Heliostat spillage variation simulated for 9-March-2011. Left: Actual canting angles used. Right: "Focuced" canting angles.

In order to have higher concentration the heliostat and field foci should coincide, this can be achieved under the current design by closing the gap between the CR and the target and modifying the tilt angles of both the heliostats and the CR mirrors, this can be done by lowering the CR, raising the target or both. But this will increase blocking in the heliostat field or field size or both, and will also increase mean cosine loss. Another possibility is to have solid continuous CR mirror that will be able to accommodate the radiation coming from neighboring heliostats.

CONCLUSION

There are two main parts of this thesis, both of which were a response to the problems we faced during our initial testing of the Beam-Down plant; first is the theoretical modeling of the concentrator optics and second is the experimental work on the measurement system and the characterization of the plant's performance. These activities are highlighted in Figure 0-1.

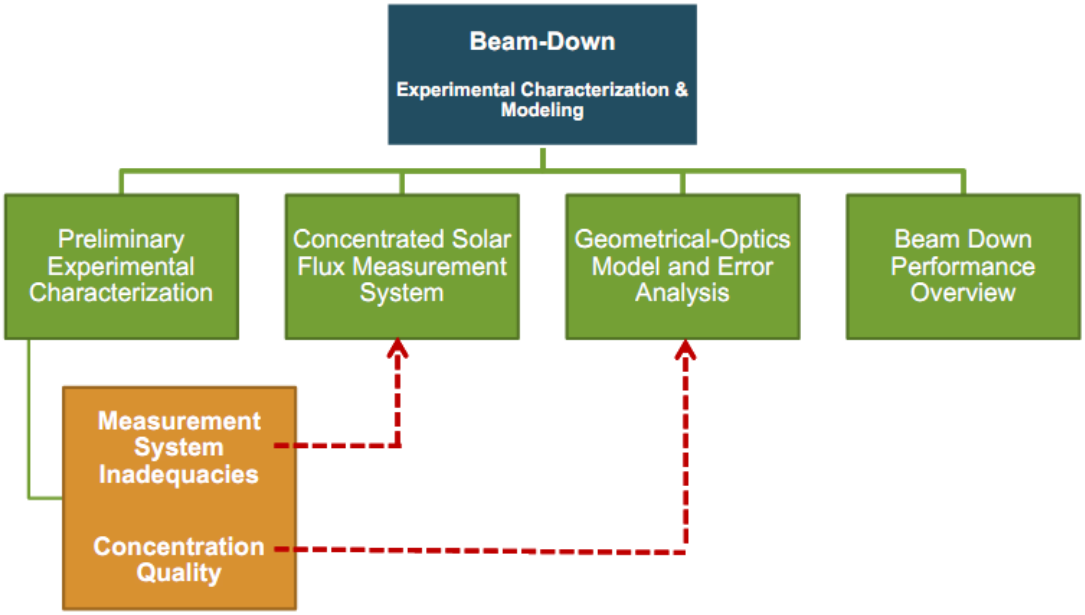

Figure 0-1 Outline of tasks performed at the beam down plant

In an effort to assess the concentration quality of individual heliostats, an optical measurement of the flux distribution of each heliostat was done at several sun positions. Due to the overwhelming number of images to be processed, we devised an automatic method to detect the irregularities in the performance of the heliostats which helped in pointing out heliostats with alignment, shading or other concentration problems.

The results of this test indicated that two main issues require further investigation and became the focus of this thesis; first is the reliability of the flux measurement set up used to characterize the performance of the plant and the concentration quality of the individual heliostats.

In order to further investigate the concentration quality of the unique heliostats and the reasons for the errors observed in their images, a model was considered necessary. A unique geometrical optics model was presented. The model was developed to investigate the causes of optical aberrations of the heliostats. It was also adapted to assess the effect of varying optical errors and sunshapes on concentration quality and radiation spillage. The optical model uses geometry and vector algebra to maintain the computation speed high compared to expensive commercial ray tracing packages. The code combines analytical and numerical methods in simulating the flux images of the heliostats which makes it suitable for design and optimization purposes. Especially because of its ability to study the effect of various errors and sunshapes on the concentration quality.

Efforts were directed on enhancing the accuracy of the heat flux sensors which are used as a reference for the optical flux measurement system consisting of a Charge-Coupled Device

(CCD) camera. A regression model for correcting the heat flux sensor measurement was proposed. It was founded on a convective and radiative heat transfer model of the flux sensor. As was shown, the proposed model for calibration reduces the measurement error significantly, especially at low radiation fluxes. In addition, since the model is based on easily measurable variables it can be applied conveniently on existing measurement systems without major modifications. Using this unique correction method we were able to enhance the measurement accuracy significantly to levels matching the accuracy of the reference instrument.

An analysis of the Beam-Down performance was presented. The analysis was based on a hypothetical receiver design to assess the performance under varying conditions. An optimal receiver size was computed for each condition based on maximizing the daily energy collection of the receiver. It was found that operating the receiver at around 650^{o}C output MFT yielded the maximum possible mechanical power. Further increase in the temperature will cause higher losses and less energy while lower temperature will result in lower availability and hence lower overall mechanical power. The analysis was based on full concentration test data obtained experimentally at the plant in March 2011 using the retrofitted measurement system.

FUTURE WORK

The Beam-Down solar concentrator is a one of a kind facility in terms of the optical design of the plant and the heliostat field. The ability test several receiver concepts, heliostat designs, reflective surfaces, measurement systems …etc, makes the Beam-Down plant an important test facility.

- **Measurement System**: After our experience with the flux measurement system we are looking for validating our results using calorimetry. A new receiver is being built by our Japanese partner (MES) to validate the test results. In addition, a new flux measurement system is being implemented to measure flux using a moving bar of 9 HFS to continuously scan the receiver plane. Unlike the existing measurement system, this system can take measurement during normal operation with the receiver installed, it is also expected to be more accurate. The system is necessary to study the performance of the receiver under investigation. Problems like the dynamic response of the HFS under varying illumination is expected and the necessary test are planned to determine the adequate scan speeds. In addition position feedback of the sensors position is required.

The new measurement system along with the receiver should provide enough information to validate the previous results.

- **Cavity receivers:** are well suited for this tower layout and concentration quality can be enhanced by means of secondary CPC concentrators. High temperature can achieved by the cavity receiver can be used to drive or to be hybridized with efficient gas cycles. This can become an important facility for research on solar-fuels and solar-assisted power cycles.
- **Heliostat Design:** The heliostat design is also one of the topics that require more investigation, the performance of the ganged type heliostat from concentration quality point of view was not satisfactory, and hence different designs have to be considered.
- **Optical Design and Trade-offs**: During our investigation, it was found that a compromise in the design was made between the size of the central reflector mirrors and the concentration level on the target. Currently the heliostats have a focal length which is shorter than the path to the target plane; this means that the heliostat radiation reaches its maximum concentration point before it reaches the target and the starts spreading. This was done because of the limitation in the CR mirror size and to reduce spillage. However we think that this compromise requires more investigation, one of the possible solutions can be decreasing the CR height on the expense of blocking and shading of heliostat field, or raising the receiver on the expense of higher structural costs, or of course using a bigger CR mirrors.

BIBLIOGRAPHY

[1] Greenpeace, SolarPaces, and ESTELA, *Concentrating Solar Power,Global Outlook 2009*, 2009.

[2] O. Goebel, "Shams One 100 MW CSP Plant in Abu Dhabi, Update on Project Status," *Proceedings of 16th International Symposium on Concentrated Solar Power and Chemical Energy Technologies*, France: 2010.

[3] M. Kaltschmitt, W. Streicher, and A. Wiese, *Renewable energy: technology, economics, and environment*, Springer Verlag, 2007.

[4] Sargent & Lundy LLC Consulting Group, *Assessment of Parabolic Trough and Power Tower Solar Technology Cost and Performance Forecasts*, NREL, Golden, Colorado, USA: 2003.

[5] M. Mokhtar, I. Rubalcaba, S. Meyers, A. Qadir, P. Armstrong, and M. Chiesa, "Heliostat Field Efficiency Test of Beam Down CSP Pilot Plant Experimental Results," *Proceedings of 16th International Symposium on Concentrated Solar Power and Chemical Energy Technologies*, Perpignan, France: 2010.

[6] H. Hasuike, M. Yuasa, H. Wada, K. Ezawa, K. Oku, T. Kawaguchi, N. Mori, W.

Hamakawa, H. Kaneko, and Y. Tamaura, "Demonstration of Tokyo Tech Beam-Down Solar Concentration Power System in 100kW Pilot Plant," *Proceedings of 15th International Symposium on Concentrated Solar Power and Chemical Energy Technologies*, Germany: 2009.

[7] A. Rabl, "Tower reflector for solar power plant," *Solar Energy*, vol. 18, 1976, pp. 269-271.

[8] C.J. Winter, R.L. Sizmann, and L.L. Vant-Hull, *Solar power plants: fundamentals, technology, systems, economics*, Springer-Verlag, 1991.

[9] Y. Tamaura, M. Utamura, H. Kaneko, H. Hasuike, M. Domingo, and S. Relloso, "A novel beam-down system for solar power generation with multi-ring central reflectors and molten salt thermal storage," *Proceedings of 13th International Symposium on Concentrated Solar Power and Chemical Energy Technologies*, 2006.

[10] J. Duffie and W. Beckman, *Solar Engineering of Thermal Processes*, Madison: JOHN WILEY & SONS, INC., 2006.

[11] William B. Stine and Michael Geyer, *Power From The Sun, eBook*, 2001.

[12] S.A. Meyers, "Flux Mapping of the Beam Down Solar Thermal Concentrator at Masdar City, UAE," Masdar Institute of Science and Technology, 2011.

[13] P. Garcia, A. Ferriere, and J.J. Bezian, "Codes for solar flux calculation dedicated to central receiver system applications: A comparative review," *Solar Energy*, vol. 82, 2008, pp. 189–197.

[14] F.W. Lipps, "Four different views of the heliostat flux density integral," *Solar Energy*, vol. 18, 1976, pp. 555-560.

[15] E.A. Igel and R.L. Hughes, "Optical analysis of solar facility heliostats," *Solar Energy*, vol. 22, 1979, pp. 283–295.

[16] F.J. Collado, A. Gómez, and J.A. Turégano, “An analytic function for the flux density due to sunlight reflected from a heliostat,” *Solar Energy*, vol. 37, 1986, pp. 215–234.

[17] P. Bendt, H. Gaul, and A. Rabl, “Determining the optical quality of focusing collectors without laser ray tracing,” *Journal of Solar Energy Engineering*, vol. 102, 1980, p. 128.

[18] P. Bendt, H.W. Gaul, and A. Rabl, *Determining the Optical Quality of Focusing Collectors without Laser Ray Tracing*, National Renewable Energy Laboratory (NREL), Golden, CO., 1980.

[19] P. Bendt and A. Rabl, “Optical analysis of point focus parabolic radiation concentrators,” *Applied Optics*, vol. 20, 1981, pp. 674–683.

[20] P. Bendt, A. Rabl, H.W. Gaul, and K.A. Reed, *Optical analysis and optimization of line focus solar collectors*, National Renewable Energy Laboratory (NREL), Golden, CO., 1979.

[21] R.B. Pettit, C.N. Vittitoe, and F. Biggs, “Simplified calculational procedure for determining the amount of intercepted sunlight in an imaging solar concentrator,” *Journal of Solar Energy Engineering*, vol. 105, 1983, p. 101.

[22] Yutaka Tamaura et al., *Tokyo Tech Beam Down Concentration Power System, Final Report*, 2010.

[23] A. Neumann, A. Witzke, S.A. Jones, and G. Schmitt, “Representative terrestrial solar brightness profiles,” *Journal of Solar Energy Engineering*, vol. 124, 2002, p. 198.

[24] S. Ulmer, W. Reinalter, P. Heller, E. L\üpfert, and D. Martinez, “Beam characterization and improvement with a flux mapping system for dish concentrators,” *Journal of solar energy engineering*, vol. 124, 2002, p. 182.

[25] J. Ballestrín and R. Monterreal, “Hybrid heat flux measurement system for solar central

receiver evaluation," *Energy*, vol. 29, Apr. 2003, pp. 915-924.

[26] S. Ulmer, E. Lüpfert, M. Pfänder, and R. Buck, "Calibration corrections of solar tower flux density measurements," *Energy*, vol. 29, 2004, pp. 925–933.

[27] D. Rall, "Heat Flux," 1972.

[28] S. Meyers, A. Qadir, I. Rubalcaba, M. Mokhtar, M. Chiesa, and P. Armstrong, "Development of a correlation between luminous intensity and solar flux for the beam-down tower configuration," *Proceedings of 16th International Symposium on Concentrated Solar Power and Chemical Energy Technologies*, Perpignan, France: 2010.

[29] M. Mokhtar, S. Meyers, M. Chiesa, and P. Armstrong, "A Model for Enhancing the Measurement of Heat Flux Sensors at Low Flux," *submitted to Solar Energy Journal*, Jan. 2011.

[30] J. Kaluza and A. Neumann, "Comparative Measurements of Different Solar Flux Gauge Types," *Journal of Solar Energy Engineering*, vol. 123, 2001, p. 251.

[31] J. Ballestrín, S. Ulmer, A. Morales, A. Barnes, L.W. Langley, and M. Rodriguez, "Systematic error in the measurement of very high solar irradiance," *Solar Energy Materials and Solar Cells*, vol. 80, 2003, pp. 375–381.

[32] J. Ballestrín, C. Estrada, M. Rodríguez-Alonso, C. Pérez-Rábago, L. Langley, and A. Barnes, "Heat flux sensors: Calorimeters or radiometers?," *Solar Energy*, vol. 80, Oct. 2006, pp. 1314-1320.

[33] Benjamin K. Tsai, Charles E. Gibson, Annageri V. Murthy, Edward A. Early, David P. Dewitt, and Robert D. Saunders, "Heat-Flux Sensor Calibration," May. 2004.

[34] Vatell Corp, "Update on Heat Flux Calibration Standard Improvements," *Heat Flux Newsletter*.

[35] D. Holmberg, K. Steckler, C. Womeldorf, and W. Grosshandler, "Facility for calibrating heat flux sensors in a convective environment," *ASME-Publications-HTD*, vol. 353, 1997, pp. 165–172.

[36] A.V. Murthy, B.K. Tsai, and R.D. Saunders, "Radiative calibration of heat-flux sensors at NIST: facilities and techniques," *Journal of Research-National Institute of Standards and Technology*, vol. 105, 2000, pp. 293–306.

[37] G. Mulholland, I. Hall, R. Edgar, and C. Maxwell, "Flux gage calibration for use in solar environments," *Solar Energy*, vol. 41, 1988, pp. 41-48.

[38] C.T. Kidd and C.G. Nelson, "How the Schmidt-Boelter gage really works," *International Instrumentation Symposium, 41 st, Denver, CO*, 1995, pp. 347–368.

[39] B. Albrecht and S.K. Cox, "Procedures for improving pyrgeometer performance," *Journal of Applied Meteorology*, vol. 16, 1977, pp. 188–197.

[40] Eppley, "Precision Infrared Radiometer Instruction Sheet," *The Eppley Laboratory*.

[41] F.P. Incropera, D.P. Dewitt, A.S. Lavine, and T.L. Bergman, *Fundamentals of Heat and Mass Transfer*, John Wiley and Sons Inc., 2010.

[42] A. Mills, *Heat Transfer*, Prentice Hall, 1998.

[43] S.A. Jones, *A comparison of on-axis and off-axis heliostat alignment strategies*, Sandia National Labs., Albuquerque, NM (United States), 1996.

[44] R. Buck and E. Teufel, "Comparison and Optimization of Heliostat Canting Methods," *Journal of Solar Energy Engineering*, vol. 131, 2009, p. 011001.